



University of Liège
Faculty of Applied Sciences

Non-Destructive Methods for the Detection of Delaminations in Concrete Bridge Decks

by

Audrey Van der Wielen

A Thesis Submitted in Partial Fulfillment of the Requirements
for the Degree of
Master in Civil Engineering

Academic year 2008 - 2009



University of Liège
Faculty of Applied Sciences

Non-Destructive Methods for the Detection of Delaminations in Concrete Bridge Decks

by

Audrey Van der Wielen

A Thesis Submitted in Partial Fulfillment of the Requirements
for the Degree of
Master in Civil Engineering

Academic year 2008 - 2009

Non-Destructive Methods for the Detection of Delaminations in Concrete Bridge Decks

A Thesis Submitted by Audrey Van der Wielen in Partial Fulfillment of the
Requirements for the Degree of Master in Civil Engineering

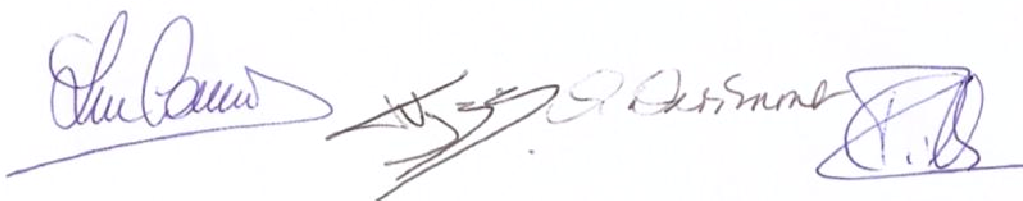
Since 1985, a new type of bridge deck degradation has appeared in Wallonia: the concrete bridge deck disintegration. Generated by a combination of simple degradation mechanisms, this phenomenon creates delaminations in the concrete deck slabs and can eventually lead to its perforation and to the ruin of the structure. In this context, the non destructive techniques (NDT) permit to inspect regularly the bridge decks and to detect abnormalities without creating any damage to the structure. Besides, after repairs, those methods can also be used to check adhesion quality.

Within the framework of this study, twelve samples were realized, presenting diverse horizontal defects to simulate delaminations at the interface between a concrete substrate slab and a repair mortar. Artificial delaminations were produced by the introduction of various defects: plastic sheets, expanded polystyrene panels or demoulding oil. Then, the various samples were scanned with a high frequency (2.3 GHz) Ground Penetrating Radar (GPR).

A specific method was developed to determine the speed of electromagnetic waves into the concrete and the depth of defects from Common Mid Point (CMP) measurements. A 3D visualization program was also created, to get a three-dimensional vision of the defects from the scans of the slabs. The influence of the depth and type of repair on the amplitude of the reflected wave was also studied.

Finally, a parallel was drawn between those results and the ones obtained by Piotr Harassek on the same samples with impact-echo, in order to evaluate the differences between the two methods.

Master Thesis Committee Members,



L. COURARD

F. NGUYEN

A. DARIMONT

P. GILLES

A. PLUMIER

Acknowledgments

First and foremost, I would like to thank my two thesis advisors, Dr. Ir. Luc Courard and Dr. Ir. Frederic Nguyen. This thesis subject is situated at the junction of their two domains of expertise, and its realization wouldn't have been possible without their support and precious advices.

Then I have to thank Piotr Harassek, who was my partner for most of the experimental part of this work. In addition to his competence, his good temper and kindness made this collaboration really pleasant.

My acknowledgements also go to all the people who gave me their time and support for the realization of the work: David Caterina, who helped me for the use of the radar equipment and gave me ideas for interpretation and visualization of results; M Husquinet, for his proficient help in slabs repair and finally Jean Arnould and Cécile Goffinet, who patiently used their English skills to proof this document from a linguistic point of view.

Finally, I want to thank my family, who's supported me for the realization of this thesis, as well as they did for my whole studies, and my boyfriend François Mahy, for his unconditional moral support and his sensible tips in the electrical domain.

Table of contents

Introduction.....	10
Part 1: State of the art	12
1 <i>Degradations and repairs of concrete.....</i>	12
1.1 Degradation mechanisms.....	13
1.2 Locating delaminated concrete.....	16
1.3 Surface preparation.....	18
1.4 Choice of repair material.....	19
1.5 Repair placement methods	20
1.6 Repair quality testing	21
2 <i>GPR.....</i>	23
2.1 Propagation of electromagnetic waves.....	23
2.2 Speed of electromagnetic waves	26
2.3 Reflection coefficient	27
2.4 Results display and analysis	28
2.5 Resolution	31
2.6 Determination of concrete electromagnetic parameters	34
2.7 Applications of GPR to concrete structures	36
3 <i>Impact-Echo</i>	39
Part 2: Experimental program	40
4 <i>Instrumentation</i>	40
5 <i>Samples.....</i>	42
5.1 Concrete substrate slabs production	42
5.2 Surface preparation.....	43
5.3 Interface roughness evaluation.....	43
5.4 Concrete substrate slabs characterization with GPR	48
5.5 Description of defects	51
5.6 Repair operations.....	52
6 <i>Investigation procedure</i>	53
6.1 CMP	53
6.2 Profile scanning	54
6.3 Acquisition parameters	55
Part 3: Results	56
7 <i>CMP signals.....</i>	56
7.1 Analysis procedure	56
7.2 Results	60
7.3 Analysis of the reflection amplitude	64
8 <i>Profiles 3D visualisation</i>	68
8.1 Data processing for visualization.....	68
8.2 Results display	70

8.3	Resolution	73
8.4	Influence of concrete age.....	74
9	<i>Comparison with Impact-Echo results</i>	76
Conclusion		78
Bibliography.....		80
Appendixes		82

List of figures

Figure 1 : Evolution of the number of cases of deck slabs decay in Wallonia (Gilles 2004).....	10
Figure 2 : Bridge deck delaminations (Gilles 2004; Demars et al.).....	10
Figure 3 : Anatomy of surface repairs (Emmons and Emmons 1993)	12
Figure 4 : Corrosion mechanism (Mommer et al. 2004).....	14
Figure 5 : Repair placement methods (Emmons and Emmons 1993)	21
Figure 6 : Pull-off testing (Emmons and Emmons 1993).....	22
Figure 7 : Radar principle (Viriyametanont 2008)	23
Figure 8 : Radar scan	28
Figure 9 : Radar profiles	29
Figure 10 : CMP acquisition principle.....	29
Figure 11 : Typical radargram obtained with CMP (Mala).....	30
Figure 12 : Peak separation in the radargram (a); Range and lateral resolution (b) (Annan 2005)	32
Figure 13 : First Fresnel zone (Reynolds 1997)	33
Figure 14: Influence of water content on dielectric properties (Soutsos et al. 2001)	34
Figure 15: Influence of steel fibers, honeycombing and salts on dielectric properties (Soutsos et al. 2001) ...	35
Figure 16 : Profiles showing evidence of (a) cracks and (b) humid zones (Pérez-Gracia et al. 2008a)	37
Figure 17 : Maps of (a) points with evidence of cracks (b) humid zones (Pérez-Gracia et al. 2008a)	37
Figure 18 : Impact-Echo principle (Sansalone and Street 1998)	39
Figure 19 : HF antenna used for investigations	40
Figure 20 : Concrete slabs sandblasting operations	43
Figure 21 : Sand patch test	44
Figure 22 : ATOS measurement	45
Figure 23 : Surface transformations to adapt ATOS outputs into RugoDS inputs	46
Figure 24: Reference surfaces equal to (a) mean+ σ (b) mean+ 2 σ	47
Figure 25 : Visualization of radargrams in Matlab7 before (a) and after (b) axes adaptation	49
Figure 26 : Slab 1.2.4 radargram (a) with time (b) with depth axis	50
Figure 27 : Description of defects at the interface between concrete slabs and repair material.....	51
Figure 28 : Slabs repair preparation (EPS defects)	52
Figure 29 : (a) Normal CMP ; (b) Double CMP ; (c) WARR	53
Figure 30 : Profile acquisition grid	55
Figure 31 : Waves involving reflections on the bottom of the slab	57
Figure 32 : CMP on slab 121, initial offset equal to (a) 19 cm (b) 5 cm	61
Figure 33 : CMP results - Defect 2 / 8 cm repair.....	62
Figure 34 : CMP results - Defect 3 (a) 5 cm repair (b) 8 cm repair	63
Figure 35 : CMP results - Defect 4 (a) 5 cm repair (b) 8 cm repair	63
Figure 36 : Radargram maximum and minimum amplitude of the different waves in function of the offset..	65
Figure 37 : Visualization of amplitude variations with offset (slab 1.2.4).....	66
Figure 38 : Amplitude variations of the reflectivity compare to the offset of a studied event at 140 MHz.	67
Figure 39 : Slab 121 (a) rough data (b) mean trace calculation (c) mean trace removal	69
Figure 40 : Longitudinal and lateral 3D results on slab 121	70
Figure 41 : 3D defect vision - no defect (slabs 1.2.3 and 1.1.3)	70
Figure 42: 3D defect vision – polystyrene defects (slabs 1.2.1, 1.1.1, 1.2.2 and 1.2.1)	71
Figure 43 : 3D defect vision – plastic sheet defects (slabs 1.3.3, 1.3.2, 1.3.4 and 1.3.1)	71
Figure 44 : Upper view of slabs with trapezoidal plastic sheet (slabs 1.3.4 and 1.3.1)	72
Figure 45 : 3D defect vision – oil defect (slabs 1.1.4 and 1.2.4).....	72
Figure 46 : Upper view of defect 4 – longitudinal profiles	73

Figure 47 : Comparison of 3D results obtained 15 and 30 days after moulding	74
Figure 48 : Impact-echo results	76
Figure 49 : Impact-echo signals (a) zone without defect (b) zone with clear interface peak	77

List of tables

Table 1 : Summary of non destructive testing methods (Courard et al. 2006)	18
Table 2 : Typical relative permittivity, electrical conductivity and velocity for common geologic materials (Annan 2005; Carino 2003; Soutsos et al. 2001; Bennett et al. 2009)	27
Table 3: Concrete slabs compositions.....	42
Table 4 : Sand patch test results	44
Table 5 : Comparison of sand patch test and ATOS results	47
Table 6 : Advantages and disadvantages of different CMP acquisition methods	54

Introduction

There is in Wallonia a total of 3500 bridges over highways, roads and waterways. Every one of them has to be carefully monitored. A specific inspection, visual and systematic, is planned every 3 years. If any sign of disorder is detected, a detailed inspection will be considered. During detailed inspections, every useful mean can be used to determine the nature and extent of the problem, including non-destructive techniques (Gilles and Toussaint 2007).

In 1985, a new kind of concrete bridge decks deterioration, named concrete decay, was observed for the first time. It occurs in both reinforced and prestressed bridges, mostly in beam-type structures. The thickness of those slabs is typically 18 cm, and they are protected by a waterproofing layer. In some situations, decay of decks slabs can ultimately lead to perforation of the slab (Mommer et al. 2004). As represented in Figure 1, a few new cases are still discovered every year.

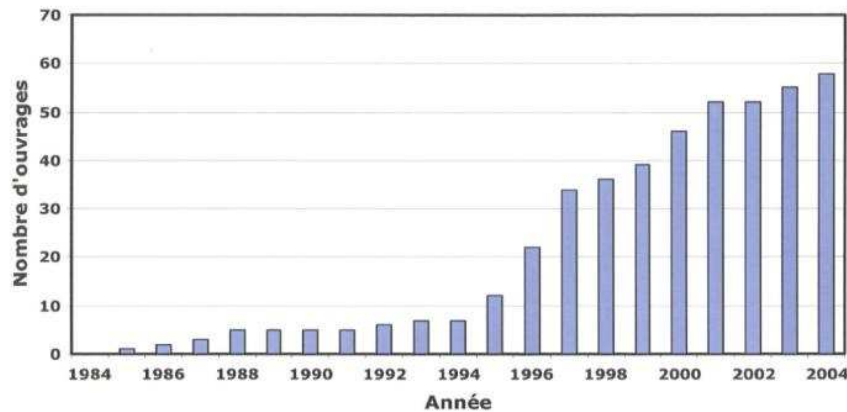


Figure 1 : Evolution of the number of cases of deck slabs decay in Wallonia (Gilles 2004)

The phenomenon generally develops down from the upper surface of the slab and creates two main types of degradation (Mommer et al. 2004):

- Concrete disintegration at the upper surface of the slab, at the interface slab/preslab or at the bottom surface of the deck: only the granular framework is remaining.
- Concrete delamination: concrete degrades into a few millimetres thick leaves, essentially at the upper surface of the slab, creating horizontal cracks (Figure 2 (c)).

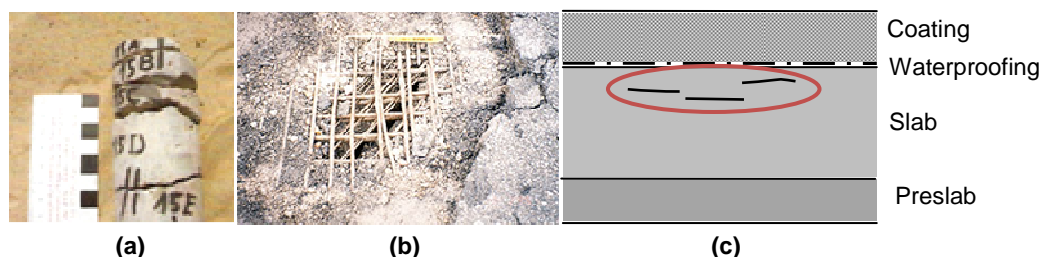


Figure 2 : Bridge deck delaminations (Gilles 2004; Demars et al.)

(a) Core drilled into a damaged deck (b) Slab perforation (c) Delaminations location

The delamination process is complex, involving several simple pathologies: freeze-thaw cycles, steel corrosion, carbonation, alkali-aggregates reactions... The development of all these processes requires the presence of water. They are thus firstly due to defects in the waterproofing (Demars et al.).

During visual inspection of the bridge, deck slab decay can be suspected if dark patches are visible on the inferior surface of the deck. Other factors as repetitive potholes formation into the asphalt layer or apparition at the surface of cement particles coming up from the slab can be other indicators of bridge deck decay (Mommer et al. 2004). The presence of delaminations can then be confirmed by core drilling for example (Figure 2 (a)), but every test is only representative of a little surface and causes damage to the structure.

In this context, in order to limit to a minimum the number of destructive essays, non-destructive techniques (NDT) of investigation, generally based on methods used in geophysics prospection, have been developed for a few years (Gagné 2009). They don't impair the function of the structure and permit regular testing at the same location to evaluate changes in properties with time. They can be calibrated on a small number of destructive tests and give a complete overview of the structure state (Carino 2003). Two non destructive techniques are particularly adapted to detect delaminations in concrete bridge decks: impact-echo and ground penetrating radar (GPR) (Gilles and Toussaint 2007). Those two methods will be investigated in the framework of this study, this report focusing on GPR while the impact-echo results are mostly described in Piotr Harassek's thesis.

To simulate bridge deck delaminations into laboratory samples, we will introduce various defects into concrete slabs. Then, we will determine GPR and impact-echo accuracy in the detection of the defects at the interface of the elements. We will try to improve the signals obtained with the two methods in order to extract as much information about the defects as possible. We will then compare the results given by the two methods and see if the results are similar or complementary.

This report will be divided into three parts. The first one will describe the state of the art in concrete degradation and repair, GPR and impact-echo. In the second part, the experimental aspect of the project, consisting mainly in the realization of the slabs and the auscultation procedure, will be described. The third and last part will eventually describe and analyze the different results obtained on the slabs with GPR, and compare them with the results obtained with impact-echo.

This work is complementary with the master thesis of Piotr Harassek, from Warsaw University of Technology. We will test the same samples, but Piotr will focus on impact-echo, while I will mainly concentrate on the GPR method. The signals will first be analyzed separately, before being compared in order to point out the differences between the two techniques.

Part 1: State of the art

1 *Degradations and repairs of concrete*

Concrete is generally considered as a durable material. Many structures built more than 50 years ago are still in an excellent state (Mays et al. 1992). Nevertheless, some factors can generate an early degradation of concrete constructions: alkali-aggregates reactions, freeze-thaw cycles, steel corrosion.... If in some cases a total replacement of the structure is needed, a majority of cases can be solved by a repair of the damaged zones (Gagné 2009). General anatomy of surface repairs is represented in Figure 3, and the different stages of the typical repair process are presented in this chapter.

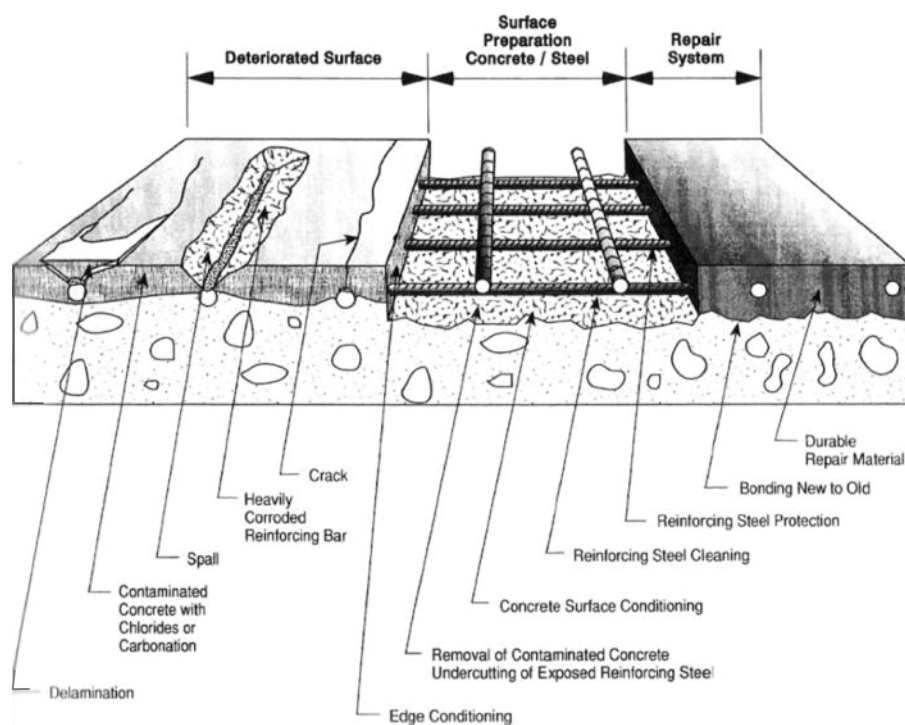


Figure 3 : Anatomy of surface repairs (Emmons and Emmons 1993)

1.1 Degradation mechanisms

As explained in the introductive paragraph, concrete bridge decks decay is a complex phenomenon, involving several simple processes of degradation. Those processes are numerous and result in visible defects as disintegration or delaminations into the slab. They are moreover really often function of climatic and exposure conditions. In concrete bridge decks, the most significant deterioration processes linked to environmental conditions are (Gagné 2009):

- intern leakage due to freeze-thaw cycles;
- armatures corrosion;
- alkali-aggregates reactions;
- sulphate reactions.

According to the European norm EN 1504-9, the identification of the cause or the causes of defects should be the first step of a complete structure assessment before a concrete repair (Raupach 2006). It is thus very important to understand the different mechanisms and their consequences on the concrete structures.

1.1.1 Freeze-thaw cycles

Freeze-thaw cycles may damage concrete if it is porous and is able to absorb water. Indeed, water involved into concrete will expand when transformed into ice and cause microcracking and localized tensions in concrete matrix. A concrete submitted to a high number of freeze-thaw cycles can lose its whole cohesion. The solution to avoid those problems is to use concrete with entrained air: this creates air bubbles inside concrete, in which water coming from the capillaries will have the possibility to expand without causing any damage (Gagné 2009; Emmons and Emmons 1993).

1.1.2 Armatures corrosion

Corrosion is an electrochemical process involving an anode, a cathode and an electrolyte. In the anodic zone, iron atoms dissolve into the interstitial solution as ions Fe^{2+} . This causes a local diminution of the section of the rebar. In the same zone, the electrical equilibrium requires the release of electrons:



These electrons travel then in the electrolyte as an electrical current and they are consumed in the reduction reaction with Fe atoms at the cathode, resulting in the precipitation of $Fe(OH)_2$ and in an increase in metal volume (up to 800%). The phenomenon is described in Figure 4. In reinforced concrete, steel rebars can provide both anode and cathode, and moist concrete matrix forms an acceptable electrolyte (Emmons and Emmons 1993; Mommer et al. 2004).

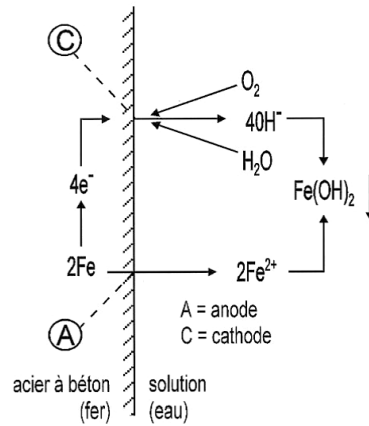
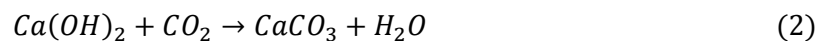


Figure 4 : Corrosion mechanism (Mommer et al. 2004)

Concrete is a high alkalinity material, in which the formation of a passivating film around reinforcing steel bars can take place, protecting them from corrosion. To observe corrosion in reinforcing bars, three different factors must be present simultaneously:

- An electrolyte with a high ionic conductivity;
- Oxygen in the cathode zone;
- Disruption of the passivating film by chlorides attack or carbonation.

If a passivating film appears around steel rebars into concrete, it is due to this high pH, situated about 12.5. A phenomenon susceptible to decrease this pH is carbonation. The process is the following one: the CO_2 naturally contained into the atmosphere dissolves into the interstitial water of the concrete at the surface of the structure and reacts with the lime contained into the concrete. The simplified reaction mechanism is:



The dissolution of CO_2 creates a decrease of pH to about 9. This is not damageable for the concrete itself, but at this pH, the passivating film is disrupted and steel corrosion can take place. For this reason, concrete carbonation is a very common cause of bridge degradation. An easy mean to reduce carbonation damages is to ensure the respect of concrete cover for the bottom surface of the slab, directly in contact with air (Mommer et al. 2004).

Another cause of passivating film disruption can be a chloride attack, which can permit corrosion of the steel bars even in a non-carbonated concrete. For this reason, de-icing salts can also play a role in corrosion process (Emmons and Emmons 1993).

In addition to the spoiling of the armatures themselves, with a diminution in their effective section, corrosion also damages surrounding concrete because of the volume change of corroded armatures in the cathode zone. In function of the corrosion level of the rebar, concrete tensile strength and quality of the concrete-rebar bond, this can lead to cracking, spalling and, in drastic cases, delaminations of concrete (Gagné 2009; Emmons and Emmons 1993).

1.1.3 Alkali-aggregates reactions

Alkali-aggregates reactions can occur when specific aggregates containing reactive forms of silica react with potassium, sodium and calcium hydroxide from cement paste and form gel around the aggregates. When submitted to moisture, this gel expands, creating microcracks in the surrounding concrete, which becomes less and less impermeable and allows an increasing quantity of water to reach the aggregates (Emmons and Emmons 1993; Lacroix and Calgaro 1999).

1.1.4 Sulfate reactions

This category regroups all reactions implying sulfate ions (SO_4^{2-}). These ions react with the cement compounds, resulting in the possible formation of two products: the ettringite and the thaumasite. The ettringite formation is a highly expansive phenomenon, which will cause cracking of the concrete. The thaumasite is not expansive, but it forms to the detriment of tobermorite, which is the highest resistant cement paste compound. This results in concrete disaggregation (Mommer et al. 2004).

As sources of sulfates, we can mention the presence of maritime environment, ground water, products storage, organic matter in decomposition and atmospheric pollution. Anyway, in some cases, the presence of sulfate reaction was observed without the presence of any of those factors, the sulfates coming then from the cement paste itself (Demars et al.).

1.1.5 Other degradation mechanisms

We can note that for all the pre-cited degradation mechanisms, water is an essential factor for the development of degradations. To those deteriorations due to environmental and exposure conditions, we should add degradation mechanisms due to other origins. They can generally be regrouped in four families (Gagné 2009):

- factors linked to structure conception;
- factors linked to construction conditions;
- factors linked to materials and concrete characteristics;
- factors linked to structure maintenance.

In the particular case of bridge decks in cold temperate climate areas, chloride contamination due to the use of road salt is considered likely to be the most serious cause of deterioration (Gagné 2009; Mays et al. 1992; INDOT 2007; Mommer et al. 2004). It is important to point out the cause of degradation before the repair. Indeed, it is generally impossible to evaluate the necessity to repair a structure or to choose a repair method without a complete identification of the origin of degradations and a setting up of protection strategies (Emmons and Emmons 1993).

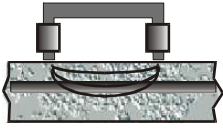
1.2 Locating delaminated concrete

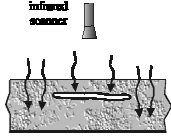
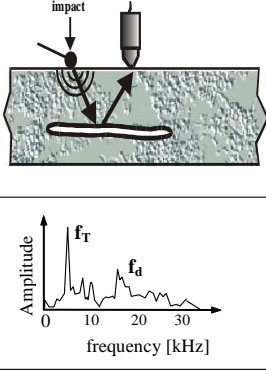
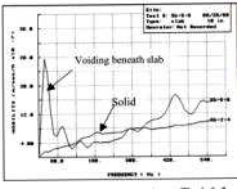
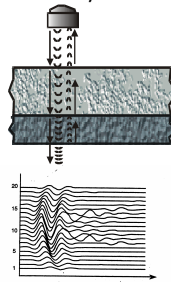
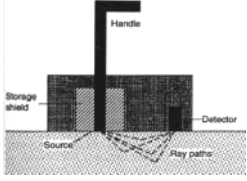
Damaged zones can be detected by removing the superficial layer on the whole deck. Anyway, it is often more interesting to locate those zones and evaluate their extent before the beginning of the heavy work. This is possible by visual inspection and non destructive techniques.

Any investigation campaign on a structure starts with a visual inspection. Key indicators of problems are for example surface degradation, water leakage, movements or metal corrosion (Emmons and Emmons 1993). A relationship has been established between degradation of the superior surface of the slabs and stains on the inferior surface, after a high number of cores drilling into damaged decks in Wallonia (Mommer et al. 2004). Anyway, if visual inspection reveals signs of concrete distress, further investigation is necessary.

A low cost and quite simple method to detect delaminations into concrete is acoustic sounding, using hammers or chain dragging to detect typical hollow sounds. When large horizontal areas are tested, chain dragging is often preferred to hammer-sounding which can be time-consuming. These methods can be used to give a general picture of the areas of delaminations, but they are generally insufficient to give the detailed layout required for reconstruction (Emmons and Emmons 1993).

Many other non destructive methods are available to detect defects in concrete structures, including GPR and Impact-Echo, the two techniques exploited in this study. Table 1 gives a general overview of the available non-destructive techniques, their principles, applications and limitations.

Methods and scheme	Principle	Application	Limitations
Acoustic impact various equipment from hammer or drag chain to electronic systems with auditory system	Impact of the object surface with implement; frequency and dumping of sounds indicate presence of defects;	Detection of debonds, delaminations, voids	Geometry and mass of object influence the results, low discrimination for auditory system
Electrical/magnetic methods (covermeters) 	Interactions between the bars and low frequency electromagnetic fields. Two principles: magnetic reluctance and eddy currents.	- Location reinforcing bars and estimation of the diameter and depth of cover - evaluation of moisture content in concrete	Expensive and specialized equipment, results depend on salt content and temperature changes
Fiber optics (video-endoscopy)	Using of fiber optic probe consisting flexible optical fibers, lens and illuminating system is inserted into drilled hole, cracks, new generation consist of additional CCD chip to improve image	Observation invisible parts of structure towards quality of joints, cracks, voids, aggregate, etc. possibility of multi- directional observation, high resolution images, possibility to register with camera	Expensive equipment, necessity of many holes to have adequate access

<p>Infrared Thermography, IT</p> 	<p>Measurement of surface temperature differences – thermographic image</p>	<p>Locating near-surface defects, like voids delamination and flaws,</p>	<p>Results depend on in-situ conditions (surface quality, wind speed and ambient temperature)</p>
<p>Impact-Echo, IE</p>  <p>$d = C_p / 2f_d$</p>	<p>Development of echo methods; mechanical, high energy impact used to generate the stress wave; high penetration of concrete, mainly by P wave; frequency analysis of recorded waveform using the fast Fourier transform</p>	<p>Evaluation of thickness of concrete slab and thick overlays, defect detection in concrete slabs, like delamination, flaws, large cracks, honeycombing, debonding, including quality of the bond between overlay and Base concrete estimation of depth of surface-opening cracks, including water-filled, detection and localization of other elements of the floor system like waterproofing isolation</p>	<p>Detection of large defects, relatively deeply located, needs expert for interpretation of results</p>
<p>Impulse-response method, IR</p> 	<p>Low-strain impact with instrumented rubber tipped hammer produces stress wave. Both the time trace of hammer force and the velocity transducer are processed into frequency using the fast Fourier transform. The “mobility” plot is constructed</p>	<p>Methods developed for evaluation of deep foundations and mass concrete stiffness measurements, quick scanning for flaws detection of concrete structures before lateral detail analysis eg. with I-E method</p>	<p>Results interpretation is delicate, unable to determine defects in shafts > 30m or with L/d > 30</p>
<p>Ground-Penetrating Radar, GPR</p> 	<p>Non-contact method; method analogous to UP-E techniques, except that pulses of electromagnetic waves are used instead of stress waves, results are register as a waterplot; can be used when only one side is available</p>	<p>Detection of delamination, locating reinforcing bars in structures, measurement of pavement thickness, measurements of water content of fresh concrete</p>	<p>Improper estimation of relative dielectric constant resulted in large error, needs expert for interpretation of results, results depends on in-situ conditions, e.g. presence of moisture and chlorides in concrete, expensive equipment</p>
<p>Nuclear (radioactive) methods:</p> 	<p>Methods involve a source of penetration, electromagnetic radiation and a sensor to measure the intensity of the radiation after it has travelled through the object. Two techniques available : direct transmission and backscatter radiometry</p>	<p>Evaluation of density of fresh and hardened concrete, could be used for reinforcement detection</p>	<p>Operator must be licensed, available equipment limited to path less than 300 mm (direct transmission) and 100 mm (backscatter r.), direct transmission needs drilling a hole and inserting the source of radiation</p>

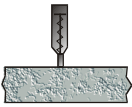
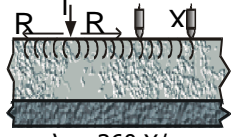
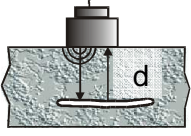
<p>Rebound hammer</p>  <p>$f_c = f(L)$; L- rebound index</p>	<p>Measurement of rebound height after striking concrete surface with spring loaded hammer; correlation between rebound index and compressive strength is determined</p>	<p>Evaluation of concrete substrate homogeneity, estimation of concrete substrate compressive strength according common procedure for concrete structure, monitoring strength gain</p>	<p>Evaluation of near-surface properties only, results depend on surface roughness, reference curve needed for strength estimation, rebound number affected by the orientation of the apparatus,</p>
<p>Spectral Analysis of Surface Waves, SASW</p>  <p>$\lambda_f = 360 X / \phi_f$ λ_f – wavelength for component frequency f X – distance between receiver; ϕ_f - phase angle of component with frequency f</p>	<p>Analysis of the spectrum of the disperse generalized Rayleigh surface wave in a layered system; the received signal is analyzed to obtained the dependence of phase velocity on the frequency</p>	<p>Determination of the stiffness profiles of flexible pavements, measurement of elastic properties of layered system, such a pavements, interlayered good or poor concrete</p>	<p>Necessity of comparison of the theoretical and experimental dispersion curves, time consuming procedure, difficulties in interpretation of the results</p>
<p>Ultrasonic pulse echo, UP-E</p>  <p>$d = v_p t / 2$</p>	<p>Propagation of a short pulse of ultrasonic wave; measurement of travel time to boundaries separating materials with different densities and elastic properties; by knowing the wave speed, v_p, the distance to the reflecting interface is calculated</p>	<p>Method developed to detect delamination, discontinuities, and small cracks; Measurements of slab thickness; Monitoring of polymer adhesive curing; Evaluation of thickness of polymer coating</p>	<p>Needs coupling agent, heterogeneous nature of concrete and of reinforcement presence result in multitude of echoes, difficult interpretation of results, relatively large "dead-zone"</p>

Table 1 : Summary of non destructive testing methods (Courard et al. 2006)

1.3 Surface preparation

When damaged zones are clearly determined in a structure, concrete of those zones has to be removed before surface preparation and repair material application. Concrete removal operations should lead to a clean, sound, uniform and cohesive concrete surface and to a global shape ensuring a good anchorage for the repair material. Corroded reinforcing bars should also be totally exposed, cleaned and protected by alkaline or cathodic protection (Emmons and Emmons 1993). Several methods can be used to remove partial depth of damaged concrete (Bissonette et al. 2006):

- Jack hammering
- Hydromilling
- Rotomilling
- Scabbling
- Steel shotblasting
- Abrasive sandblasting

Most of those methods are based on the low resistance of concrete under traction or impacts. One should select them as a function of site characteristics: tolerance to noise, dust and vibrations, depth and surface of concrete removal and accessibility. Quality of the obtained surface is also highly variable. Some methods can damage the substrate superficial concrete, by creating microcracks and decohesions, which can generate a decrease in the repair system adhesion (Gagné 2009; Garbacz et al. 2006; Emmons and Emmons 1993). It is especially the case for jack-hammering methods, creating an increasing number of cracks with the weight of the device (Bissonette et al. 2006). An easy mean to test the residual characteristics of the substrate concrete is to perform a test similar to the pull-off test before repair, provided that the test parameters are selected properly (Courard and Bissonette 2004).

To ensure a good bond between the substrate concrete and the repair material, the surface of concrete has to be clean, in order to have an open pore structure in which the repair material or the primer will be absorbed. With some concrete removal techniques as jack-hammering, such a surface is not achieved and a secondary surface preparation has to be performed, like sandblasting, shotblasting or hydroblasting. Those techniques enable to remove a very thin slice of concrete, allowing a better contact between substrate concrete and repair material (Gagné 2009; Emmons and Emmons 1993; Bissonette et al. 2006) .

Moisture level of the substrate may also be a key factor in bond quality achievement. Indeed, if the surface is totally dry, it will absorb too much water from the repair material, resulting in an excessive shrinkage. If the surface is completely damp, the water will clog the interface pores, preventing repair material penetration. It can also locally increase the E/C ratio, which will decrease repair material quality at the interface. A study run at the University of Liege proved that to get classical values of adherence at the interface, the saturation level of the support had to be comprised between 55% and 90%. (Courard et al. 1995)

1.4 Choice of repair material

The choice of the repair material has to be made carefully, taking into account several parameters. First, repair material has to have a physical, chemical and electrochemical compatibility with the substrate concrete. Dimensional compatibility between the two materials is also a key factor. The repair material should be chosen with a low drying shrinkage and a high creep, which can decrease cracking. Dilatation coefficient and elasticity modulus should also be as close as possible from those of substrate concrete. If dimensional compatibility isn't perfect, shear stress will develop at the interface, which has to have a sufficient shear strength (Gagné 2009).

Other parameters have to be taken into consideration in the choice of a repair material: repair thickness, need of impermeability, vibration requirement, surface appearance, material price, etc. Most of deep repairs are realized using Portland cement binders and well-proportioned aggregates. Properties of those cement-based repair materials can be modified by the use of pozzolans or polymers as latex.

Durability of repairs depends on the quality of repair materials and their ability to resist to physical, chemical and mechanical attacks, but also and mostly on the quality of the bond between the repair layer and the substrate slab. This last point is the more susceptible to cause durability problems. Adherence quality is thus considered by numerous authors as a repair longevity guarantee (Gagné 2009).

To ensure a good bond between substrate concrete and repair material, preliminary laboratory tests can be carried out. Three different test methods are currently in use: slant shear test, direct shear method and uniaxial tensile test. The two first tests are mostly representative of the shear resistance of the interface, when the latter is representative of its tensile resistance. It is the laboratory equivalent of pull-off test, used in situ after repair (see §1.6). By these methods, compatibility of repair and substrate materials can be evaluated, as well as the efficiency of surface preparation and bonding agent application (Emmons and Emmons 1993).

Indeed, in some cases, a bonding agent can be applied on the concrete surface before the application of the repair material. It must be easily absorbed into the open-pore structure and has to be compatible with both repair and substrate materials. Three different types of products are frequently used: cement-based slurries (for cement-based repairs), latex emulsions and epoxies. If those bonding agents are supposed to increase bond quality, they can also constitute a source of additional problem. Thus, they never dispense from bond quality evaluation after repair (Emmons and Emmons 1993).

1.5 Repair placement methods

Once the surface is prepared and the repair material chosen, we can proceed to the repair itself. A wide range of placement techniques are available; the choice of one or another mainly depends on the geometry of the repair. For vertical repairs, a first solution is to place a formwork in front of the damaged zone and to cast the repair material, which should have a sufficient workability, into the prepared cavity. This cast-in-place (Figure 5 (a)) method is widespread and requires a sufficient repair depth.

Recently, the possibility to cast the new material between the substrate material and a formwork was extended to non-vertical surfaces. This is the form and pump method (Figure 5 (b)), in which the repair material is pumped to fill the cavity from its bottom or from one side. To achieve a good bond between the substrate concrete and the repair material, the cavity should have very neat boundaries. A wide range of materials (concretes, mortars, PCCs) can be pumped and placed with this technique.

A last variation of those methods involving casting behind a formwork is the grouted preplaced aggregates technique (Figure 5 (c)). In this method, a quite liquid grout is pumped into the cavity which had been previously filled in with the washed and gap-graded aggregates. The mortar grout can then fill the cavities between the aggregates. This method ensures a very low shrinkage, because of the point-to-point contact between the aggregates, but the placement has to be made by an experimented builder.

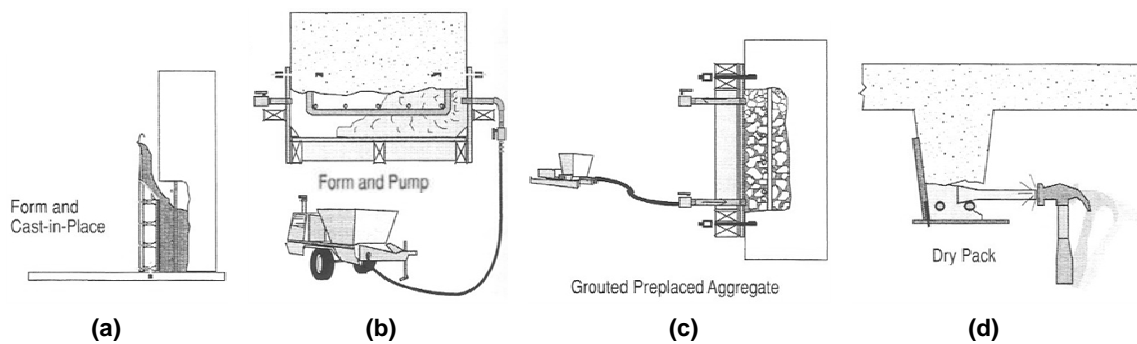


Figure 5 : Repair placement methods (Emmons and Emmons 1993)

Another method to place concrete is the dry packing (Figure 5 (d)). The concrete or mortar placement is achieved manually, by compaction with a hardwood stick and a hammer. The consistency of the repair material has to be such that one can easily mold it into a ball shape. Thanks to the low water content, this method ensures a low shrinkage but quality controls are difficult to set up. It is also possible to apply specifically designed repair materials with a trowel on vertical or overhead surfaces. This hand-applied method is useful for low repair depths, in which the steel rebars are not involved.

For vertical and overhead surfaces, we can also mention the dry and wet shotcrete methods, consisting in a projection of the repair material directly on the surface to be repaired, without any formwork. The difference between dry and wet shotcrete is that for dry shotcrete the water is only added at the nozzle while in wet shotcrete the water is premixed with the dry materials. This type of placement has to be executed by a professional operator in order to minimize the placement defects associated to the method, as for example the formation of low compaction zones behind the rebars.

The easiest configuration for repair material placement is the case of horizontal surfaces. For many buildings as bridges or parking structures, screeds are used to level, consolidate and restore the overlay materials. The thickness of the overlays ranges from a few millimeters to several centimeters. In most of cases, additional reinforcement is not required, but the quality of bonding is particularly important. Almost all the types of repair materials can be used for overlays. (Emmons and Emmons 1993; Courard 2008)

1.6 Repair quality testing

If one of the repair stages is not carried out properly, the bond between the repair material and the substrate slab can be very low. For example, if the repair material is submitted to an important shrinkage, the adherence between the two materials can be partially or totally disrupted. For this reason, it is important to test the quality of repairs after their applications (Courard and Bissonette 2004; Gagné 2009). After stiffening of the new concrete or mortar, the quality of the repair is generally determined by pull-off testing. In this destructive method, a core is drilled into the substrate layer through the surface layer. A tensile force is then

applied to this core until the failure occurs (Figure 6). If it takes place at the interface, it reflects the tensile bond between the two materials.

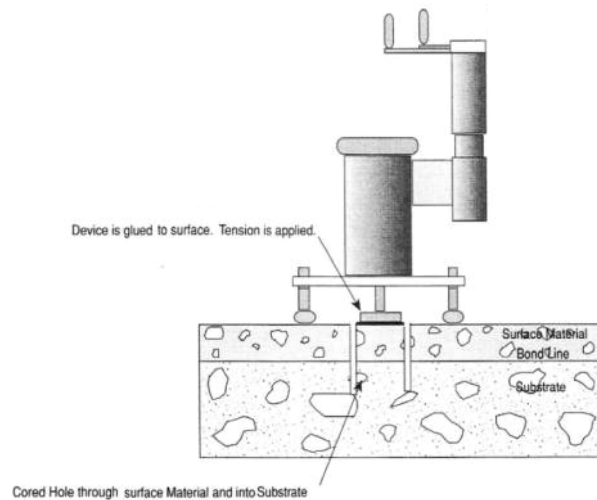


Figure 6 : Pull-off testing (Emmons and Emmons 1993)

Pull-off results are greatly influenced by aggregate size, core depth and plate diameter, so results are best used as qualitative review of the bond between materials, which is sufficient to detect early delaminations in concrete repairs. The greatest problem with pull-off test is that it can only be performed in a few punctual points, because it causes damages to the newly-renovated structures. For this reason, it is only partially representative of the adherence in the whole structure (Emmons and Emmons 1993; Carino 2003; Courard and Bissonette 2004).

To compensate for this drawback, we can use non-destructive techniques. Most of the techniques describe in Table 1 can be used to detect early delaminations after concrete repair. This is also the case for GPR and Impact-Echo. The only limitation for those devices is the thickness of repair: very shallow delaminations will be difficult to detect with both techniques. In both cases, the minimum thickness seems to lie from 5 to 7 centimeters. For GPR, this will probably decrease in the future, with the production of devices emitting in higher frequencies.

2 GPR

GPR, or Ground Penetrating Radar, is a non-destructive evaluation technique used in soil prospection since the sixties. This method is frequently used for ice studies, archaeological research and, since the eighties, it has been increasingly used in concrete elements characterization. Initial civil engineering applications included condition assessment of highway pavements and their foundations, with applications to structural concrete focussing on inspection of bridge decks (Bungey 2004).

GPR principle is to create, with an emitter antenna, very short pulses of electromagnetic waves which propagate through the medium and reflect on the interfaces between materials of different electromagnetic properties. This is illustrated in Figure 7. The reflected signal is registered by a receiver antenna at the surface. By measuring the time interval between wave emission and reception of the echo, the depth of the interface can be determined if the wave speed in the material is known, and vice-versa. By using this method, voids, humid zones and material changes can be detected.

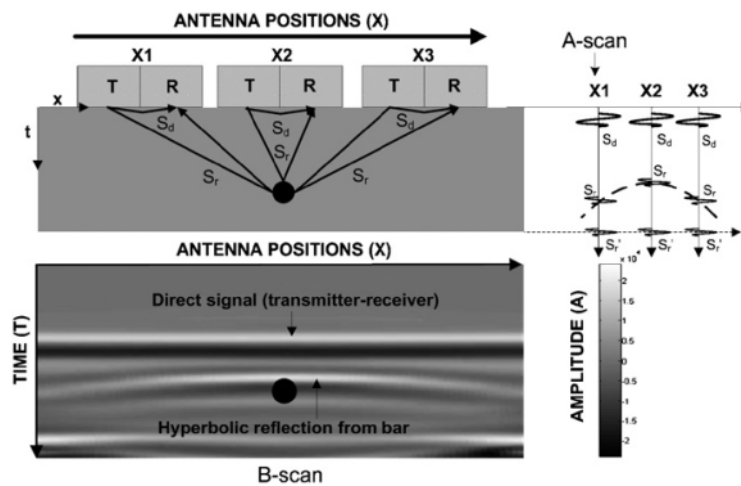


Figure 7 : Radar principle (Viriyametanont 2008)

In electromagnetic spectrum, radar frequencies range from 100 MHz to 100 GHz. For geological applications, in which penetration depth has to be quite important, frequencies of antennas are generally inferior to 500 MHz. For civil engineering applications, useful frequencies can rise up to 2.6 GHz. (Viriyametanont 2008; Reynolds 1997)

2.1 Propagation of electromagnetic waves

The physical properties of the material and the electromagnetic field are related by three constitutive equations:

$$\vec{j} = \sigma \cdot \vec{E} \quad (3)$$

$$\vec{d} = \varepsilon \cdot \vec{E} \quad (4)$$

$$\vec{b} = \mu \cdot \vec{H} \quad (5)$$

Where:

- \vec{j} is the electric current density vector (A/m²)
- σ is the electric conductivity (S/m)
- \vec{E} is the electric field strength vector (V/m)
- \vec{d} is the electric displacement vector (C/m²)
- ε is the dielectric permittivity (F/m)
- \vec{b} is the magnetic flux density vector
- μ is the magnetic permeability (H/m)
- \vec{H} is the magnetic field vector (A/m)

Equation (3) describes how free charges flow to form a current when an electric field is present. In concrete, electric conductivity is linked to the number, the charge and the speed of ionic particles moving under the electric field action and the concrete porous structure characteristics.

Equation (4) describes how constrained charges are displaced in response to an electric field. This movement creates a dielectric displacement current, proportional to the temporal derivative of electric field:

$$\vec{j}_d = \frac{d\vec{d}}{dt} = \varepsilon \cdot \frac{d\vec{E}}{dt} \quad (6)$$

Equation (5), the last constitutive equation, describes the magnetic field influence on intrinsic atomic and molecular magnetic moments. Concrete being a non-magnetic material, μ is equal to μ_0 , void permeability. Thus, this third equation won't be useful in applications related to this material (Annan 2005).

Conductivity and permittivity are complex values depending on field frequency (f).

$$\sigma(\omega) = \sigma'(\omega) + i\sigma''(\omega) \quad (7)$$

$$\varepsilon(\omega) = \varepsilon'(\omega) - i\varepsilon''(\omega) \quad (8)$$

Where:

$$\omega = 2\pi f \quad (9)$$

$$i^2 = -1 \quad (10)$$

It is impossible to distinguish experimentally in radar frequency range contributions of electric conductivity from dielectric permittivity in total current density. Therefore, effective parameters σ_e and ε_e are defined to take into account both effects (Viriyametant 2008):

$$\varepsilon_e = (\varepsilon'_e - i\varepsilon''_e) = \left(\varepsilon' + \frac{\sigma''}{\omega} \right) - i \left(\varepsilon'' + \frac{\sigma'}{\omega} \right) \quad (11)$$

$$\sigma_e = (\sigma'_e + i\sigma''_e) = (\sigma' + \omega\varepsilon'') + i(\sigma'' + \omega\varepsilon') \quad (12)$$

Generally speaking, σ and ε are tensors and can be non linear. Indeed, they can be dependent on electric field magnitude and direction. Anyway, for GPR applications, those parameters are generally treated as field independent scalar quantities (Annan 2005). Experimental works proved that this assumption is close to reality when high frequencies are employed (Soutsos et al. 2001).

Then, total current density \vec{j} generated by the application of the electric field \vec{E} can be expressed as a function of effective conductivity or effective permittivity:

$$\vec{j} = \sigma_e \vec{E} = i\omega\varepsilon_e \vec{E} \quad (13)$$

Generally, permittivity is expressed as a relative value, by dividing it by ε_0 , void permittivity:

$$\varepsilon_r = \frac{\varepsilon_e}{\varepsilon_0} = \varepsilon'_r - i\varepsilon''_r \quad (14)$$

The real part of relative permittivity ε'_r represents the material capacity to accumulate electric energy by electric polarization. It is usually defined as the concrete dielectric constant. The imaginary part ε''_r represents energy losses by absorption, resulting from combined effects of σ' and ε'' .

In radar frequency range, different polarization mechanisms can take place (Bourdi et al. 2008):

- electronic polarization due to the distortion of the electronic cortege of an atom with respect to its nucleus;
- ionic polarization due to the relative motion of anions and cations within a crystalline structure;
- dipole polarization, linked to water molecules in concrete constituting permanent dipoles;
- interfacial polarization, linked to charge accumulation at solid-liquid interfaces.

The first two phenomena are applicable to all solids. In case of concrete, they dominate in the absence of dipole particles i.e. in dry conditions. In presence of water, dipole polarization, which is related to water content, has the greatest importance and electronic and ionic polarization can be neglected. The dominating influence of water content on relative permittivity was experimentally confirmed by Soutsos (see § 2.6.1).

Interfacial polarization is linked to the ionic concentration in interstitial solution but is characterized by very low relaxation frequencies (1-100 KHz). At radar frequencies, it doesn't have time to settle and doesn't contribute to the total permittivity, even if it has a great influence on conductivity (Bourdi et al. 2008).

The amplitude of the electromagnetic waves doesn't remain constant during propagation, but is submitted to attenuation. The attenuation factor α describes this diminution caused by electromagnetic losses in function of the covered distance x (Reynolds 1997):

$$\frac{E_0}{E_x} = e^{-\alpha x} \quad (15)$$

In this equation, E_0 is the initial electromagnetic field strength and E_x is the electromagnetic field strength at a distance x . The attenuation factor depends on the dielectrical and electrical properties of the medium (equation (16)).

$$\alpha = \omega \left\{ \left(\frac{\mu \varepsilon}{2} \right) \left[\left(1 + \frac{\sigma^2}{\omega^2 \varepsilon^2} \right)^{\frac{1}{2}} - 1 \right] \right\}^{1/2} \quad (16)$$

The ratio $\sigma/\omega\varepsilon$ is defined as the loss factor. When we have a low loss medium,

$$\frac{\sigma}{\omega \varepsilon} \ll 1 \quad (17)$$

The attenuation coefficient can then be written in the simple form:

$$\alpha = \frac{\sigma}{2} \sqrt{\frac{\mu}{\varepsilon}} \quad (18)$$

2.2 Speed of electromagnetic waves

By introducing the constitutive equations (3), (4) and (5) into Maxwell's equations, it is possible to obtain a differential equation describing the spatial/temporal variations of the electric field (Annan 2005):

$$\frac{\partial^2}{\partial \beta^2} f(\beta, t) - \mu \sigma \frac{\partial}{\partial t} f(\beta, t) - \mu \varepsilon \frac{\partial^2}{\partial t^2} f(\beta, t) \equiv 0 \quad (19)$$

Where f is a function describing the electric field, function of t , time, and β , the scalar distance in the direction that the field varies. In the case of a low-loss medium such as concrete in radar frequency range, losses can often be neglected, which means that we assume $\sigma \equiv 0$. The differential equation can then be solved and we have:

$$v = \frac{1}{\sqrt{\varepsilon\mu}} \quad (20)$$

In this equation, $\mu = \mu_0$ and $\varepsilon = \varepsilon_r \varepsilon_0$. By introducing the speed of light

$$c = \frac{1}{\sqrt{\varepsilon_0 \mu_0}} = 0.3 \text{ m/ns} \quad (21)$$

and neglecting the effects of the imaginary part of the effective dielectric permittivity ε_r'' , which is possible because concrete is a low-loss medium, the wave velocity can be finally approximated as:

$$v = \frac{c}{\sqrt{\varepsilon_r'}} \quad (22)$$

Table 2 gives typical values of relative permittivity, conductivity and velocity for common geological materials and the different materials that will be encountered during this study:

Material	ε_r'	σ (mS/m)	v (m/ns)
Air	1	0	0.30
Distilled water	80	0.01	0.033
Fresh water	80	0.5	0.033
Sea water	80	3000	0.01
Dry sand	3-5	0.01	0.15
Saturated sand	20-30	1-10	0.06
Limestone	4-16	0.5-2	0.075-0.15
Silts	5-30	1-100	0.05-0.13
Clays	5-40	2-1000	0.05-0.13
Granite	4-7	0.01-1	0.11-0.15
Concrete	4-10	0.01-0.12	0.09-0.15
Polystyrene	2.6	$<10^{-10}$	0.19
Polyethylene	2.3	$<10^{-10}$	0.20
Oil	2.2-2.8	$<10^{-10}$	0.18-0.2

Table 2 : Typical relative permittivity, electrical conductivity and velocity for common geologic materials (Annan 2005; Carino 2003; Soutsos et al. 2001; Bennett et al. 2009)

2.3 Reflection coefficient

The amplitude of the reflected wave at an interface is given by the reflection coefficient. It depends on the difference between the relative permittivities of the two materials:

$$R_{1,2} = \frac{\sqrt{\varepsilon_{r1}} - \sqrt{\varepsilon_{r2}}}{\sqrt{\varepsilon_{r1}} + \sqrt{\varepsilon_{r2}}} \quad (23)$$

This coefficient can be negative if material 2 (the lower layer) has a higher relative permittivity than material 1 (the upper layer), which is the case for embedded metallic rebars for example, whose dielectric permittivity approaches the infinity. At an interface between air and concrete, reflection coefficient is about 50%, which means that GPR waves are able to penetrate beyond such interfaces and detect deeper features in the material. This is not possible with other non destructive techniques such as impact-echo or ultrasonic testing, because they use stress waves which have an air-concrete reflection coefficient almost equal to 100%.

2.4 Results display and analysis

Each measurement made by the receiving antenna is called a sample. The set of all the samples collected at the same point is called a trace or a scan (Figure 8). On each scan, we can observe the direct wave and the waves reflected on the different interfaces. In reality, the signal is affected by a residual noise, which can be decreased by the stacking of several measurements made at the same point. With this method, the peaks corresponding to noise, situated at random positions, will disappear.

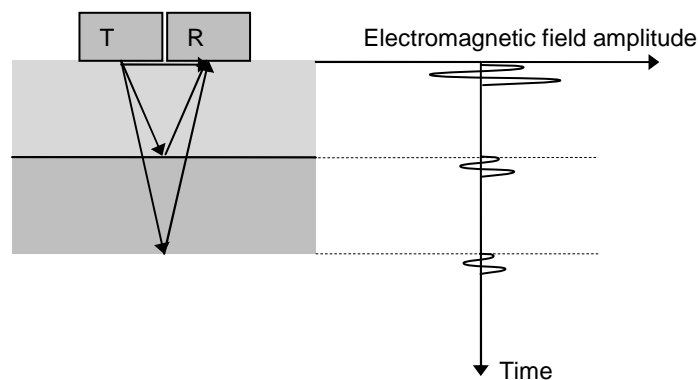


Figure 8 : Radar scan

Two different modes of acquisition can be used in radar testing. In the first one, the transmitter and the receiver are moved together along the surface. This enables to obtain a direct representation of the corresponding profile. The second mode of acquisition uses varying offset between the antennas. With this method, one can focus on a precise point of reflection into the structure and evaluate the speed of the waves into the tested material. The next two chapters will describes those two modes of acquisition.

2.4.1 Profile scanning

In this type of structure radar auscultation, the transmitter and the receiver are moved together along a defined line of the structure surface. The user defines the spatial interval separating all the traces recordings. All the scans taken altogether and represented as

function of their position x constitute a profile (Figure 9). This is the most common way of visualization of radar results.

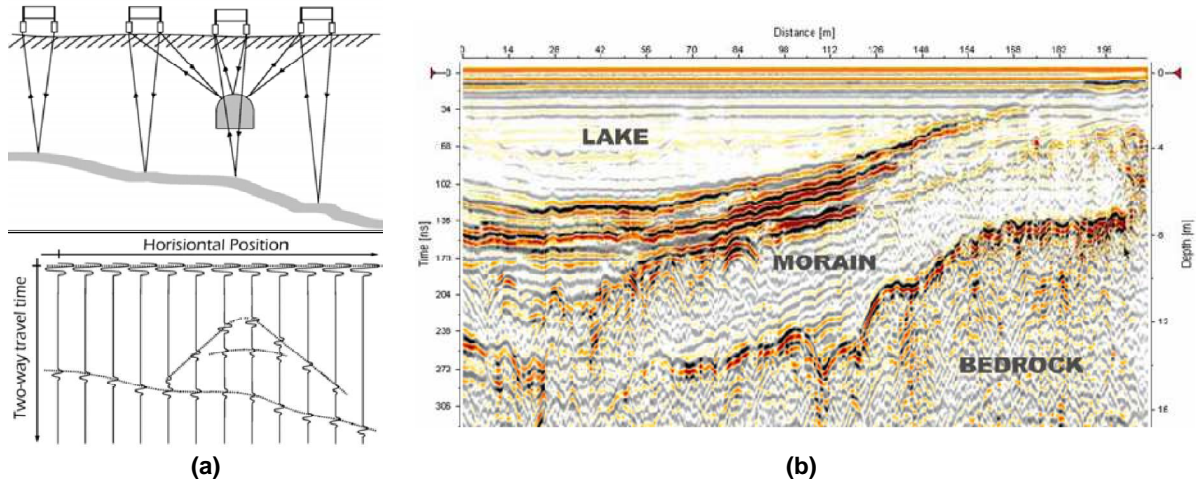


Figure 9 : Radar profiles
(a) Scheme of principle (b) Real example (Mala)

If the offset is constant, we can deduce the depth of the reflection z from the two-way travel time t displayed on the radargram:

$$z = \frac{\sqrt{t^2 v^2 - x^2}}{2} \quad (24)$$

If the distance between the two antennas x is short by comparison to the depth of the target z , this equation becomes simply:

$$z = \frac{t v}{2} \quad (25)$$

2.4.2 CMP acquisition principle

The other mode of acquisition is CMP, in which the reflection point remains constant and the offset is gradually increased (Figure 10).

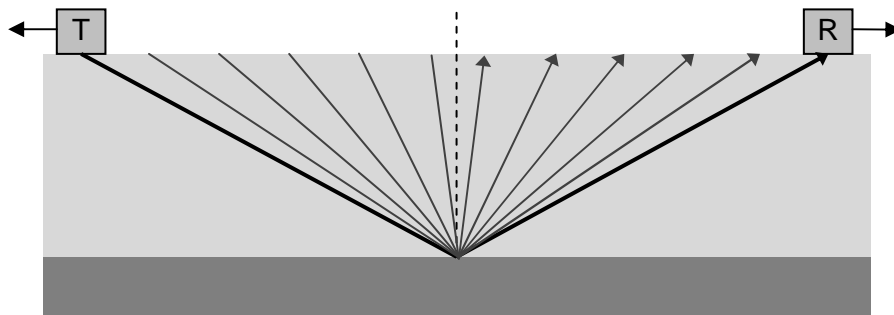


Figure 10 : CMP acquisition principle

In the radargram obtained with this acquisition mode (Figure 11), we can recognize characteristic waves, whose equation can be calculated.

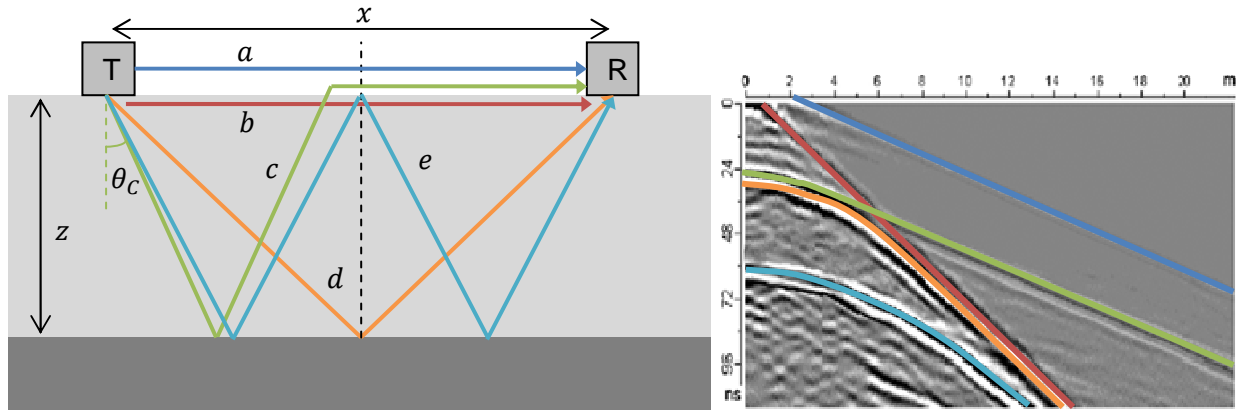


Figure 11 : Typical radargram obtained with CMP (Mala)

Wave a is the direct wave in the air. Its speed is known and equal to the speed of light $c = 30 \text{ cm/ns}$. It is supposed to cross the origin of axes, thus it can help to find the time zero if the initial offset is known. The equation of this wave is:

$$t_a = \frac{x}{c} \quad (26)$$

Wave b is the direct wave into the ground. It gives directly the speed v of the radar waves into the material. Its equation is

$$t_b = \frac{x}{v} \quad (27)$$

Wave c is the critically refracted wave. This wave travels into the ground with an incident angle equal to θ_c , the critical angle, which is the incident angle corresponding to an horizontal path into the air. At every interface, refraction laws stipulate that we have:

$$\frac{1}{v_1} \sin \theta_1 = \frac{1}{v_2} \sin \theta_2 \quad (28)$$

In our case, material 1 is concrete and material 2 is air, thus if $\theta_1 = \theta_c$, θ_2 should be equal to 90° . It gives us the value of θ_c :

$$\frac{\sin \theta_c}{v} = \frac{\sin 90^\circ}{c} = \frac{1}{c} \quad (30)$$

$$\theta_c = \arcsin \frac{v}{c} \quad (31)$$

If the offset is inferior to $2z \tan \theta_c$, the critically refracted wave is coincident with the first reflected wave d . If the offset x is superior to this value, the time of travel of the wave is equal to the constant time of travel through the concrete plus the time of travel in the air:

$$t_c = \frac{2z}{v \cos \theta_c} + \frac{x - 2z \tan \theta_c}{c} \quad (32)$$

First reflected wave d is a function of the offset and the speed into the material. Its equation is:

$$t_d = \frac{2\sqrt{z^2 + \frac{x^2}{4}}}{v} \quad (33)$$

Finally, secondly reflected wave e has exactly the same parameters than the first reflected wave. Its equation is

$$t_e = \frac{4\sqrt{z^2 + \frac{x^2}{16}}}{v} \quad (34)$$

Of course, an infinite number of reflection multiples on the first interface can be represented in the same way. Anyway, because of the attenuation into the material, the number of visible multiples is quite limited.

2.5 Resolution

2.5.1 Vertical resolution

The vertical resolution of the radar, also called longitudinal, range or depth resolution, depends mainly on the length of the emitted pulse, which is inversely related to the bandwidth of the wave:

$$\lambda = \frac{v}{f} \quad (35)$$

Two different reflections will appear as distinguishable events if the reflected pulses are clearly separable on the radargram. Two different methods are applied to determine the vertical resolution. The simplest one (Pérez-Gracia et al. 2008a) simply proposes to choose the wavelength λ as the vertical resolution. A more complicated method (Annan 2005) proposes to use the width of the pulse at half amplitude W (Figure 12). According to the authors, the peaks should be distinguishable if the time separation between the pulses is higher than $W/2$. The vertical resolution Δr is then obtained by equaling the differential time between the two wave arrivals to the half half-width $W/2$. The vertical resolution is then equal to:

$$\Delta r = \frac{Wv}{4} \quad (36)$$

Theoretically, Δr is thus independent of the reflection depth. Anyway, in practical purposes, the resolution will decrease at larger distances, due to pulse dispersion and attenuation (Annan 2005).

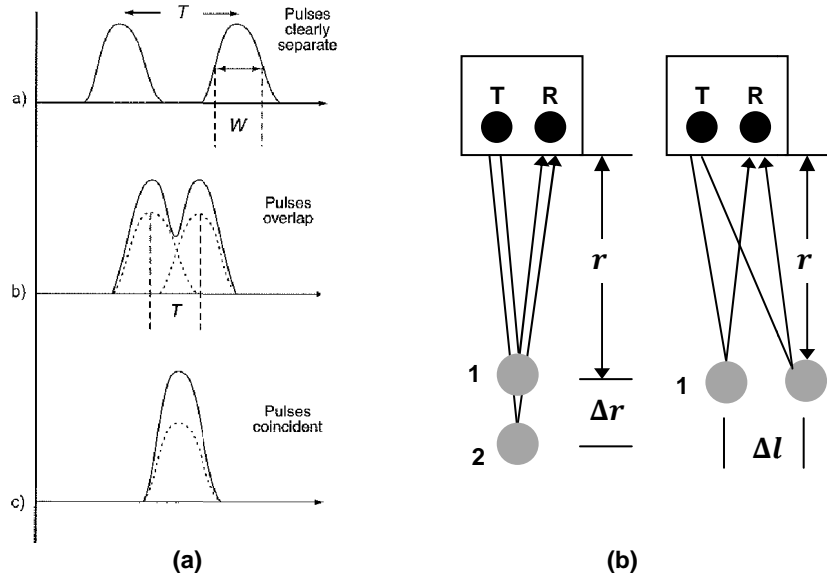


Figure 12 : Peak separation in the radargram (a); Range and lateral resolution (b) (Annan 2005)

The detection of thin layers embedded into concrete depends mainly on their reflection coefficient and not on the thickness of the layer. Indeed, a very thin sheet of metal will always generate a total reflection, while a 10 cm thick layer of a material having the same properties as the substrate concrete won't be detected. It depends on the reflection coefficient (cf. § 2.3). Nevertheless, the thickness of the layer has an influence on the possibility to evaluate the thickness of the layer. The ability to resolve the thickness requires the layer thickness to be at least in the order of one wavelength (Annan 2005). For 2.3 GHz into concrete, for example, the minimum thickness of the embedded layer should be at least 4 cm in order to be determined.

2.5.2 Horizontal resolution

Horizontal (or lateral) resolution can be determined the same way as vertical resolution, by equaling the time difference between the two wave arrivals and half the half-width $W/2$. If the lateral offset is small compared to the depth of the targets, we obtain (Annan 2005):

$$\Delta l = \sqrt{\frac{vdW}{2}} \quad (37)$$

In this equation, we can see that the lateral resolution depends on the depth of the target: the larger the distance, the lower the lateral precision.

Another approach is to consider the horizontal resolution equal to the Fresnel zone radius for signals related to the center frequency f_c . First Fresnel zone is the finite-sized footprint of the

wave, travelling in a cone of radiation, on any interface (Figure 13). If a feature has a smaller dimension than this first Fresnel zone, it won't be pictured (Reynolds 1997).

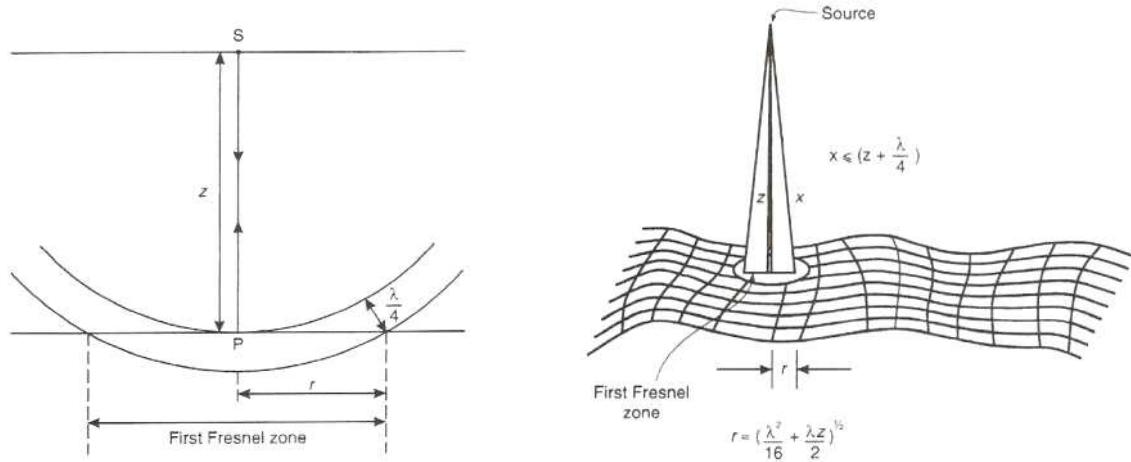


Figure 13 : First Fresnel zone (Reynolds 1997)

From Figure 13, we have:

$$\Delta l = \sqrt{\frac{\lambda_c^2}{16} + \frac{\lambda_c d}{2}} \quad (38)$$

Where λ_c is the wavelength associated with the center frequency of the antenna. If λ_c is small in comparison to the depth, we obtain:

$$\Delta l = \sqrt{\frac{d\lambda_c}{2}} \quad (39)$$

This equation is identical to the previous one if we use the relationship between the pulse width and the center frequency:

$$W = \frac{1}{f_c} = \frac{\lambda_c}{v} \quad (40)$$

The two expressions of horizontal resolutions described in equations (38) and (39) were compared to experimental data obtained on concrete samples by Perez-Gracia & al. (Pérez-Gracia et al. 2008b). They also compared the results to other equations, expressing the First Fresnel zone as an ellipse or including the attenuation coefficient. The results obtained with the equations previously described give a good estimation of the minimum distance to detect two targets with no or small interferences. Anyway, it is possible to detect the presence of two different targets for a shorter distance, which is better described by elliptical first Fresnel zone equations.

2.6 Determination of concrete electromagnetic parameters

2.6.1 Direct measurement

Works were set up (Soutsos et al. 2001) in order to determine dielectric properties of concrete by direct measurement, with a coaxial transmission line. It was shown that relative permittivity of concrete depended on both water content and frequencies, but the influence of frequency is weak for high frequencies.

Soustos et al. also proved that cement type and concrete strength has a minor influence on results, especially on relative permittivity. The main influent factor turned out to be the water content of the samples.

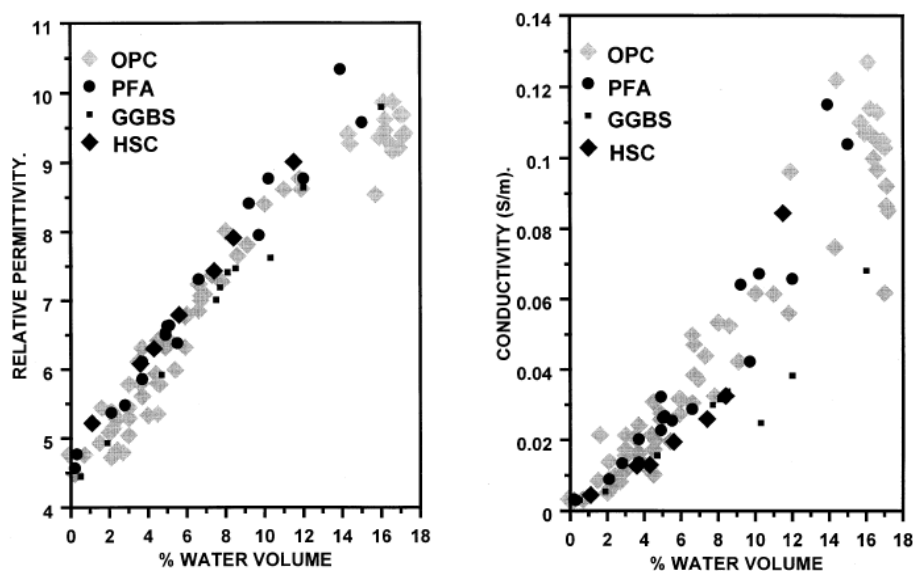


Figure 14: Influence of water content on dielectric properties (Soutsos et al. 2001)

Finally, the influence of steel fibers, chlorides and honeycombed concrete was studied. Steel fibers and honeycombed concrete have an influence on samples permittivity and conductivity, while chlorides only modify the conductivity.

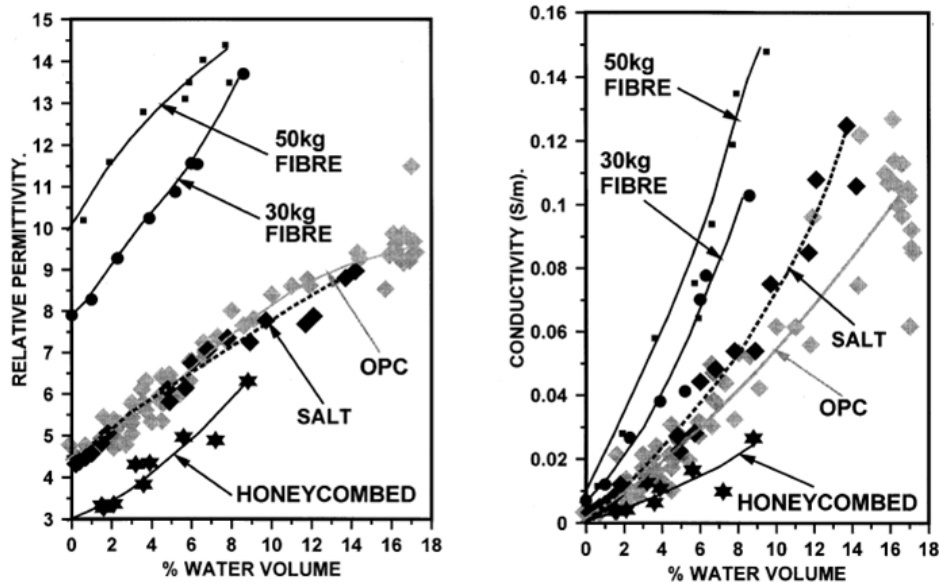


Figure 15: Influence of steel fibers, honeycombing and salts on dielectric properties (Soutsos et al. 2001)

2.6.2 Indirect evaluation by speed experimental measurement

Dielectric properties of concrete can be evaluated by measurement of the propagation speed of the direct wave in the material. Two different techniques are described by Klysz & al. (Klysz et al. 2008).

The first one is a direct measurement of the propagation speed of the wave maximum energy, estimated from eleven different receiver positions. This could approach real velocity even if dispersion and attenuation can modify the shape of the wave and thus the velocity measurement.

The second one is based on the spectral analysis of the radar surface wave. The use of a Fourier transform frees calculations from changes in the shape of this wave during its propagation. However, this technique is more complicated and is submitted to more noise because only one pair of receivers can be taken into account after each measurement.

It was shown that both methods tended to underestimate the permittivity value for the lowest water content (i.e. for low permittivity values and high wave speed), because it is then difficult to separate contributions of direct wave in the material from direct wave in the air.

2.6.3 Indirect evaluation by resolution of the inverse problem

Ferrieres & Klysz (Ferrieres et al.) showed it is possible to evaluate dielectric properties of concrete with an indirect method. The principle is to adjust electromagnetic parameters in order to fit the experimental results obtained on concrete slabs to the numerical simulation results. Those ones were obtained with a 2D FDTD wave propagation model. The results were in good accordance with experimentally measured dielectric properties.

2.6.4 Extrapolation of experimental results with Jonscher model

To take into account the variation of dielectric properties of concrete with frequency, we can use Jonscher model. The three parameters model uses as variables:

- n , an empirical parameter without dimension that characterizes the change in amplitude as a function of frequency;
- χ_r , the real part of the dielectric susceptibility to the frequency reference;
- ε_∞ , the limiting high-frequency value of the real part of the effective permittivity. It is constant and real and describes the mechanisms of polarization that rapidly respond to the application of an electric field.

This model permits to take into account the variation of dielectric properties with the radar frequency. It was validated on mortar and concrete by Bourdi. (Bourdi et al. 2008) and gives very good results for different moisture levels, heterogeneities and porosities.

2.7 Applications of GPR to concrete structures

GPR is now recognized as a useful tool in concrete structures characterization. The widespread applications generally focus on the geometrical characterization of the structures: thickness determination (Al-Qadi and Lahouar 2005), detection of defects such as delaminations or cracks, localization of reinforcing bars. Recent works also showed that radar could be used for the characterization of the material itself, which opens new application fields: detection of humid or salt-contaminated zones (Hugenschmidt and Loser 2008), measurement of the water content (Dérobert et al. 2008). (Bungey 2004; Balayssac et al. 2007).

2.7.1 Example of GPR survey results

A good example of the possibilities opened by GPR utilization on concrete structures is given by Péres-Gracia (Pérez-Gracia et al. 2008a) for the inspection of the reinforced concrete base of a block of flats. The slabs of the underground parking of the buildings showed evidence of moisture and numerous cracks were visible at the surface. The building was scanned with 40 different GPR profiles.

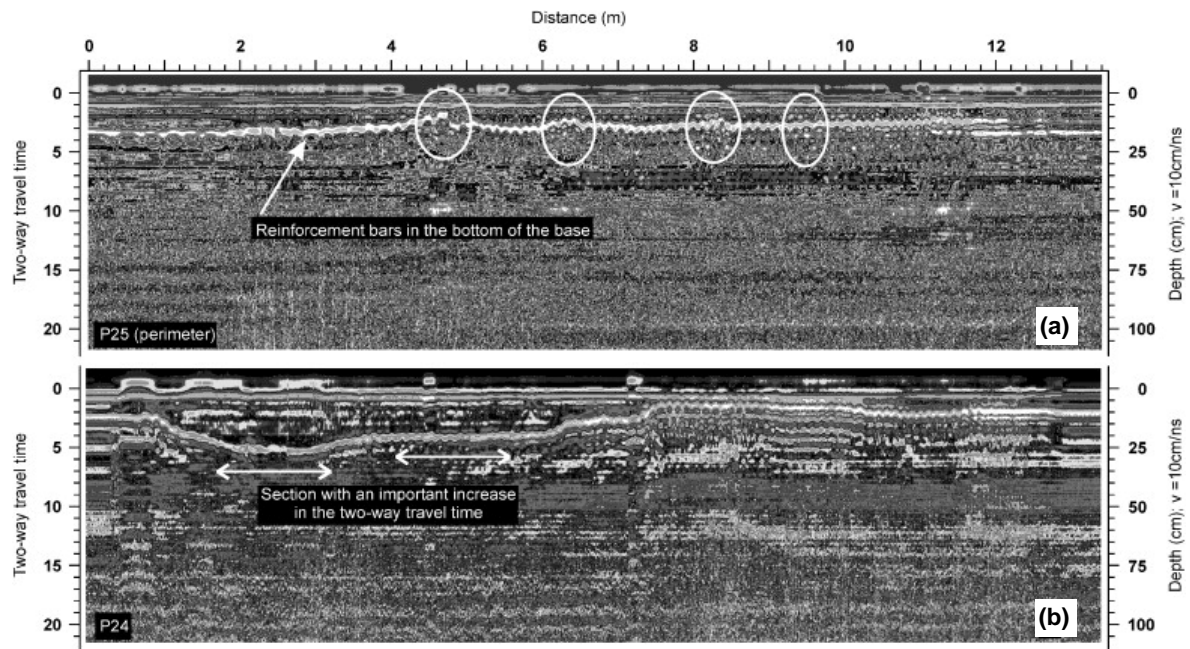


Figure 16 : Profiles showing evidence of (a) cracks and (b) humid zones (Pérez-Gracia et al. 2008a)

On every profile, the reinforcement bars situated at the bottom of the slabs are clearly visible. A fault or a crack appears then as a local change of the time associated to the rebars (indicated with white circles on profile P25 (Figure 16 (a))), while the humidity causes a decrease of the concrete speed and thus increases the two-way travel time. This is clearly visible on the scan P24 (Figure 16 (b)).

With those radar results, it was possible to create maps of the cracks (indicated by black points on Figure 17 (a)). If some of the detected cracks correspond to visible fissures on the surface (reported as grey lines), a majority of them weren't visible. A map of the humid zones was also drawn (Figure 17 (b)), and the presence of a shallow water table, probably responsible for the humidity problems, was also revealed.

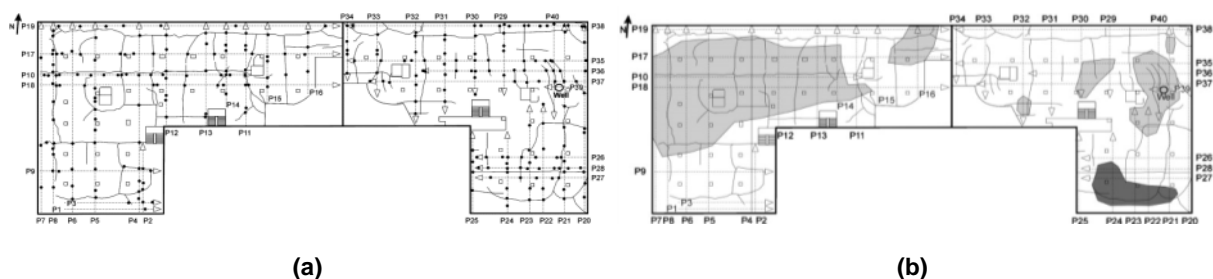


Figure 17 : Maps of (a) points with evidence of cracks (b) humid zones (Pérez-Gracia et al. 2008a)

In addition, this GPR inspection of the slabs permitted to detect variations in the slab thickness. To distinguish them from the wet zones, the authors used the different frequency content of the radargrams.

2.7.2 Signal analysis and statistical methods

The actual prospects with radar concern the development of automatic inversion methods to correlate the parameters obtained from measurement to the structure characteristics. Two possibilities are considered: the inversion of the physical model of wave propagation and the inversion with statistical models. The advantage of this last possibility is that the problems can be solved without taking into account the physical background, whose complexity doesn't matter anymore. (Bungey 2004; Balayssac et al. 2007).

The statistical models can involve artificial neural networks (ANN). This method is a mathematical (or computational) model based on biological neural networks. In short, during a learning phase, the model is submitted to a set of data (which can be extracted from GPR profiles) and adapts itself to fit its outputs to the real features of the tested structures. Then, the model can be used on other data sets, first to check its validity and then to analyze unknown structures. (Viriyametanont 2008)

This solution was recently developed by K. Viriyametanont (Viriyametanont 2008) for the determination of the water content and the porosity of concrete samples, as well as the depth and diameter of the rebars. The predicted values of all the parameters by the neural network were well correlated with the real characteristics of the tested samples, except for the determination of the rebars diameters. However, this parameter can be estimated by the mean of the results obtained with a sufficient number of measurements. Finally, the validity of the models was proved on test samples and real structures.

3 *Impact-Echo*

Impact-echo is a method based on sound, or stress, waves propagation. Those waves are generated by a steel sphere impact at the surface of the concrete and have a frequency inferior to 80 kHz. In the concrete, waves reflect on interfaces between materials of different acoustic properties. Those interfaces are typically situated between concrete and air, concrete and water or concrete and steel. The acoustic properties difference between two different concretes is generally too slight to be detected, thus the main applications are to detect voids and cracks or steel rebars inside concrete. Wavelengths typically range from 5 cm to 2 m, which is sufficient to avoid detection of the natural heterogeneities of concrete (Sansalone and Street 1997).

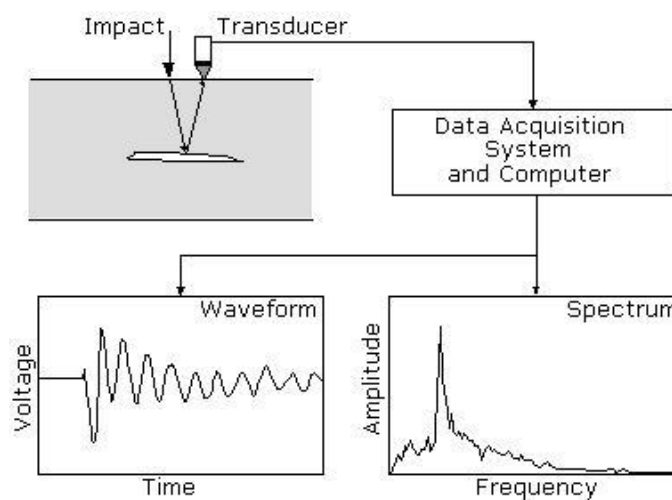


Figure 18 : Impact-Echo principle (Sansalone and Street 1998)

Part 2: Experimental program

4 Instrumentation

Typical instrumentation for GPR is composed of an antenna unit, a control unit, a display device and a storage device. Those two last parts can be replaced by a laptop equipped with an acquisition program, which enables the user to display data during acquisition, to apply directly some filters enhancing data visualization and to save radargrams on the hard disk. The antenna and control unit are manufactured by the company Malå Geoscience.

The antennas are chosen with the highest possible frequency (2.3 GHz) in order to maximize the resolution. With those antennas, connected to the control unit with coaxial cables, radial resolution is approximately equal to 1.3 cm and maximum penetration depth equal to 40 cm (according to the manufacturer). Each antenna is composed of an emitter and a receiver, both contained in a small shielded box which encloses the antenna to minimize coupling with signals in the air. Both transmitter and receiver are situated on the longitudinal axis of the antenna, at a distance of 2 cm from the lateral axis, marked on the sides of the antennas. Therefore, the distance between the two antennas is constantly equal to 4 cm.

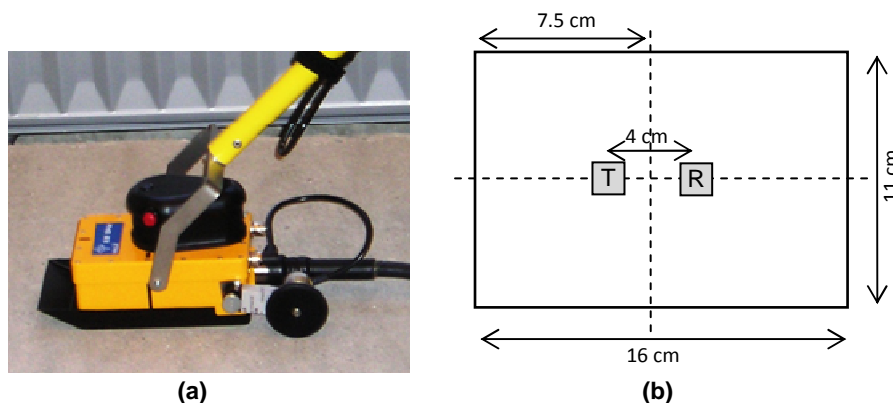


Figure 19 : HF antenna used for investigations

To perform tests with variable gaps, like CMPs (see § 2.4.2), we need to have the possibility to separate the emitter and the receiver. If it is not possible, two different antennas are necessary to perform the test, which can be carried out by deactivating the emitter of one of the antennas. Each antenna is equipped with a measuring wheel, transmitting electrical pulses to the control unit. This enables to know the exact point on the profile corresponding to each registered signal.

The control unit monitors the repetition frequency of the pulse, provides power to the antennas, acquires and amplifies the received signals and transmits them to the display device. It can be equipped with two HF (High Frequency) modules to support two antennas simultaneously. This makes it possible to use different modes of acquisition: direct, CMP or WARR. It is connected to the display device (here the laptop) with an Ethernet cable.

5 Samples

Impact-echo and radar signals were experimentally obtained on 12 slabs, in which various defects had been introduced. The concrete substrate slabs are 800 x 600 x 80 mm³. These quite important dimensions have been chosen in order to limit edge effects. After 28 days, the slabs surfaces were prepared by sandblasting, before to be covered with PCC (Polymer Cement Concrete). The repair layer was 5 and 8 cm thick, respectively. At the interface, various defects have been introduced to simulate the presence of delaminations.

5.1 Concrete substrate slabs production

After component mixing, 12 concrete substrate slabs were cast. They were designed in order to obtain a concrete compressive class of C 20/25. The composition is given in Table 3. This low grade concrete was selected because of the usually low quality of concrete structures to be repaired.

	C 20/25 (kg/m ³)
CEM I 52.5 N	225
Sand 0/2	792
Crushed limestone aggregate 2/8	297
Crushed limestone aggregate 7/14	535
Crushed limestone aggregate 14/20	356
Water	200
W/C	0.89

Table 3: Concrete slabs compositions

After moulding, the slabs were vibrated during 30 seconds on a vibrating table. The concrete slabs were demoulded after 24h curing and then conserved in a climatic room for 27 days. The compressive strength of concrete was checked for each mix on 150 mm cubes after 28 days, showing a mean compressive strength of 29.6 MPa. Complete results are given in Appendix 1 and tend to confirm the belonging of the substrate concrete to the C20/25 compressive class.

Each slab was referred with three numbers. The first one corresponds to the experimental campaign, and is always equal to 1. The second one represents the day of moulding of the slabs. They were realized within 3 days so it can be equal to 1, 2 or 3. Finally, the last number was given arbitrarily to the four slabs realized a same day, in order to differentiate them.

5.2 Surface preparation

After 28 days of curing, slabs surfaces were prepared with wet sandblasting (Figure 20). Surface preparation was performed on the moulded face, in order to have a relatively plane interface after repair.



Figure 20 : Concrete slabs sandblasting operations

Wet sandblasting is accomplished by injecting abrasive - in our case sieved sand - into a pressurized water stream. Wet sandblasting was selected as surface preparation because it doesn't introduce too much superficial microcracks in the substrate concrete, while ensuring a good bond strength after repair (Courard and Schwall 2006).

5.3 Interface roughness evaluation

After sandblasting, roughness of the concrete surfaces was evaluated with both sand patch test and optic equipment (ATOS).

5.3.1 Sand patch test

Sand patch test is an easy method to determine texture depth of a surface. It is described by the European norms EN 1766, "Products and systems for the protection and repair of concrete structures. Test methods. Reference concretes for testing". It is used to determine the average depth of pavement surface or concrete macrotexture. To perform this test, next equipment is needed:

- soft brush;
- wooden disk;
- calibrated cylinder of known volume V ;
- graduated rule;
- fine sieved sand.

The principle of the test is to fill the cylinder with sand, whose granulometric curve is given in Appendix 2, so that the sand volume is exactly equal to the cylinder busload. This known volume of sand is then poured onto the surface of the slab and spread with the wooden disk in a circular area (Figure 21).



Figure 21 : Sand patch test

The sand penetrates the surface asperities and there is a maximum diameter from which it is not possible to spread the sand disk anymore. The mean diameter D of the patch is then measured, by taking the mean between the maximum diameter and the diameter perpendicular to it. The sand patch test results (spt) corresponding to mean depth of the macro-texture is then given by the equation (41).

$$spt = \frac{4V}{\pi D^2} \quad (41)$$

Results are summarized in Table 4:

Slab n°	d1 (cm)	d2 (cm)	Spt (mm)
1.1.1	41	37	0.21
1.1.2	44	35	0.20
1.1.3	42	33	0.23
1.1.4	41	38.5	0.20
1.2.1	42	38	0.20
1.2.2	39.5	36.5	0.22
1.2.3	41	34	0.22
1.2.4	44	37	0.19
1.3.1	41	33.5	0.23
1.3.2	41.5	36	0.21
1.3.3	39	38	0.21
1.3.4	39.5	37	0.21

Table 4 : Sand patch test results

We can observe that the dispersion of the results is quite low, which ensures that the surface roughness could be considered as uniform for all the slabs. In the European norm EN 1766, three different texture classes are defined (UBAtc 2002):

- smooth : $spt < 0,2 \text{ mm}$;
- sandblasted : $0.2 \text{ mm} < spt < 0,5 \text{ mm}$;
- rough : $spt > 0,5 \text{ mm}$.

Most of our results are situated at the limit between the sandblasted and the smooth classes. Those results are consistent, because we applied a relatively smooth sandblasting.

5.3.2 ATOS optical evaluation

The interfaces were then qualified with ATOS equipment. ATOS is an optical measuring device based on the principle of triangulation and Moiré technique. A central projector lights the target with a fringes network observed by two calibrated cameras. For each pixel, ATOS provides the 3D coordinates with a high precision. The result of the measurement is a polygonal mesh of the object's surface. ATOS is generally used for mechanical applications, such as the digitalization of mechanic parts in CAD programs.

Here the goal is to obtain a 3D representation of the surface to have the possibility to evaluate its roughness and calibrate specific parameters such as mean roughness, highest peaks and holes... In order to get the highest resolution possible with the device, we analyzed a relatively small zone ($125 \times 100 \text{ mm}^2$). Six little black circular stickers were pasted on the zone as reference points for the equipment (Figure 22). Then, the measurements have to be repeated with six different axes to get the 3D coordinates of the points. The resolution of the ATOS device for these measurements is evaluated to 0.12 mm .

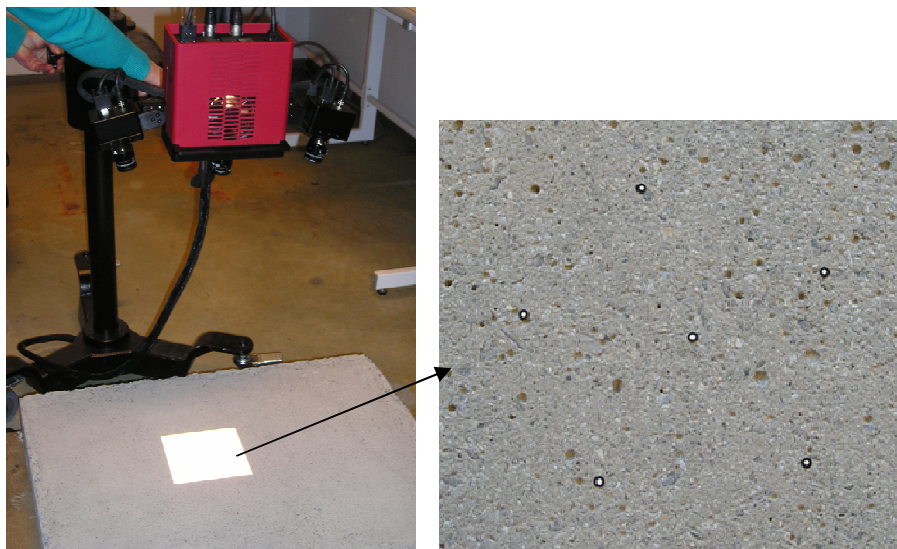


Figure 22 : ATOS measurement

As results, ATOS gives a cloud of points belonging to the surface. The surface described by those points is oblique and delimited by an irregular, circle-like form. To make the analysis

easier, we cut the surface into a rectangular shape of dimensions 8 x 8 cm² and then rotated it around the x and y axes, to obtain a horizontal surface (Figure 23). The matrix was also adjusted to get a fixed spatial interval (equal to 0.3 mm), by calculation of the mean of the points situated in a circle of 0.2 mm radius from each point of the grid. This transformation permits a potential future interpretation of the surface characteristics with the program RugoDS (Schwall 2005), which only accepts rectangular horizontal surfaces.

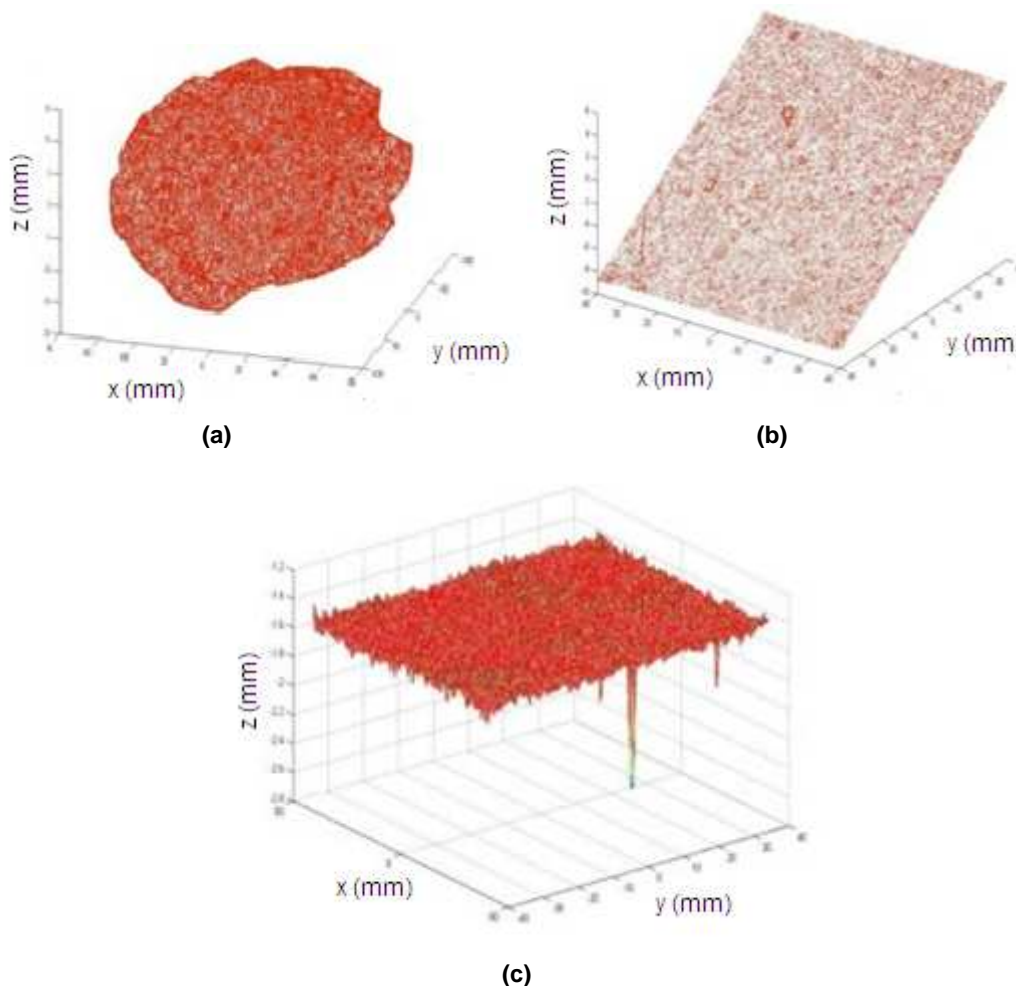


Figure 23 : Surface transformations to adapt ATOS outputs into RugoDS inputs
(a) Initial data (b) Surface after cutting (c) Surface after rotation

To compare the ATOS results to the sand patch test results, we tried to estimate the half-depth of the points. Unfortunately, the results obtained with the program RugoDS can't be directly linked to the sand patch test results, so we wrote our own Matlab code to make the comparison. The mean Z-value of the matrix is of course easy to calculate. The difficulty is to know to which reference we can compare this mean depth to evaluate the half depth. The sand is filling the different holes and bubbles of the surface, but doesn't reach the highest peaks, corresponding to the aggregates that were not eroded by sandblasting. From the total profile, it is usually needed to filter it to obtain waviness and roughness profiles. In our case it is not necessary because the tested surfaces are very smooth and small.

The standard deviation σ is a non arbitrary parameter permitting to evaluate a regular distance from the mean without taking into account the furthest points. In a normal

distribution, removing the positive points exceeding standard deviation is equivalent to keep about 84 % of the points. For two standard deviations, this amounts to 97.5 %. On Figure 24, one can observe the reference surfaces for slab 1.2.2 situated at the levels (mean + σ) and (mean + 2 σ).

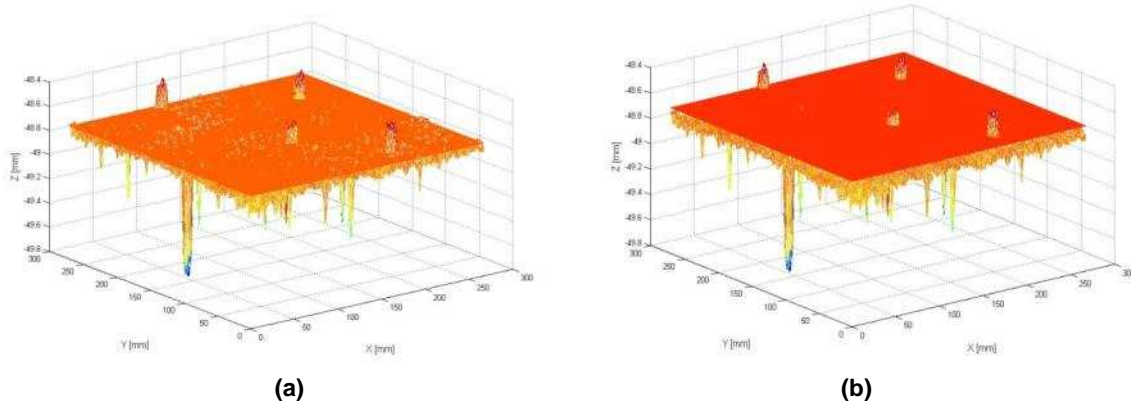


Figure 24: Reference surfaces equal to (a) mean+ σ (b) mean+ 2 σ

On Figure 24 (a), we observe that the big aggregates are visible, as well as numerous little peaks. When the limit is fixed to two standard deviations (Figure 24 (b)), only the main peaks are visible, but the surface seems however to lie quite high with regard to the level of the sand during sand patch test. Intuitively, we assume that the limit level of the sand during sand patch test should be comprised between those two reference surfaces. A simple way to check and refine this hypothesis would be to make an ATOS measurement of the surface during the sand patch test.

Once this reference surface is obtained, the half depth can be simply calculated from the mean difference of Z-values between the reference and each point situated below it. For the peaks situated above the surface, the depth is set equal to 0. Results are detailed in Table 5 for the intervals of 1 and 2 standard deviations:

Slab n°	Spt (mm)	1 σ	2 σ
1.1.1	0.21	0.054	0.103
1.1.2	0.20	0.055	0.107
1.1.3	0.23	0.070	0.135
1.1.4	0.20	0.059	0.114
1.2.1	0.20	0.069	0.131
1.2.2	0.22	0.047	0.092
1.2.3	0.22	0.037	0.071
1.2.4	0.19	0.057	0.112
1.3.1	0.23	0.063	0.124
1.3.2	0.21	0.04	0.076
1.3.3	0.21	0.054	0.103
1.3.4	0.21	0.113	0.225
mean	0.211	0.060	0.116

Table 5 : Comparison of sand patch test and ATOS results

Except for slab 1.3.4, the results obtained from ATOS data are totally different from the sand patch test results. This can be explained by several factors:

- we are out of range of validity for both sand patch test and ATOS equipment;
- the method of results adjustment and, especially, the calculation of a mean of the nearest points could have an influence on the results;
- the surface tested with ATOS was very small and may be not representative of the total slab surface.

In conclusion, the results are not satisfying, but the method should be tested on really rough surface before to be totally rejected. An ATOS test during sand patch test would also give interesting information.

Another method was tested to extract the same information from the ATOS profiles, using the Abbott curves created by RugoDS (Schwall 2005). It turned out to give similar results than the method previously explained, with a more complicated method involving some approximations. For these reasons, this second method wasn't hold back.

As for all the Matlab codes written in the framework of this thesis, an informatics version of the described function is available by request to me or my advisors in a computer version.

5.4 Concrete substrate slabs characterization with GPR

Before repair, all the slabs were carefully analyzed and tested with both radar and impact-echo. The slab thicknesses are displayed in Appendix 3. For radar tests, only one antenna was available, so that evaluation of profiles was the only possible acquisition mode. All the profiles were realized in the length direction, joining the two mid-widths of the slab. The profile acquisition procedure will be described in § 6.2.

To study the resulting radargrams, we decided to export the data to Matlab, in which a treatment code can be written and applied to every sample. When a radargram is registered with Groundvision2, two main files are created: the first one has a .rad extension and contains all the data relative to the measurement like frequency, number of samples, type of antenna, time window, number of traces, etc. The second file has a .rd3 extension and contains the profile itself.

To export those data to Matlab, the program loadrd3 (Barret 2004) was used. Its principle is to get the number of samples and traces into the file.rad and to transform the .rd3 file into a matrix of dimensions *traces* \times *samples*.

The obtained matrix can then be drawn as a surface. To see the details of the radargram, the color scale can also be modified, limiting the variations into a shorter interval of intermediate values. In Figure 25 (a), we can observe a resulting radargram, obtained on the slab 1.2.4. The amplitude of the wave is given as a function of the time and distance samples numbers.

The axes can be adapted to correspond to the real distance and time scales. This can be done using the real time and length windows as well as the sampling intervals. This information is available in the .rad files. The time of the direct air wave arrival has to be set equal to zero. It can be manually calculated but an automatic detection is easily implemented into the code, because this wave has the strongest amplitude of the whole radargram. The zero time corresponds to the maximum of the mean trace, from which we subtract the time of direct wave in the air arrival. An initial distance, depending on the size and position of the antenna, can also be added to make the radargram distance scale matching the position on the real slab. This has to be manually implemented but is not much variable from one slab to another since the measurements have been conducted with a similar procedure. In order to focus on the interesting part of the graph, the time scale is limited from -1 ns to 6 ns. The result is shown in Figure 25 (b).

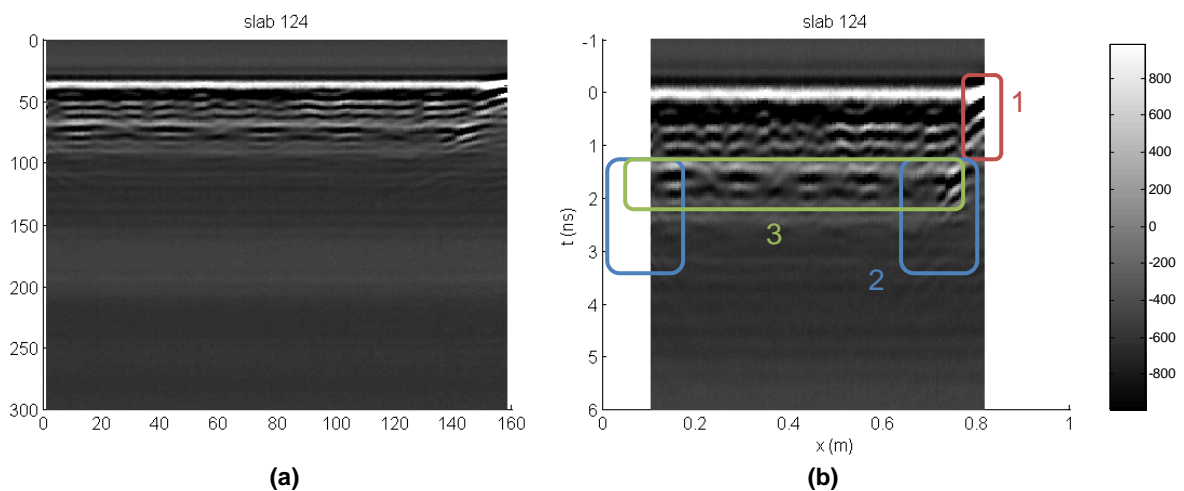


Figure 25 : Visualization of radargrams in Matlab7 before (a) and after (b) axes adaptation

From this representation of the substrate slab, we can make several observations:

- [1] we can clearly observe the direct wave in the air at the end of the slab, while it isn't possible on the first traces. This is due to antenna geometry (a longer distance is needed at the beginning of the slab because of the presence of the wheel) and explains the necessity of an initial offset x_{init} ;
- [2] at the beginning and at the end of the slab, we can observe hyperbolas, created by the diffraction of the waves on the edges, which act as punctual defects. The hyperbola peak position reflects the position of the edge, while its shape depends on the speed of the waves into the concrete;
- [3] the bottom of the slabs is represented by a dotted line. This is due to the presence of a wooden pallet under the slab. The difference in dielectric constants is lower between wood and concrete than between air and concrete. Thus, the wooden planks are observable on the radargram, the stronger reflections corresponding to the concrete/air interfaces.

The depth of the reflections from the bottom surface depends on the thickness of the slab and the speed of the waves into the concrete. The thickness of the slab can be measured, so that the speed of the waves into the concrete can be determined using the time of reflection from the bottom and the shape of the hyperbolas situated at the edges of the slabs. Matlab can be used to compare the theoretical results with the real radargram and deduce the speed of the waves. This is represented in Figure 26 (a).

As for the time zero, the time of reflection from the bottom can be automatically detected as the maximum of the mean trace in the interval corresponding to the range of possible reflection times. As seen in the paragraph 2.3, the reflection coefficient for a concrete/air interface is equal to about 0.5, so the searched peak should be positive as the zero-time peak. Then, the wavespeed v corresponding to the measured thickness h can be easily calculated:

$$v = \frac{2}{t} \cdot \sqrt{h^2 + 0.02^2} \quad (42)$$

where 0.02 is the half-distance between the emitter and the receiver. The radargram can then be displayed in function of the reflection depth (Figure 26 (b)).

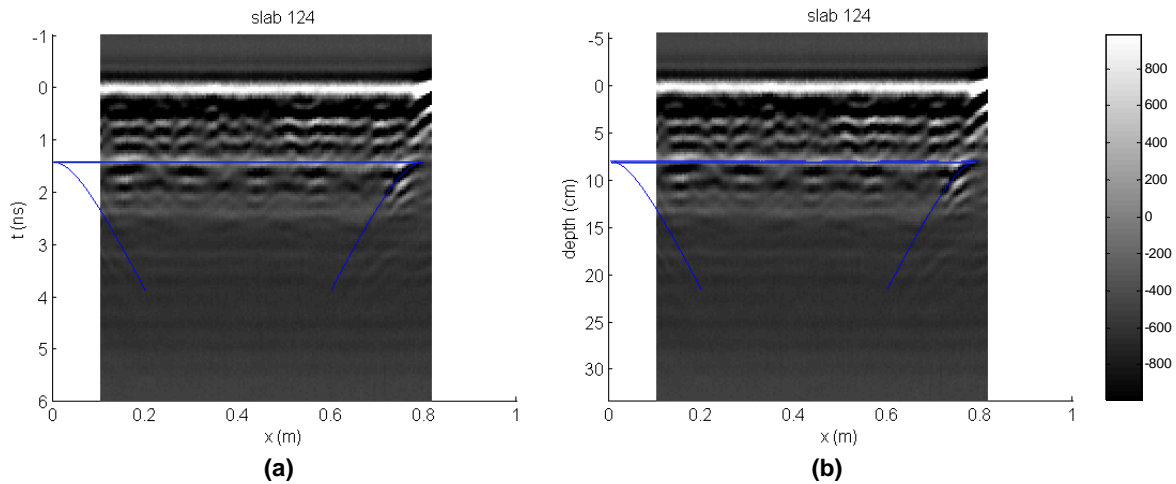


Figure 26 : Slab 1.2.4 radargram (a) with time (b) with depth axis

The results obtained on all the slabs are given in Appendix 4. The values of wavespeed determined by this method range from 0.103 to 0.114 cm/ns, with a mean situated at 0.109 cm/ns. All those values are situated in the range of variations of speed into concrete described in the literature (Soutsos et al. 2001). The results don't seem to be affected by the slab age or the slab thickness. The precision of the thickness measurement was limited to a few millimeters, mainly because of the thickness variation between the middle and the edges of the slab. There is consequently no reason to consider these little variations of speed in the further developments: only the mean speed will be kept.

5.5 Description of defects

Before repairing the slabs, defects were introduced at the interface. Different situations were induced:

1. no defect (reference);
2. expanded polystyrene (EPS) panel, 40 cm width and 0.5 cm thick;
3. expanded polystyrene (EPS) panel, 10 cm width and 0.5 cm thick;
4. homogeneous plastic sheet (Mylar), 40 x 20 cm²;
5. local trapezoidal plastic sheet, length of 25 cm, width varying from 5 to 10 cm;
6. demoulding oil (34 x 54 cm²).

Each defect was introduced on two different slabs, to be covered with the two different repair thicknesses. A table associating the slabs numbers with the defects and repair thicknesses is available in Appendix 3.

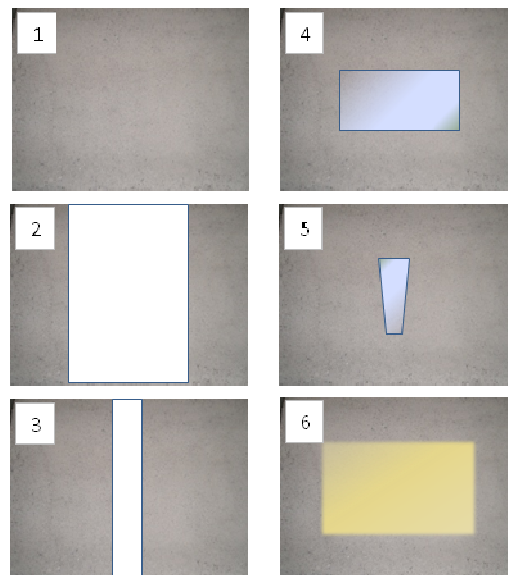


Figure 27 : Description of defects at the interface between concrete slabs and repair material

For defects 4 and 6 (homogeneous plastic sheet and demoulding oil), the goal was to create a uniform defect on the whole slab without compromising the adhesion of the repair mortar to the concrete slab. Consequently, we left a zone without defect all around the slab to ensure the adhesion between the two materials, with a higher unrepaired width for the plastic sheet which totally disrupts the adherence. For defects 2 and 3 (expanded polystyrene), the defects were disposed on the total width of the slab, to have the possibility in the future to burn the polystyrene and study a real void.

The demoulding oil is a recycled mineral oil produced by Sika Décoffre, suitable for every formwork material. Plastic sheet Mylar is the commercial name for Biaxially-Oriented PolyEthylene Terephthalate (boPET). The double orientation of the molecular chains of this polymer is obtained by a second drawing in the orthogonal direction of the extruded film

before crystallization. This gives to the material high strength and stiffness. The Mylar sheets used in this study had a thickness of 100 μm .

A couple of minutes before the repair mortar application, the surfaces of the slabs were coated with primer. In the case of the plastic sheets and the expanded polystyrene, primer was spread on the defect. In the case of the oil defect, oil was spread instead of primer. The first and second layers of primer were spread about 30 and 10 minutes before the repair. This time was sufficient for the primer to lose its opacity before every following application.

5.6 Repair operations

For the repair mortar placement, we used simple wooden framework moulds. Each one was maintained by two clamps, while the watertightness was provided by a silicone joint. The whole system is displayed in Figure 28 in the case of the polystyrene defects. All the slabs were repaired with the same commercial repair mortar. To have a perfectly smooth surface which makes easier both radar and impact-echo testing, we chose to use a self compacting mortar.



Figure 28 : Slabs repair preparation (EPS defects)

The repair material was Cemtop 320. This commercially available PCC (Polymer Cement Concrete) is a pumpable cementitious mixture formulated from High Alumina Cement, aggregates, supplementary binders and chemical admixtures. It is delivered as a pre-blended dry powder to which water should be mixed. The product has a very low stiffening time (final heavy loading can be applied after only one week) and a very low shrinkage ($<0.005\%$), which is a very important property for repair material (cf. § 1.4). The compressive strength is equal to 32 N/mm^2 (Cemart 2009).

The compressive strength was checked on $40 \times 40 \times 40 \text{ mm}^3$ cubes after 12 and 50 days. The mean strengths were estimated at those dates at 22.6 MPa and 29.9 MPa, which is slightly inferior to the product specifications. The detailed results of the tests and the product sheet are given in Appendix 5.

6 Investigation procedure

To get as much information as possible from the samples, we decided to use both profile recordings and CMP acquisition. Profile recording is the easiest and most common method to detect defects and create maps of the underground, while CMP gives information about the thickness and the wave speed for only one point.

6.1 CMP

As represented in Figure 10, CMP (Common Mid Point) is an acquisition mode consisting in increasing the distance between the transmitter antenna and the receiver, with a constant reflection point, corresponding to the middle point between the two antennas. In our case, both antennas consist in a transmitter and a receiver enclosed in a box. Thus, to perform CMP, the transmitter of one of the antennas has to be turned off.

An ideal CMP measurement begins with the two antennas very close to the middle point. In our case, it is not possible to make such measurement, because the antennas are not punctual: they indeed measure $160 \times 90 \times 110 \text{ mm}^3$ and are equipped with wheels, cables and plastic skid plates. The minimum distance between the two face-to-face antennas is about 4 cm. Consequently, if we take into account the position of the antennas into the shielded box, the total distance between the antennas is about 19 cm. The first acquisition possibility is thus to make a classical CMP (Figure 29 (a)), giving up the idea of having the zero distance point on the radargram and therefore the crest of hyperbolas.

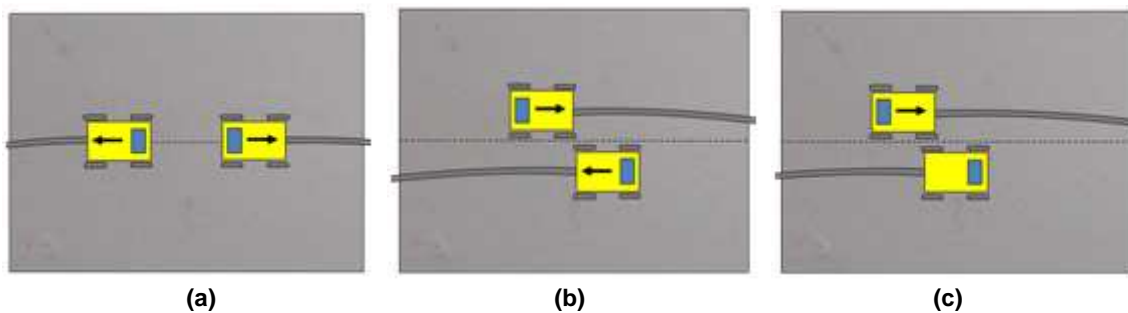


Figure 29 : (a) Normal CMP ; (b) Double CMP ; (c) WARR

Another possibility is to make a double CMP (Figure 29 (b)): the antennas start at the opposite edges of the slab, cross in the middle, which is then the point of minimum distance, and continue till the opposite edge of the slab. For both normal and double CMPs, the operators should be careful to move the two antennas at the same speed, in order to keep the same midpoint.

A third possibility is to realize a WARR (Wide Angle Reflection and Refraction) acquisition (Figure 29 (c)), in which the receiver antenna is immobile at the middle of the slab and only the mobile antenna is moving. WARR is not strictly speaking a CMP acquisition, because the

middle point between the two antennas, and so the reflection point, is not fixed during acquisition. Nevertheless, this acquisition mode is interesting because only one antenna has to be moved, thus the speed has no importance and the acquisition is very quick and easy. The advantages and disadvantages of those three methods are summarized in Table 6.

	Normal CMP	Double CMP	WARR
Alignment	Yes ⇒ Stronger transmission of direct waves	No ⇒ Weaker transmission of direct waves	No ⇒ Weaker transmission of direct waves
Zero offset visibility	No	Yes	Yes
Reflection point	Fixed	Fixed	Variable
Acquisition speed	Low	Low	Fast

Table 6 : Advantages and disadvantages of different CMP acquisition methods

The main advantage of WARR by comparison to the two other methods is the easiness of acquisition. But the variation of reflection point can complicate the results, especially if the reflection zone is not uniform, which is the case for our smallest defects. Thus, we will only use the two first methods and compare the results.

The receiver of the emitting antenna doesn't have to be turned off during the acquisition. If it is turned on, it will record a simple profile during the CMP acquisition. This radargram can bring information about the depth and visibility of the interface and on the speed of the waves. This is especially the case for double CMPs, in which both antennas are moved along the total slab. To study the speed of the waves into the material, we will thus finally combine and compare three radargrams:

- normal CMP;
- double CMP;
- the profile registered by the emitting antenna during the double CMP.

6.2 Profile scanning

The second acquisition mode is the profile scanning, allowing representing the characteristics of the structure situated under the auscultation line. This method was already used in §5.4 for substrate slabs characterization. To represent the whole tridimensional structure, a set of profiles have to be recorded at the surface of the slabs. The distance between two measurements has to be short enough to get a good resolution for the defects representation. However, 12 slabs must be scanned so the number of profiles on each slab should be limited. In this situation, a 5 cm offset between two measurements seems to be a good compromise (Figure 30).

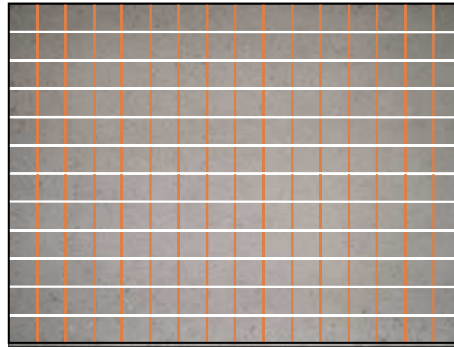


Figure 30 : Profile acquisition grid

With this method, we decided to record 11 longitudinal profiles and 15 lateral profiles per slab. To facilitate the profile acquisition, we drew a 5*5 cm² grid on every slab.

6.3 Acquisition parameters

For both CMP and profiles recording, we chose the same parameters in the acquisition program Groundvision2:

- according to the operating manual of the program, we have to select a *sampling frequency* approximately equal to 10 times the antenna frequency. The antenna frequency is equal to 2.3 GHz, and so the sampling frequency is set equal to 23 GHz;
- the *number of samples* (cf §2.4) shouldn't be chosen superior to 500 because for higher values the acquisition speed decreases. In our case, a number of 300 was selected because the thickness of the studied structure is low and all the interesting information is mainly comprised into the 150 first samples (see for example Figure 25 (a));
- the *trig interval* is the distance between the registering of two different traces. In our case, the length of the structure is limited so that the trig interval was set equal to 0.5 cm. Anyway, the real trig interval is not exactly equal to this value. Indeed, we can observe in the rad files that the real distance interval is equal to 0.4532 cm;
- finally, the *number of stacks* of every signal was set equal to 8, in order to decrease the importance of the noise, as explained in § 2.4.

Part 3: Results

7 *CMP signals*

As explained in the previous chapters, the goal of CMP measurements is to study the speed of waves and depth of interfaces in one point of the structure, situated at the same distance of both antennas during all the acquisition time. As explained in paragraph 6.1, three signals were registered on each slab:

- normal CMP;
- double CMP;
- profile corresponding to the signal registered by the emitter antenna during double CMP acquisition.

To be sure we have at least one correct signal for each slab, each measurement was repeated again.

7.1 Analysis procedure

To analyze those results, a specific code was written in Matlab, in which all the profiles were loaded with the program LoadRd3 (Barret 2004). For each slab, the best simple and double CMP profiles were selected. They were registered in a specific Workspace, as well as their traces number and the measured thickness of the slabs.

The global analysis principle is the following one. The user first estimates the speed of both materials. The theoretical waves corresponding to those speeds and to the actual slab thickness are then drawn. By comparing those curves to the real radargram, the user can adjust the speed of the two materials. The presence and amplitude of reflections at interface depends on the type of defect placed at the interface.

7.1.1 Normal CMP

The time interval dt is equal to the total time divided by the number of samples. Those parameters are available in the rad files, but don't change from one profile to another if the profile acquisitions parameters are kept constant. It is fixed in our case to 0.043 ns. The length interval dx is also available in the rad files and is equal to 0.4532 cm. Anyway, the measured length corresponds to the distance covered by the antenna equipped with the activated measuring wheel, while we are looking for the total distance between the antennas. In CMPs, the two antennas are moved simultaneously; the total distance interval is consequently equal to 2×0.4532 cm.

For the reflections on the interface, the equations used in this program are the theoretical CMP equations described in the paragraph 2.4.2 (equations (26) - (34)). The program draws the direct waves into air and into concrete, the first and second reflected waves on the interface and the critically refracted wave, which appears in a dotted style in the same color as the simple reflection.

For the reflections on the bottom of the slabs, the equations are almost the same as those of the interface. The two exceptions are the thickness, which corresponds now to the sum of the substrate slab and repair mortar thicknesses, and the speed of the waves, which should now take into account the speeds of the two materials, their thickness and the refraction angle at the interface. Typical waves involving one or more reflections on the bottom of the slab are represented in Figure 31.

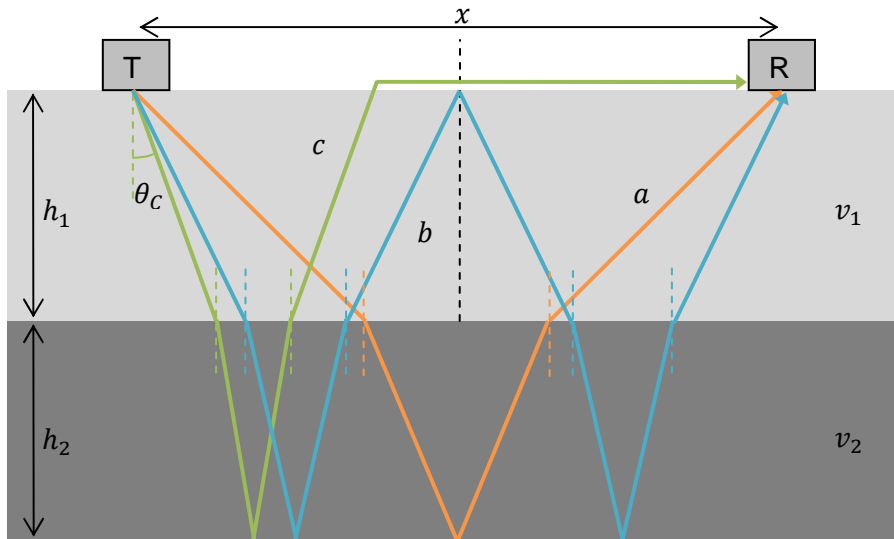


Figure 31 : Waves involving reflections on the bottom of the slab

According to the refraction laws, the inclination of a wave is modified each time it reaches an interface between two materials presenting different speeds. As seen in the paragraph 2.4.2, the angular change is governed by the equation:

$$\frac{1}{v_1} \sin \theta_1 = \frac{1}{v_2} \sin \theta_2 \quad (43)$$

In our case the difference of speed between the two materials is not very important. Indeed, both are concretes and are stored in the same atmosphere. Thus, we will make the approximation to neglect the wave deviation at the interface, and thus the mean wave speed is equal to the mean of the speeds of the two materials, weighted by their relative thicknesses:

$$v_{moy} = \frac{v_1 * h_1 + v_2 * h_2}{h_1 + h_2} \quad (44)$$

Using this mean speed and the total thickness, the equations for the waves reflected on the bottom of the slab can be written as in the case of a uniform material.

To focus on the interesting zone of the diagram, the visualization window is set from -1 ns to 10 ns. The initial offset was set equal to 19 cm, because, according to the manufacturer of the antenna (see Figure 19), the distance from the edge of the antenna to the receiver and to the emitter are 9.5 cm and 5.5 cm, respectively. The distance between the two antennas is equal to 4 cm, due to the plastic skid plate jutting out in front on the antenna. Altogether, we have thus a distance of 19 cm between the two antennas. The initial time has to be calculated manually, because the amplitude of the direct wave is not sufficient to detect it automatically. Anyway, as all the measurements have been realized with the same antenna settings, it doesn't vary from one slab to another.

7.1.2 Double CMP

In the case of the double CMP, the classical CMP equations are not valid anymore, because we have to take into account the lateral distance between the antennas. The emitter and receiver are situated on the longitudinal axis, at a distance of 5.5 cm from the edge of the shielded box. To this distance, we have to add the width of the antenna supports (wheel carriage of skid plate) and a security margin, aimed to avoid any contact between the antennas during the acquisition. Finally, we estimate the minimum distance between emitter and receiver to 13 cm.

To take this distance into account, we have to use Pythagoras's relationship. For example, the equations of the direct waves are the following ones:

$$t_1 = \frac{\sqrt{x^2 + e^2}}{c} \quad (45)$$

$$t_2 = \frac{\sqrt{x^2 + e^2}}{v_1} \quad (46)$$

Where e is the distance between the two longitudinal axes of the antennas, x is the longitudinal offset and v_1 is the speed of the superficial material. Let's call d the distance between the two antennas:

$$d = \sqrt{x^2 + e^2} \quad (47)$$

(48) and (49) are the equations of the waves reflecting once and twice on the interface, respectively.

$$t_3 = \frac{2}{v_1} * \sqrt{\frac{d^2}{4} + h_1^2} \quad (48)$$

$$t_4 = \frac{4}{v_1} * \sqrt{\frac{d^2}{16} + h_1^2} \quad (49)$$

For the calculation of the curves corresponding to a reflection on the bottom of the slab, we define a mean speed:

$$v_{moy} = \frac{v_1 * h_1 + v_2 * h_2}{h_1 + h_2} \quad (50)$$

We can now calculate the equations of the simple and double reflections on the bottom of the slab:

$$t_5 = \frac{2}{v_{moy}} * \sqrt{\frac{d^2}{4} + (h_1 + h_2)^2} \quad (51)$$

$$t_6 = \frac{4}{v_{moy}} * \sqrt{\frac{d^2}{16} + (h_1 + h_2)^2} \quad (52)$$

Finally, (56) and (57) are the equations of the critically refracted waves, whose reflections happen at the interface and on the bottom, respectively. We first have to define θ , the critical angle of refraction, as well as d_1 and d_2 , the oblique distances corresponding to the path from the surface to the interface or to the bottom, respectively, with an inclination θ .

$$\theta = \text{asin}\left(\frac{v_1}{c}\right) \quad (53)$$

$$d_1 = \frac{h_1}{\cos(\theta)} \quad (54)$$

$$d_2 = \frac{h_1 + h_2}{\cos(\theta)} \quad (55)$$

$$t_7 = \frac{d - 2 * h_1 * \tan(\theta)}{c} + 2 * \frac{d_1}{v_1} \quad (56)$$

$$t_8 = \frac{d - 2 * (h_1 + h_2) * \tan(\theta)}{c} + 2 * \frac{d_2}{v_{moy}} \quad (57)$$

Those critically refracted waves only appear from their separation point with the reflected waves. The abscissas corresponding to those points are the following ones:

$$x_7 = 2 * \sqrt{(h_1 * \tan(\theta))^2 - e^2} \quad (58)$$

$$x_8 = 2 * \sqrt{((h_1 + h_2) * \tan(\theta))^2 - e^2} \quad (59)$$

Concerning the initial parameters (time and distance) and the time and distance intervals, all the remarks made in the previous paragraph about normal CMP are still valid.

7.1.3 Double CMP profile

The analysis of the double CMP profiles is really easier and more straightforward than for the normal CMPs, but it doesn't always give by itself enough information to solve the problem.

For the profiles, the time zero is easy to detect automatically, because it has the highest amplitude of the whole profile. Equations (60) and (61) describe the horizontal lines corresponding to the interface and to the bottom.

$$t_1 = \frac{2}{v_1} * \sqrt{h_1^2 + 0.02^2} \quad (60)$$

$$t_2 = \frac{2}{v_{mean}} * \sqrt{(h_1 + h_2)^2 + 0.02^2} \quad (61)$$

The goal is to make those lines matching the visible reflections on the radargram. For the slabs with no visible defect at the interface, we get only one relationship for two unknowns v_1 and v_2 , which is insufficient.

7.2 Results

In order to determine the speed of the waves in both materials, we will first study the cases in which the interface is clearly visible, including the polystyrene and the large plastic sheet. Let's represent the CMP for the slab with large polystyrene defect and 5 cm repair thickness (Figure 32 (a)). We evidently distinguish the direct wave in the air, because its speed is known and equal to the speed of light 30 cm/ns. Besides, we also discern another straight line with a higher slope. This one corresponds to the direct wave in concrete and its slope, equal to the speed of the radar waves into the repair material, approximately rises up to 11 cm/ns.

But we can observe on Figure 32 (a) that this line (appearing in white on the graph) doesn't correspond to the theoretical position of the direct wave (plain green line) but is situated

above it. If we draw a line perfectly fitting the direct concrete wave of the radargram (dotted green line), it crosses the direct wave in the air at an offset superior to 10 cm, while it should cross it on the vertical axis. A simple way to perfectly fit the radargram to the theoretical waves would be to reduce the initial offset to 5 cm, as shown in Figure 32 (b), but this distance doesn't correspond to the real initial offset (equal to 19 cm as in Figure 32 (a)),

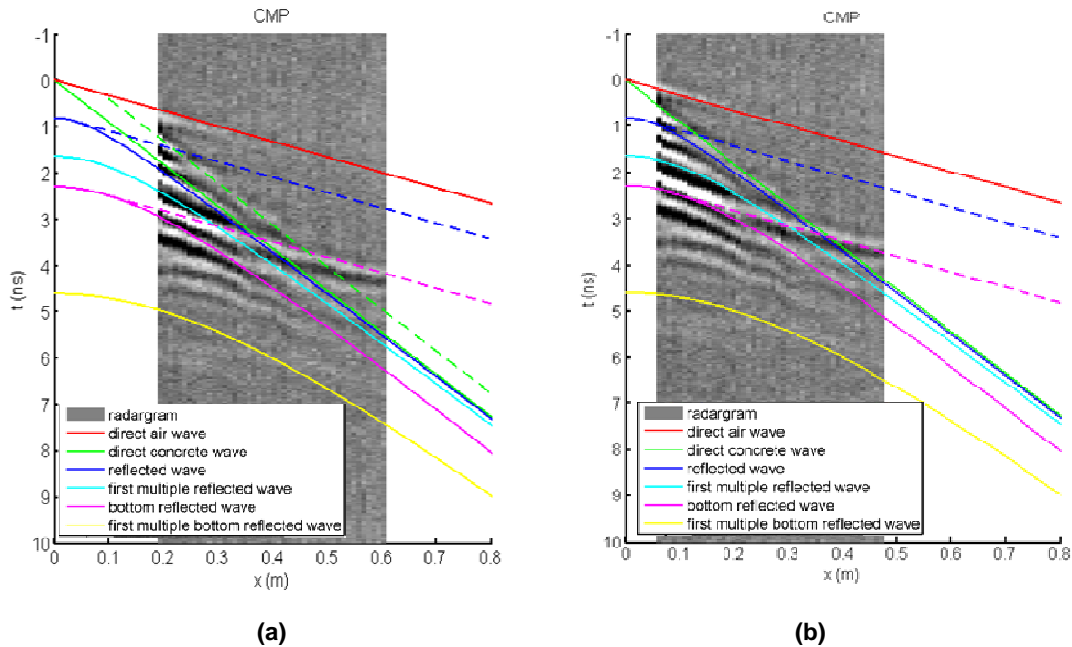


Figure 32 : CMP on slab 121, initial offset equal to (a) 19 cm (b) 5 cm

To explain the presence of this wave, we can imagine that the waves, travelling through the air inside the shielded box, are diffracted when they meet it and travel into concrete between the boxes, which are about 5 cm apart. Such a wave would travel in the air 15 cm out of the total distance and any increase of the distance between the two antennas would result in a longer path into concrete, which could explain the slope of the line. If it exists, such a wave would appear as the green dotted line visible on Figure 32 (a), which fits perfectly the radar results. Anyway, the concordance between the radargram and the theoretical waves in Figure 32 (b) is such accurate that a doubt still subsists about the real initial offset. This should be checked on the antennas or discussed further with the manufacturer.

The total CMP results, with the comparison of the three radargrams, are available in Appendix 6 for all the slabs. Anyway, we will discuss in this section some representative cases with different defects. For every sample, the speed values of 11 cm/s in the mortar and 10 cm/s in the concrete were selected. They permit to have good results in every case, even if in some cases, the speed determination could have been refined with a higher accuracy. Let's begin with the most evident defect: the large polystyrene panel with thick repair (Figure 33).

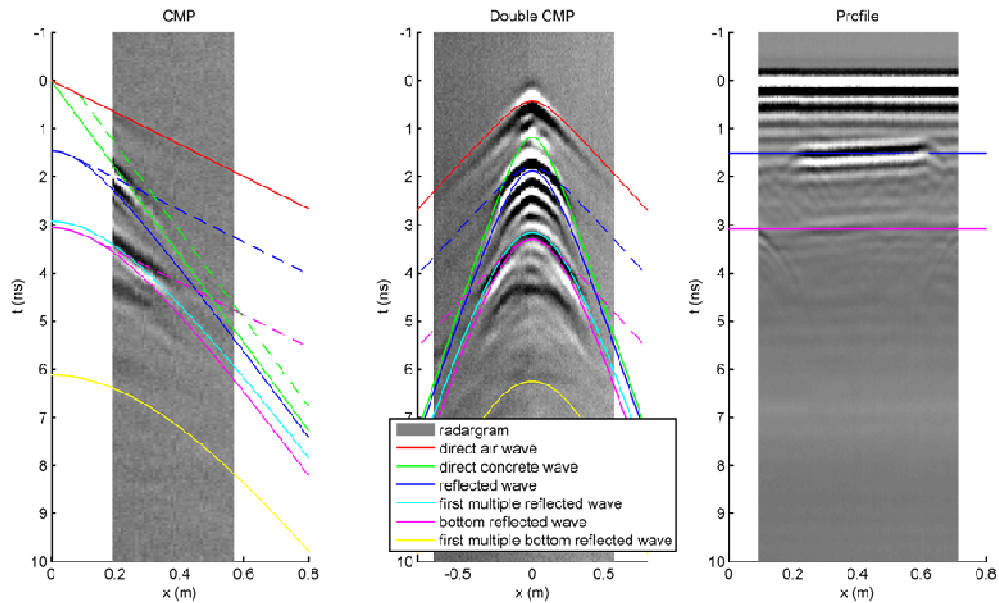


Figure 33 : CMP results - Defect 2 / 8 cm repair

We can observe a very neat reflection from the interface on the three radargrams. On the double CMP, we note the very good concordance between the shape of theoretical and real hyperbolas. On the profile, we can observe the inclination of both the interface and the bottom of the slab compared to the surface waves. This corresponds to a real thickness difference measured on the slab. As for the majority of the slabs, the double reflection on the bottom and the critically refracted wave corresponding to the interface are barely visible. The first multiple of the wave reflected on the interface is very close to the reflection from the bottom, because both the thickness and the speed are similar in the two layers. For this reason, it is not possible to say from this radargram if this wave is visible or not.

Finally, we can also observe a change in the background intensity at the middle of the double CMP radargram. This could be induced by a preferential direction of wave emission by the antenna (in the direction of the receptor situated inside the same shielded box). When the two antennas cross in the middle of the slab, the relative position of the receiving antenna regarding the emitting one abruptly changes, which could explain the global background change. The continuous variation in background that can be observed for some other slabs, however, is more mysterious. Fortunately, it doesn't impair the possibility of analysis by comparison with theoretical curves.

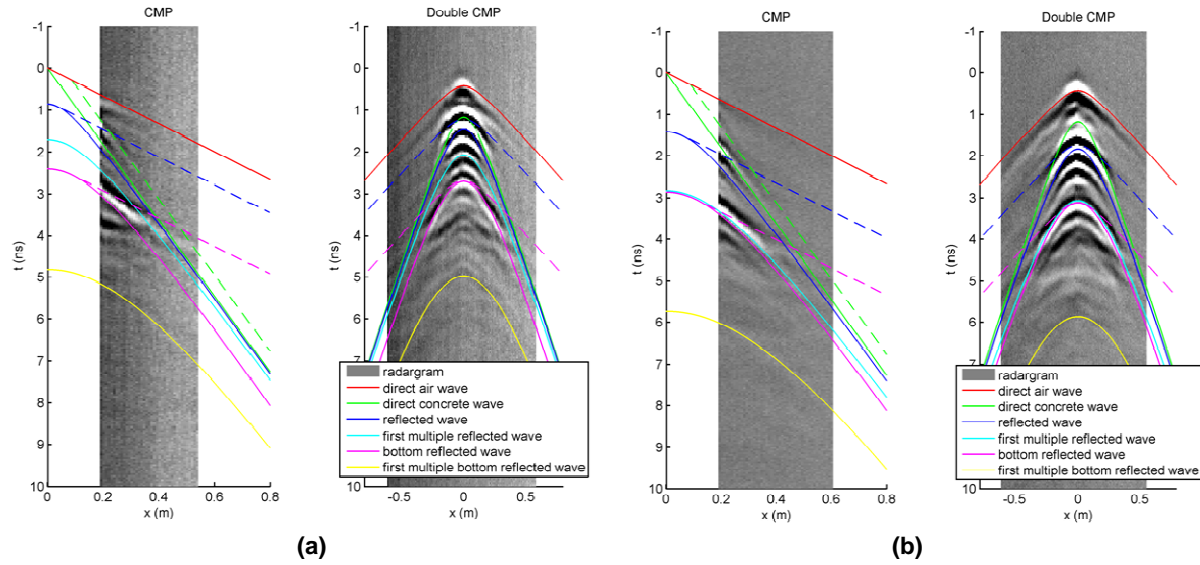


Figure 34 : CMP results - Defect 3 (a) 5 cm repair (b) 8 cm repair

Analysis of the differences between two repair thicknesses for the small polystyrene defects (Figure 34) shows that the interface is more visible in the normal CMPs for a thicker repair thickness. Nevertheless, in the double CMPs, the presence of the defect is always very clear even if we see that the distinction between interface and bottom reflections is easier with 8 cm repair. The influence of the polystyrene defect width can be evaluated by a comparison between Figure 33 and Figure 34 (b), in which the defect size is the only variable. We observe that the CMP radargrams are very similar, except for the reflection from the bottom. This confirms that the size of the defects has a small influence on CMP results, because only one point is tested. On Figure 35 the double CMPs and profiles for the large plastic sheet are displayed:

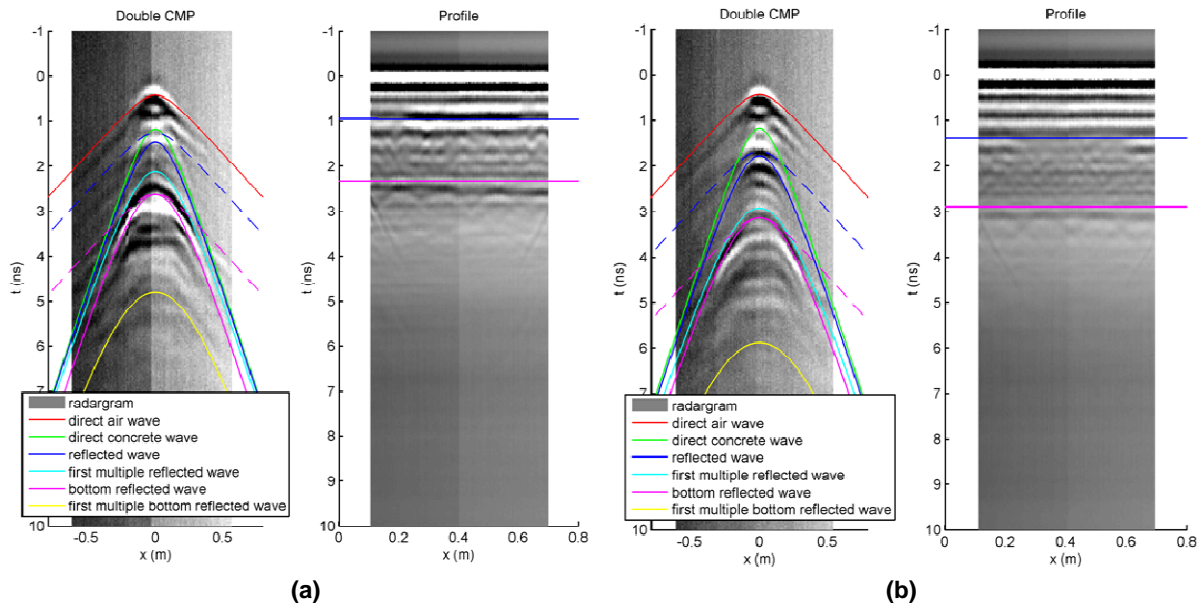


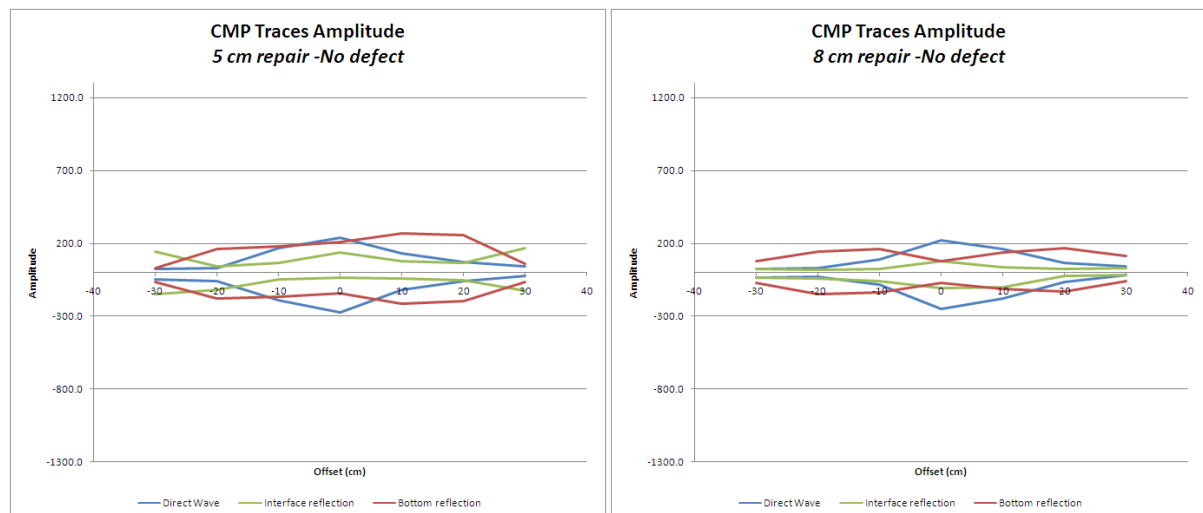
Figure 35 : CMP results - Defect 4 (a) 5 cm repair (b) 8 cm repair

Two different observations can be made from these representations. Firstly, the reflection on the plastic sheet is visible for 8 cm repair, when it is not very clear for 5 cm repair. This shows the difficulty to observe very shallow defects with radar. Then, we can observe that the defect appears differently on the profiles. For the thin repair, it appears as strong reflections, while for the thicker one, it only appears as a grey cloud. In fact it is due to the superposition of the reflected waves with the direct waves. In the first case the positive peaks are coincident, while in the second case, every peak is superimposed with an opposite peak, which result in a suppression of any peak in the reflection zone. This shows the importance to remove a mean wave corresponding to a part of the structure without defect (here the first and the last traces) to get the same defects visualization in every case. This method will be applied on the profiles for 3D representation in § 8.1

7.3 Analysis of the reflection amplitude

The last part of the CMP analysis concerns the evolution of the different wave amplitudes versus the offset. This determination was based on the double CMP radargrams. The evolution of three different waves was studied: the direct wave in the air, the wave reflected on the bottom and the wave reflected on the interface. The direct wave into concrete wasn't studied because its amplitude is too small and it is too close to the waves reflected on the interface.

Firstly, the mean value was removed from each radargram, in order to center the amplitude values round zero for every sample. The amplitude of the waves was calculated for seven different offsets; from -30 cm to 30 cm. For each offset, the theoretical position of the wave on the radargram was calculated, using the equations described in paragraph 7.1.2. Around this (x,t) point, a window of data was extracted, allowing a few pixels variation for the peak detection. Then, the maximum and minimum values were calculated in this zone. They are supposed to correspond to the maximum and minimum peaks of the concerned wave. On Figure 36, the results are displayed, for all defects materials and both repair thicknesses. For plastic sheet and polystyrene, only the big defects were tested, in order to avoid any diffraction on the edges of the defects.



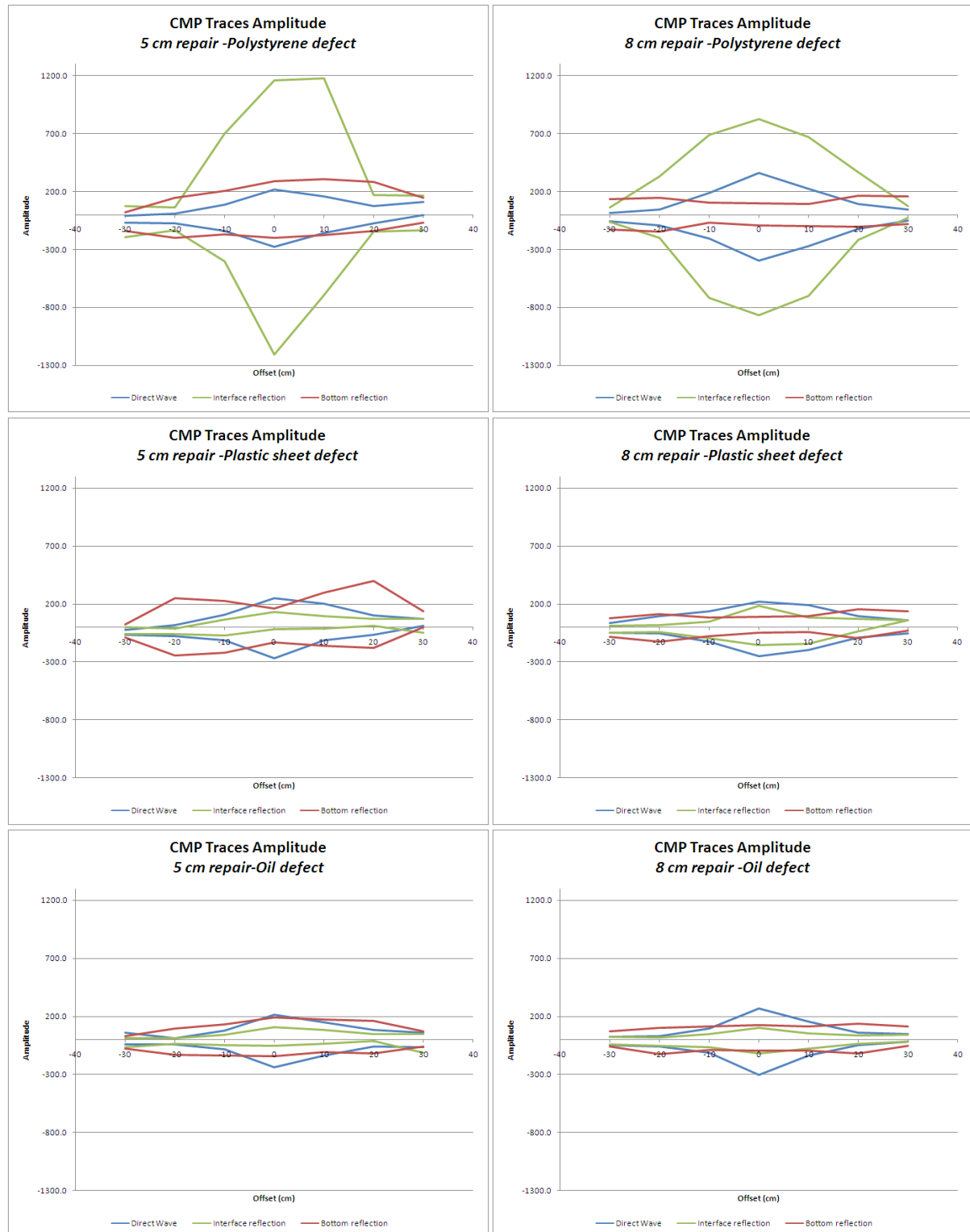


Figure 36 : Radargram maximum and minimum amplitude of the different waves in function of the offset

From the graphs on Figure 36, we can make several observations. First, for some slabs, as for example in the case of the plastic sheet and thin repair, we have a global increase of the background amplitude. For some other slabs, the change is not progressive but sharp, and happens in the middle of the profile. This was also observed in the 2D CMPs described in the previous chapter. Anyway, we have both maximum and minimum values, so it is easy to

distinguish a real increase in amplitude from a background change, because in this case the minimum and maximum values are shifted in the same direction.

The maximum amplitude of direct wave is almost always situated about 200. The only exception is the 8 cm/polystyrene defect slab, in which it amounts to 360. Anyway, as we could expect for surface waves, both the shape and the amplitude remain quite constant from one slab to another. For what concerns the waves reflected on the interfaces, the amplitude is highly variable depending on the defect type. For both oil and no defect, the amplitude of this wave is very small. The same phenomenon can be observed in the case of the plastic sheet, even if the amplitude seems slightly higher in the case of the thicker repair. For the polystyrene defects, the amplitude of this wave is really high and reaches 1200 in both positive and negative directions. In some graphs, we can observe a slight increase of the amplitude for larger offsets. It doesn't reflect any real tendency but it is induced by the reflection from the bottom, very close to the reflection at the interface for large offset values.

Finally, the waves reflected on the bottom of the slabs have a specific shape. We could expect their highest amplitude to be measured for the zero offset and then to simply decrease as the path and consequently the attenuation increase (cf. §2.1). If it is the case for both direct waves and waves reflected at the interface, it is not anymore for the bottom reflections. For a majority of samples, we can observe that the highest amplitude occurs for an offset situated about 20 cm, while for the offset zero the amplitude is quite low. This is clearly visible in Figure 37, which is the 3D representation of the double CMP radargram for the slab with no defect and thick repair.

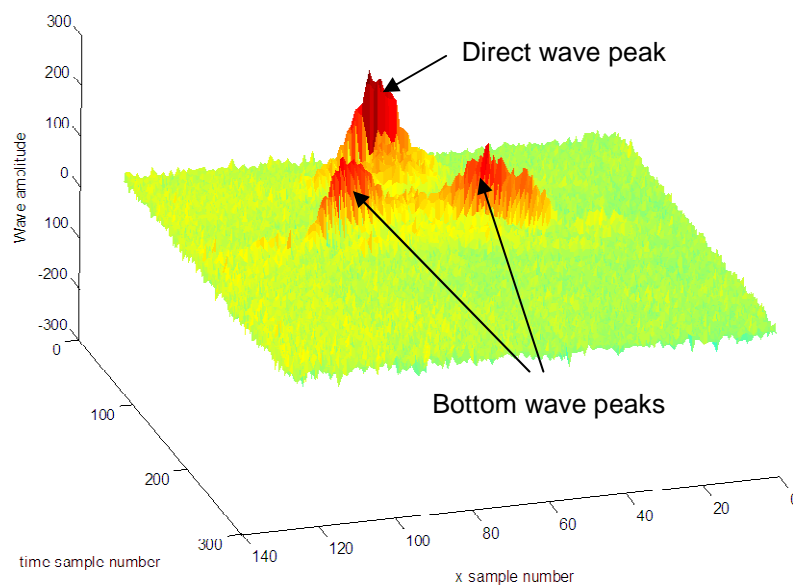


Figure 37 : Visualization of amplitude variations with offset (slab 1.2.4)

This increase of amplitude with the offset cannot be due to the presence of numerous other peaks at that point, because we can see that the huge reflections from the interface in the case of polystyrene defects have no real influence on the shape of the bottom hyperbolas (Figure 36). To explain this phenomenon, we can suggest several hypotheses:

- the thickness of our slab is not really important and the waves are very close to one another on the radargrams. In most of the profiles, we can find in the peak area the reflections from the bottom, the double reflections from the interface and the critically refracted waves. Even if all those waves don't seem to have a high amplitude, their addition could create apparent peaks in this areas;
- the acquisition was made with parallel antennas, so the radar radiation pattern could have an influence on the results. This radiation pattern should be measured on the antennas to confirm or invalid this assumption;
- at the bottom of the slab, we have wooden planks, visible in substrate slabs profiles (cf § 5.4). We could imagine that a complex thin-bed reflection would happen in this zone, in which we have concrete-air, concrete-wood and wood-air interface. Deparis (Deparis and Garambois 2007) showed that for thin-bed reflections, we could sometimes observe a similar variation in the reflection amplitude with the offset (Figure 38). This could be another path of investigation to explain our amplitude variation.

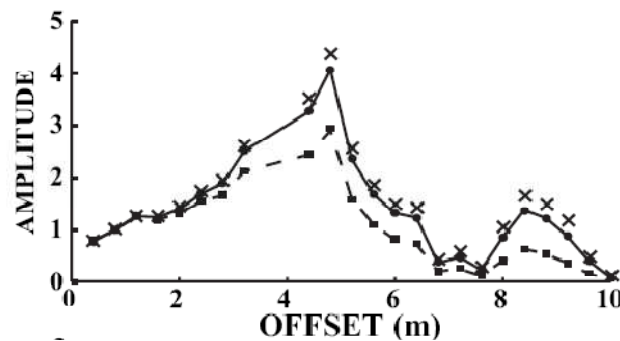


Figure 38 : Amplitude variations of the reflectivity compare to the offset of a studied event at 140 MHz.
Dashed lines represent raw data and plain lines represent data corrected from propagation effects
(Deparis and Garambois 2007)

8 *Profiles 3D visualisation*

As explained in the paragraph 6.2, 26 different profiles were measured for each slab: 11 longitudinal and 15 lateral profiles. Each profile could be analyzed separately, with a similar method that the one used for the substrate slabs characterization (§ 5.4). Anyway, it is more convenient to have a complete 3D visualization of each situation. If a 3D matrix is represented opaquely, only the sides of the volume are visible and the visualization of targets within the block of data is not possible. To solve this problem, we can use a translucent visualization of the data, permitting to distinguish the targets situated inside the data through the volume. This is made possible by the alpha-rendering options of Matlab. This method was described by Conroy (Conroy and Radzevicius 2003).

8.1 Data processing for visualization

The first step of slabs representation consists in the calculation of the initial and final times of the scans corresponding to the slab. The initial time is easy to determine because it corresponds to the maximum of the mean trace. To evaluate the double travel time of reflection on the bottom of the slab, the mean trace of the whole radargram is calculated and the bottom peak is isolated in its range of possible occurrence. This range is fixed from 2 to 3.6 ns and corresponds to a range of thickness from 10 to 18 cm with a speed of 10 cm/ns. The initial and bottom times calculated by this method will constitute the limits of the studied zone of the radargram.

The time limits have to remain the same for the whole slab, so those calculations are only realized on one profile, which is supposed to be representative of the total surface. We chose to use for each case the profile corresponding to the middle of the slab. We also used the length of this profile as a reference, because all the radargrams must have the same dimensions to be assembled into a 3D matrix and represented with Matlab.

For all the profiles, a typical response associated with the structure without defect was calculated. In most of the cases, the mean of the 20 first traces can correspond to this definition because most of the defects are situated in the middle of the slab. This mean trace was then suppressed from each profile, in order to increase the relative amplitude of the defects reflections. The original profile, the mean profile and the result of their difference can be observed on Figure 39, representing the slab 1.2.1, which contains a large polystyrene defect.

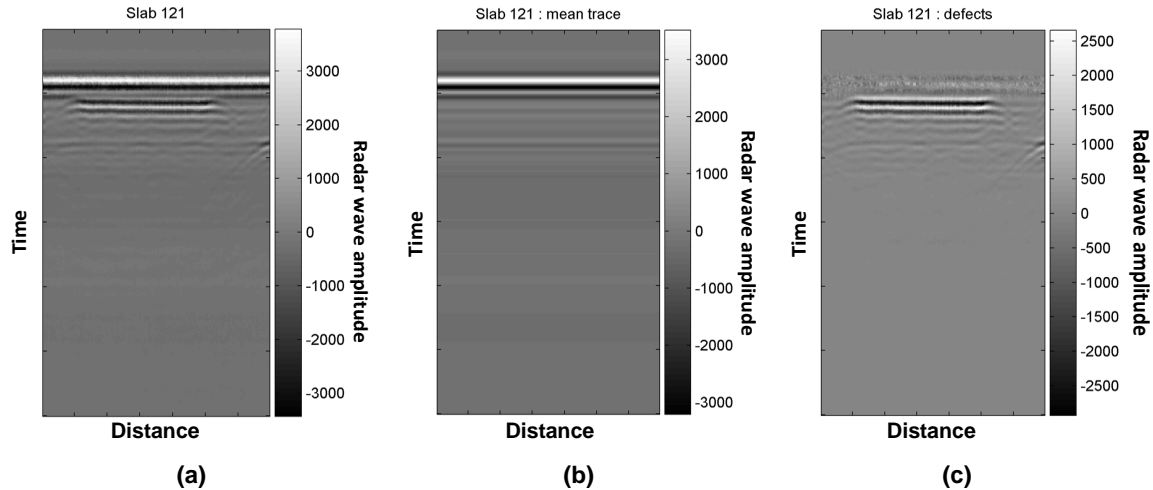


Figure 39 : Slab 121 (a) rough data (b) mean trace calculation (c) mean trace removal

Each profile is then registered as a 2D component of a global 3D matrix. If we are looking for local defects, it can be interesting to suppress from each profile a mean profile corresponding to a zone without defect. A mean profile may for example correspond to an average between a few profiles measured near the edges of the slab if the defect situated is in the middle of the slab. For example, the reflections from the edges and from the wooden palette are erased by this method. Anyway, it doesn't work if we don't have any profile corresponding to a zone without defect: this operation shouldn't consequently be applied in every situation.

We can also observe that the most intensive noise is concentrated in the very first nanoseconds, corresponding to the first few millimeters of the slab. As any reflection could hardly be distinguished in this zone, we decided to mask the first ten samples of each profile ($\approx 5\text{ mm}$), which enhances the visualization of the defects.

To represent the 3D matrix without creating any interpolation between the rough results, we will use the Matlab function 'slice'. This function allows the user to draw 2D slices along the x, y or z directions inside a 3D matrix. In our case, we will draw one slice per profile. This visualization is still opaque, so the first radargrams hide the others. To solve this problem, we use the alpha-rendering options of Matlab, which associates a different transparency to the different amplitudes. The scale of alpha-rendering was associated with the scale of colors, the maximum opacity corresponding to the negative (dark) reflections. By this way, we tried to limit the number of reflections from each target. For both the colors and the translucency, the contrast can be adapted to have a better visualization of the targets.

To enhance the 3D visualization of the slabs, a box is drawn around the data and the horizontal axes lengths are set equal to the dimensions of the slab. The vertical axis length is dependent on the double travel time of the slab. The proportions of the slabs are fixed to have the possibility to see the difference between thick and thin slabs on the graph.

All the operations previously described allow to represent the results of a set of parallel profiles in a tridimensional visualization. Those operations can be applied on the 11 longitudinal profiles or on the 15 lateral profiles. On Figure 40, we can observe the results obtained on slab 1.2.1 with the longitudinal and lateral profiles. To gather on a single 3D

graph all the information registered on one slab, it is possible to simply superimpose the two sets of results with the 'hold on' function.

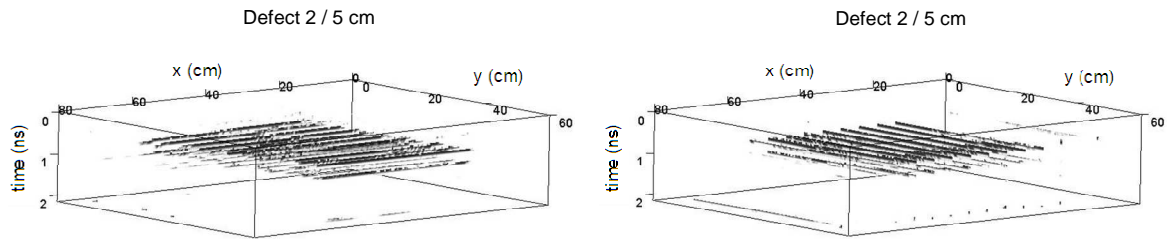


Figure 40 : Longitudinal and lateral 3D results on slab 121

8.2 Results display

For every defect, the 3D maps resulting from the superposition of the longitudinal and lateral profiles are represented. The contrast used for the representation is kept constant for a same defect. The scales and the decomposition between longitudinal and lateral profiles are given in Appendix 7. Figure 41 offers the representation of the results obtained on the slabs with no defect for both repair thicknesses.

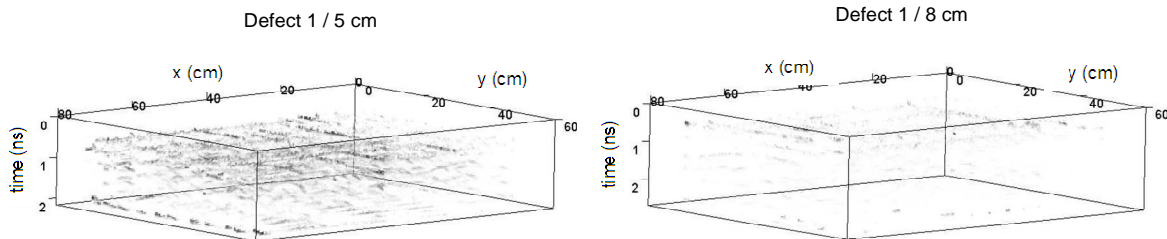


Figure 41 : 3D defect vision - no defect (slabs 1.2.3 and 1.1.3)

We observe that the results are quite different for the two slabs. For the 5 cm thick repair, we have a relatively continuous noise, while for the thicker repair we have almost no trace. Anyway, for both slabs, it is quite clear that no local defect is detected. As well as the real slabs, the 3D visualizations appear with different total thicknesses. We could replace the time axis by a depth axis, but it would remain an approximation, because this visualization is not sufficient to determine the speed of the waves into the concrete. Moreover, we have two different materials in which the speeds are different. Thus, the depth axis wouldn't be linear but bi-linear, with two different scales.

Figure 42 represents the results for the polystyrene defects, which cover the total width of the slabs and are 40 and 10 cm wide

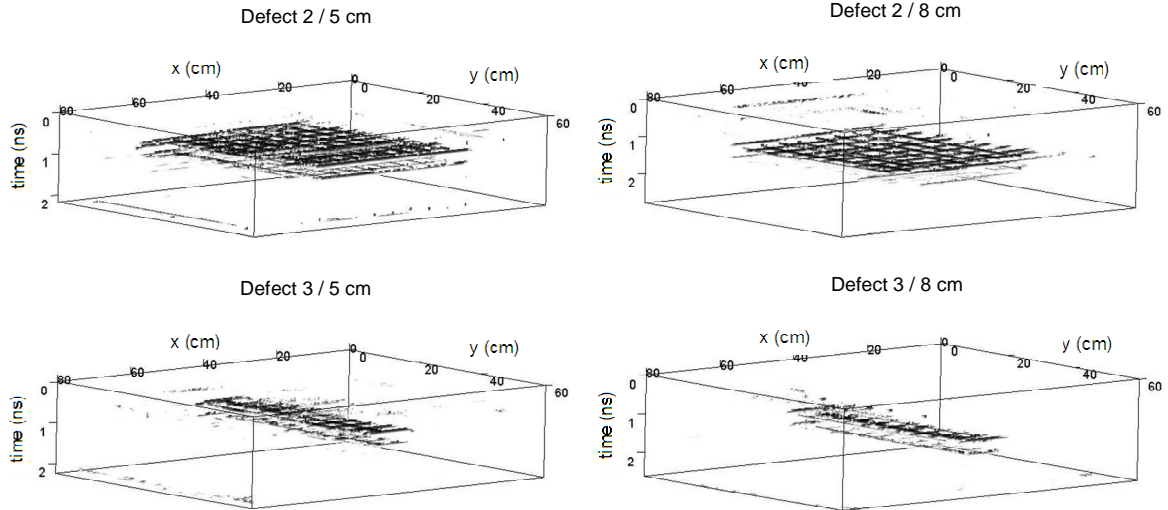


Figure 42: 3D defect vision – polystyrene defects (slabs 1.2.1, 1.1.1, 1.2.2 and 1.2.1)

We observe that the polystyrene defects are clearly visible with this method. The reflection amplitude and intensity seems to be slightly higher for the thinner repair. We can also observe, for the large defect and thick repair, that the defect doesn't seem horizontal by comparison to the superior limit of the slab. This could be explained by a lateral variation of the speed of the repair material, which seems nevertheless unlikely in the case of such a liquid repair material. In fact, this inclination corresponds to a real inclination of the substrate slab during the moulding of the repair layer. The difference of thickness between the two extremities of the slab is about 1.5 cm.

On Figure 43, the results are displayed for the plastic sheets. Defect 4 corresponds to a large rectangular plastic sheet ($40 \times 20 \text{ cm}^2$), while defect 5 has a smaller trapezoidal shape.

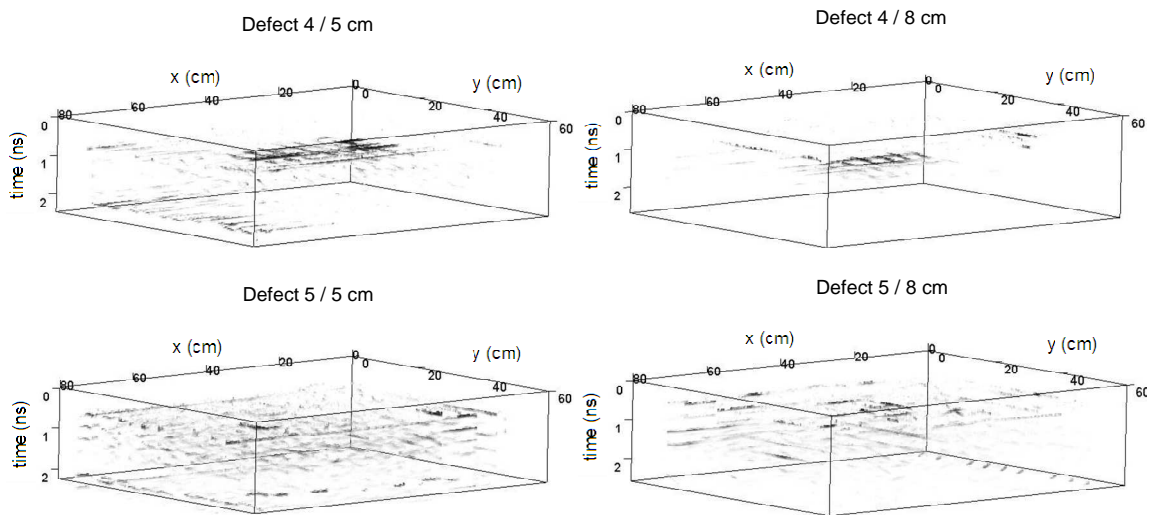


Figure 43 : 3D defect vision – plastic sheet defects (slabs 1.3.3, 1.3.2, 1.3.4 and 1.3.1)

The amplitude of the reflections from the plastic sheet is much lower than in the case of the polystyrene panels. Nevertheless, for the big rectangular plastic sheets, the place and size of

the defect are quite neat. For the little trapezoidal defect, however, the defect is less clear. Let's rotate those representations to observe the defects from an upper view (Figure 44):

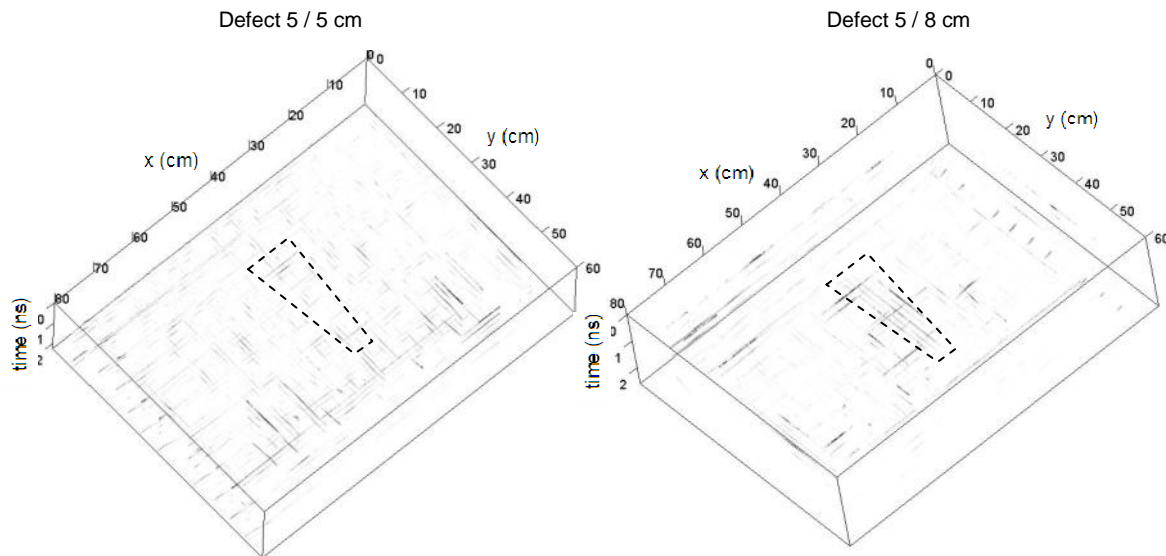


Figure 44 : Upper view of slabs with trapezoidal plastic sheet (slabs 1.3.4 and 1.3.1)

We can see, for the 5 cm thick repair, a reflection on one profile that probably corresponds to the defect; however, generally speaking, the reflections from the zone of the defect have the same order of magnitude than the noise in the zones without defects. For the 8 centimeters thick repair layer, the defect is more visible. Five profiles seem to show reflections in the zone of the defect. The longitudinal traces don't seem to be really aligned as they should be, but this can be caused by an irregular initial offset of the antenna.

Eventually, the results for the slabs with a layer of oil on a rectangle of dimensions 34 x 54 cm² are presented in Figure 45:

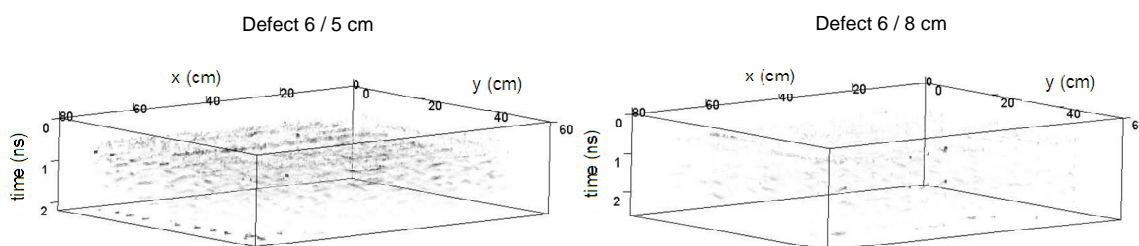


Figure 45 : 3D defect vision – oil defect (slabs 1.1.4 and 1.2.4)

We can observe that the defects are similar to those obtained for no defect. We have a global noise for the slab with a thin repair and not many reflections for the case of the thick repair. However, the same visualization parameters have been used for both slabs. Anyway, in the case of the oil, a doubt can subsist in the possibility to discern a local defect, because the distance from the defect to the edges of the slab is, in our case, not much bigger than the initial offset of the antenna. That means that the mean trace removed from all the traces could already correspond to a zone with presence of oil. Anyway, this hypothesis is highly improbable; the most satisfying explanation for the invisibility of the interface is simply that

the contrast of dielectric permittivities between normal concrete and concrete spread with oil is not sufficient to observe a reflection.

8.3 Resolution

The resolution of the method can be determined for the polystyrene and plastic sheet defects. We can observe in every case a quasi perfect vertical superposition of the lateral and longitudinal results. The horizontal superposition of the results is less perfect, mainly due to the initial offset of the antenna, which can be variable from one profile to another. This can be observed in the case of a very local defect such as the trapezoidal plastic sheet (see Figure 44). To be sure to get a good precision about the defects location, it is thus very important to control carefully the initial position of the antenna.

On the profiles crossing a defect, the size of the defect is generally quite close to the real dimensions of the defects. Anyway, when the reflection from the defect is not very strong, which is the case for the plastic sheet, the shorter defects can go totally unnoticed. It is the case for the trapezoidal plastic sheet, which has in each point a width inferior to 10 cm, and which appears only in about half of the transversal scans. According to the theory (cf. §2.5.2), the lateral resolution should be better for deeper defects. It doesn't clearly appear in our results, maybe because of the small depth variation between the defects.

The dimension of the defect perpendicular to the profiles directions is less easy to determine. If the measurement is clearly over the defect, we can see it on the radargram. If it is over the edges of the defects, it is totally visible in some cases while, in other situations, it is perceptible but with smaller amplitude; sometimes, the presence of the defect can go totally unnoticed. This last situation systematically occurs in the case of the plastic sheet. As example, we can observe on Figure 46, which corresponds to large plastic sheet and thick repair, that the length of the defect is about 40 cm. For the width of the defect, we count 3 profiles, with a 5 cm interval. This means that we are sure the defect width is at least equal to 10 cm. We have an incertitude of 5 cm at each edge of the defect!

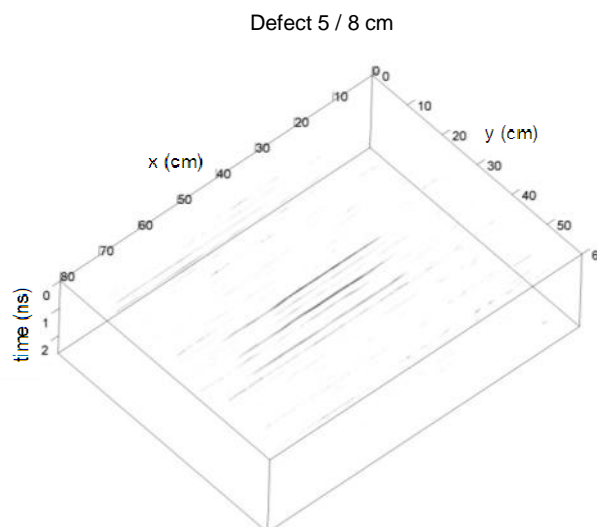


Figure 46 : Upper view of defect 4 – longitudinal profiles

In order to summarize the information obtained from analysis, we observe, if dx is the distance between two adjacent profiles,

- a very small incertitude for the defect dimension parallel to the acquisition direction;
- an incertitude of $2 \cdot dx$ for the defect dimensions perpendicular to the profiles.

If we produce profiles in only one direction, doubling the number of profiles seems to divide by two the incertitude on the width of the defect. A better solution is to realize perpendicular profiles, which directly gives precise information about the transverse dimension.

8.4 Influence of concrete age

To study the influence of concrete age on the results, the same sample (1.3.2 – 8 centimeters thick repair and large plastic sheet) was tested both 15 and 30 days after the repair. 3D results are represented in Figure 47.

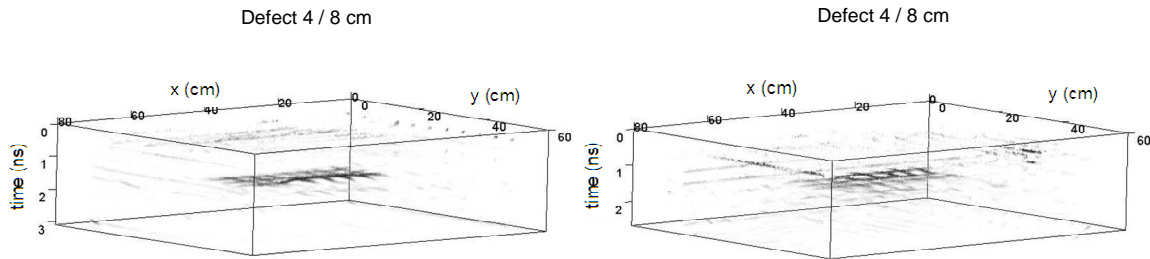


Figure 47 : Comparison of 3D results obtained 15 and 30 days after moulding

Firstly, it is important to note that the lateral scans were realized in different directions. This is why the stronger zone of reflection doesn't seem to appear at the same place in both cases. Anyway, the bigger difference between the two profiles is the time at which the defect and the bottom of the slab appear. The defect appears at 1.5 ns for 15 days after the repair and at 1.3 ns 15 days later. The defect is of course still situated at the same place: the difference is only due to a speed decrease.

In fact, when the concrete gets older, its water content decreases, and, consequently, its dielectric permittivity, as mentioned in § 2.6.1. The speed into concrete is proportional to the inverse of the square root of the dielectric permittivity, which means it will increase when the water content decreases.

For both cases, we can write:

$$1.5 = \frac{2d}{v_{old}} \quad (62)$$

$$1.3 = \frac{2d}{v_{new}} \quad (63)$$

By eliminating the distance between equations (62) and (63), we get the relationship between the two different speeds:

$$\frac{v_{old}}{v_{new}} = \frac{1.3}{1.5} = 86.7\% \quad (64)$$

The time of reflection from the bottom of the slab is also different in both cases. This is still due to the difference of speed into the repair material; but a slight difference of speed in the substrate concrete, due to the humidity increase induced by the repair moulding, is not to be categorically rejected.

9 Comparison with Impact-Echo results

The radar results can now be compared to the slabs characterization obtained with impact-echo. The impact-echo tests were performed and analyzed by Piotr Harassek, from Warsaw University of Technology. He made one measurement every 10 cm, which corresponds to 35 measurements per slab, and used a steel ball diameter of 5 mm. The results are displayed in Figure 48.

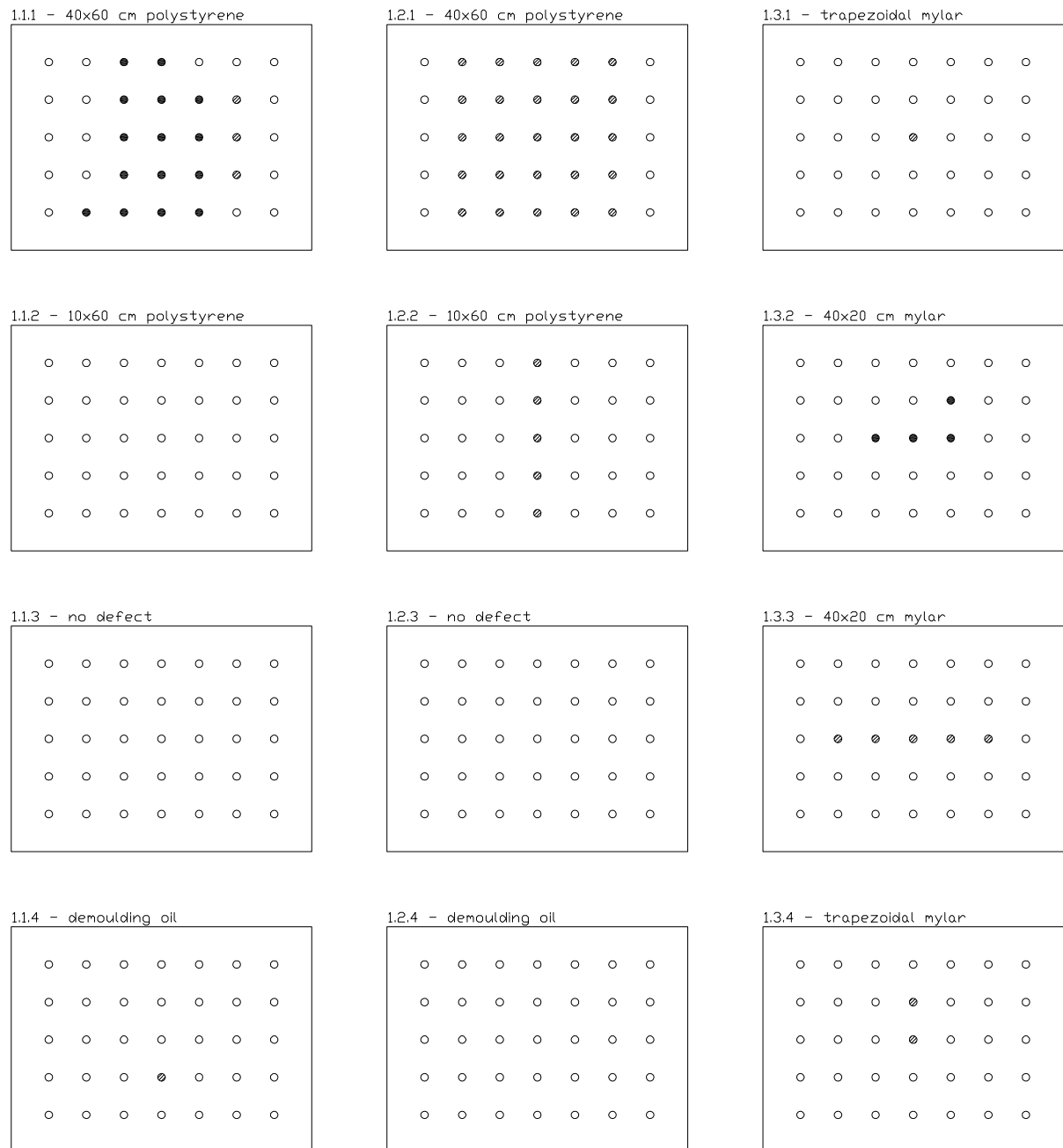


Figure 48 : Impact-echo results

The white points correspond to signals in which only the bottom peak is visible, as in Figure 49 (a); the black ones correspond to signals in which the interface is clearly visible and its depth can be determined (Figure 49 (b)). Finally, the grey points correspond to unclear signals: there is something at the interface that clearly corrupts the response, but it is not possible to determine its depth.

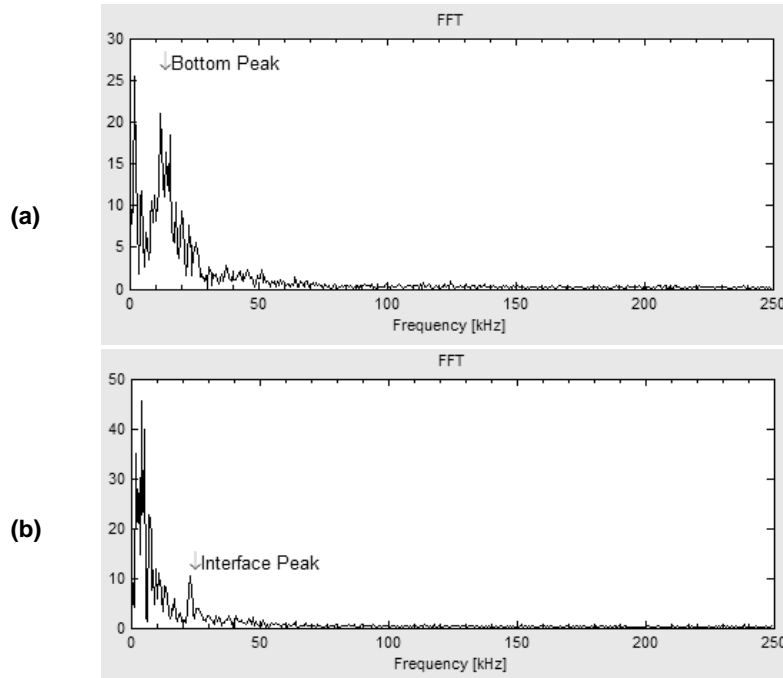


Figure 49 : Impact-echo signals (a) zone without defect (b) zone with clear interface peak

We can observe that some anomalies are generally detected when a defect is present. However, the precision in the size of defects is low, except in the case of polystyrene. For the big polystyrene and plastic sheet defects, we observe that the interface peaks are only visible for 8 cm thick repairs; a 5 cm layer is too thin for the interface peak to appear on impact-echo signals.

For the plastic sheet defects, a very strange signal was registered with impact-echo, as if the presence of the Mylar sheet corrupted the signal. This makes this kind of defects very easy to distinguish from the other ones.

If we compare the impact-echo results to the radar ones, we note that the precision in defects localization is better with GPR. The determination of the depth of defects with impact-echo was only possible in a few cases, while with radar we can calculate the depth of every visible defect. This could be due to the thin repair layers used in this study. Moreover, radar allows representing the tested structures in 3D, when impact-echo only gives punctual results. On the other hand, an advantage of impact-echo over radar is that it is less dependent on the environmental conditions and especially the water content of the concrete.

Conclusion

The concrete deck slabs decay is a complex pathology involving several individual degradation mechanisms and generally leading to the apparition of delaminations in the upper part of the slabs. Before carrying out any repair, it is important to understand the origin of the problem and evaluate the degradations extent. In this prospect, the non-destructive methods, and particularly radar technique (GPR), appear to be performing and more and more widespread tools.

The objective of this work was to simulate slab delaminations into laboratory concrete samples and to develop a GPR acquisition procedure with a signal treatment method in order to analyze and visualize the defects. Twelve concrete substrate slabs were cast and then repaired after surface treatment. Six different defects (created with plastic sheets, polystyrene panels or demoulding oil) were introduced at the interface between the concrete substrate and the repair material. The influence of defect size was also studied by the introduction of smaller polystyrene and plastic sheet.

Before repair, the substrate slabs were characterized with GPR. The speed of radar waves into the concrete was determined and a first profile visualization code was written. The roughness of the surfaces before repair was also evaluated by sand patch test and optical evaluation (ATOS). An attempt of correlation between the results of the two methods was also made, but the results are not really convincing, probably because of the too low roughness which is very close to the range of validity of the two methods.

After repair, the radar measurements were performed on the samples, using two different acquisition methods. The first one was the CMP (common midpoint) and allows to test only one point of the structure and to deduce the thickness and radar waves speed of the different layers. The main difficulties in this type of acquisition were the complexity of the resulting signals and the time zero determination.

The evolution of the wave amplitudes versus the offset was also studied on double CMP radargrams, showing the influence of the defect type on the amplitude of the wave reflected at the interface. In the case of the waves reflected on the bottom of the slabs, we could also observe that the maximum amplitude doesn't correspond to the zero offset as we could expect. Different hypotheses could explain this phenomenon, but they should be checked by further investigations.

The second radar acquisition method is the profile measurement. We measured 26 profiles on the surface of each slab and set up a data treatment method allowing the representation of the slabs in 3D, the defects appearing at the interface by transparency. The polystyrene defects turned out to be highly visible with this method. The plastic sheet defects appear with lower amplitude, but are clearly detected when their surface is sufficient. Finally, the presence of demoulding oil at the interface goes totally unnoticed and those samples can't be distinguished from the reference slabs.

The precision in determining the defects extent by profiles measurements was also evaluated. The defect dimensions are determined quite precisely in the direction parallel to the profile while, in the perpendicular direction, the incertitude on the defect extension is equal to two times the distance between two profiles. The realization of a second set of profiles, perpendicular to the first one is thus more interesting than a multiplication of the number of profiles in the same direction to improve the precision in the lateral direction. The importance of a good precision in the initial radar position was also demonstrated.

Finally, the influence of the concrete age, linked to its water content, was studied by the realization of the same 3D visualization on the basis of profiles performed 15 days apart on the same slab. If the plastic sheet defect was equally visible, we noticed that the double travel time of the waves reflected on the defect was more important for the older slab, which highlights the influence of water content on the radar wave speed into concrete.

The experimental part of this work was realized in collaboration with Piotr Harassek, who tested the samples with another non destructive technique: impact-echo. A comparison between the two sets of results showed that the radar is globally more accurate in the defects detection, even if most of the defects were detected by impact-echo as well. The thickness of the repair was probably too low – especially for the 5 cm thick repairs – to get accurate impact-echo results.

The perspectives of this work are multiple. Firstly, the study of CMPs needs to be improved by image treatment methods and complementary experimental measurements (about the antenna radiation pattern or the initial offset for example). To analyze the complex data appearing on those radargrams, a finite difference computer model of wave propagation would also be a useful tool.

Moreover, the measurements should be repeated in time to have a long-term monitoring of the evolution of wavespeed and defects visibility. The humidity factor should also be taken into account, because the water content is a key factor in the radar wave propagation speed into concrete.

Finally, the whole set of treatment and visualization methods described in this work should be tested on data from real delaminated bridge deck slabs. Some parameters as the presence of humidity, waterproofing sheet, steel rebars, or the absence of filling material into the cracks could have a huge influence on the defects visibility.

Bibliography

- Al-Qadi, I. L., and S. Lahouar. 2005. Measuring layer thicknesses with GPR - Theory to practice. *Construction and Building materials* 19 (10):763-772.
- Annan, A. P. 2005. Ground-Penetrating Radar. In *Near-Surface Geophysics Part 1: Concepts and Fundamentals*, edited by D. K. Butler: Society of Exploration Geophysicists, 357 - 438.
- Balayssac, J. P., V. Kringkaï, M. Sbartaï, G. Klysz, S. Laurens, and G. Arliguie. 2007. Contribution au développement du radar pour la caractérisation non destructive du béton. In *25e rencontres de l'AUGC*. Bordeaux: LMDC.
- Barret, B. 2004. LOADRD3 (Matlab function), Leeds.
- Bennett, S., O. C. Jones, M. Sené, and G. F. Phillips. 2009. *Electricity and Magnetism* (National Physical Laboratory). Kaye & Laby 2009 [cited 10 May 2009]. Available from http://www.kayelaby.npl.co.uk/general_physics/#2_6.
- Bissonette, B., L. Courard, A. M. Vaysburd, and N. Bélair. 2006. Concrete removal techniques: influence on residual cracking and bond strength. *Concrete International* 28 (12):49-55.
- Bourdi, T., J. E. Rhazi, F. Boone, and G. Ballivy. 2008. Application of Jonscher model for the characterization of the dielectric permittivity of concrete. *Journal of Physics D-Applied Physics* 41 (20).
- Bungey, J. H. 2004. Sub-surface radar testing of concrete: a review. *Construction and Building materials* 18 (1):1-8.
- Carino, N. J. 2003. Nondestructive Test Methods to Evaluate Concrete Structures. In *Sixth CANMET/ACI International Conference on Durability of Concrete*. Thessaloniki, Greece.
- Cemart. 2009. Cemtop 320. Lommel.
- Conroy, J. P., and S. J. Radzevicius. 2003. Compact MATLAB code for displaying 3D GPR data with translucence. *Comput. Geosci.* 29 (5):679-681.
- Courard, L. 2008. *Maintenance, entretien et réparation des constructions en béton*. Edited by CdC.
- Courard, L., and B. Bissonette. 2004. Essai dérivé de l'essai d'adhérence pour la caractérisation de la cohésion superficielle des supports en béton dans les travaux de réparation: analyse des paramètres d'essai. *Materials and Structures* 37:342-350.
- Courard, L., A. Garbacz, and L. Wolff. 2006. Chapter 4: Evaluation and quality assessment. In *RILEM TC 184-IFE "Industrial Floors"*, edited by P. Seidler. Bagneux: Rilem publications, 59-89.
- Courard, L., and D. Schwall. 2006. Effect of concrete substrate texture on the adhesion properties of PCC repair mortar. In *International Symposium Polymers in Concrete*, edited by J. Barroso de Aguiar. Guimaraes, Portugal: University of Minho, 99-110.
- Courard, L., J. Wiertz, A. Darimont, and R. Degeimbre. 1995. Influence of operating conditions and humidity on adherence of repair mortar. In *International Congress on Polymers in Concrete*. Oostende, 585-590.
- Demars, P., P. Gilles, E. Dondonne, G. Lefebvre, A. Darimont, G. Lorenzi, G. Henriët, and A.-M. Marion. The degradation of the bridge decks slabs in Belgium mainly involves alkali-aggregates reactions.
- Deparis, J., and S. Garambois. 2007. Inversion of dispersive APVO GPR curves: a thin-layer approach for fracture characterization on a vertical cliff. In *4th International Workshop on Advanced Ground Penetrating Radar*. Aula Magna Partenope.
- Dérobert, X., J. Iaquina, G. Klysz, and J.-P. Balayssac. 2008. Use of capacitive and GPR techniques for the non-destructive evaluation of cover concrete. *NDT & E International* 41 (1):44-52.
- Emmons, P. H., and B. W. Emmons, eds. 1993. *Concrete repair and maintenance illustrated : problem analysis, repair strategy, techniques*. Kingston, MA: R.S. Means Co. 295 p.

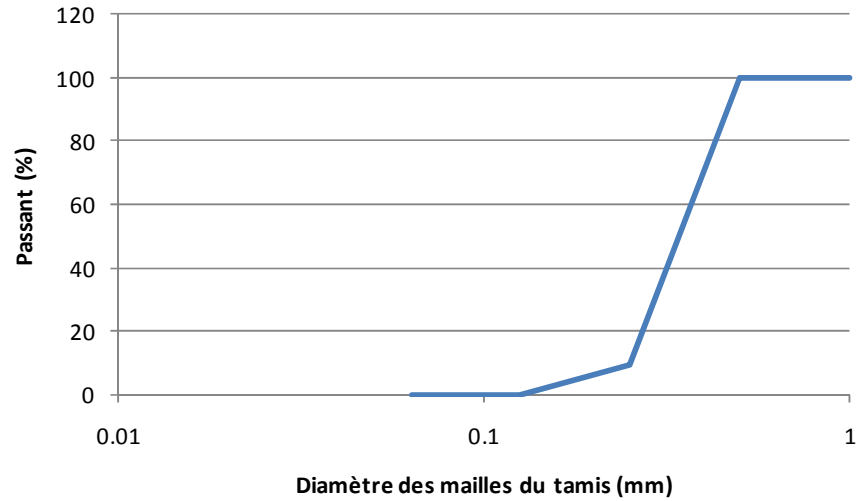
- Ferrieres, X., G. Klysz, P. Mazet, and J. P. Balayssac. Evaluation of the concrete electromagnetics properties by using radar measurements in a context of building sustainability. *Computer Physics Communications* In Press, Accepted Manuscript.
- Gagné, R. 2009. *GCI 714 - Durabilité et réparations du béton* [Notes de cours]. Université de Sherbrooke 2009 [cited 10 février 2009]. Available from <http://www.civil.usherbrooke.ca/cours/gci714/>.
- Garbacz, A., L. Courard, and K. Kostana. 2006. Characterization of concrete surface roughness and its relation to adhesion in repair systems. *Materials Characterization* 56 (4-5):281-289.
- Gilles, P. 2004. Investigation et réparation des ouvrages atteints de pourrissement de dalles de tablier de ponts. In *Diagno-béton*. Montréal.
- Gilles, P., and P. Toussaint. 2007. Les besoins en CND d'un gestionnaire d'ouvrages d'art. In *Diagnobéton*. Aix en provence.
- Hugenschmidt, J., and R. Loser. 2008. Detection of chlorides and moisture in concrete structures with ground penetrating radar. *Materials and Structures/Materiaux et Constructions* 41 (4):785-792.
- INDOT. 2009. *Certified Technician Program Training Manual for Bridge Construction and Deck Repair*. Indiana Department of Transportation, 2008 2007 [cited 16 march 2009]. Available from <http://www.in.gov/indot/3092.htm>.
- Klysz, G., J. P. Balayssac, and X. Ferrières. 2008. Evaluation of dielectric properties of concrete by a numerical FDTD model of a GPR coupled antenna--Parametric study. *NDT & E International* 41 (8):621-631.
- Lacroix, R., and J. A. Calgaro. 1999. Pathologie et évaluation des ponts existants. In *Techniques de l'ingénieur*.
- Mala. RAMAC/GPR CUII. In *Operating manual*.
- Mays, G. C., T. P. Lees, A. F. Baker, L. J. Tabor, and J. G. Keer. 1992. *Durability of Concrete Structures*. Edited by G. Mays. London: E & FN Spon.
- Mommer, P., E. Dondonne, and P. Demars. 2004. Dégradation des dalles de tablier de ponts en Région Wallonne. Etude d'une pathologie complexe. *Revue scientifique des ISILF* (18).
- Pérez-Gracia, V., F. García García, and I. Rodríguez Abad. 2008a. GPR evaluation of the damage found in the reinforced concrete base of a block of flats: A case study. *NDT & E International* 41 (5):341-353.
- Pérez-Gracia, V., R. González-Drigo, and D. Di Capua. 2008b. Horizontal resolution in a non-destructive shallow GPR survey: An experimental evaluation. *NDT & E International* 41 (8):611-620.
- Raupach, M. 2006. Concrete repair according to the new European Standard EN 1504. In *Concrete Repair, Rehabilitation and Retrofitting*, edited by M. Alexander, F. Beushausen, F. Dehn and P. Moyo. Cap Town: Taylor & Francis Group, 6-8.
- Reynolds, J. M. 1997. *An Introduction to Applied and Environmental Geophysics*. Chichester: John Wiley & Sons.
- Sansalone, M., and W. B. Street. 2009. *The Impact Echo Method*. NDTnet 1998 [cited 10 May 2009]. Available from <http://www.ndt.net/article/0298/streett/streett.htm>.
- Sansalone, M. J., and W. B. Street. 1997. *Impact-echo. Nondestructive evaluation of concrete and masonry*. Jersey Shore: Bulbrier Press.
- Schwall, D. 2005. Analyse de l'effet des techniques de préparation sur la rugosité des surfaces en béton. Master Thesis, GeMMe, ULg, Liège.
- Soutsos, M. N., J. H. Bungey, S. G. Millard, M. R. Shaw, and A. Patterson. 2001. Dielectric properties of concrete and their influence on radar testing. *NDT & E International* 34 (6):419-425.
- UBAtc. 2002. Revêtements de protection des surfaces en béton soumis aux influences extérieures et non soumis au trafic. In *Guide d'agrément et de certification n°G0008*.
- Viriyametanont, K. 2008. Reconnaissance physique et géométrique d'éléments en béton armé par radar et RNA. PhD Thesis, LMDC, INSA, Toulouse.

Appendixes

Appendix 1 : Substrate slabs compressive strength

	Dim 1 (cm)	Dim 2 (cm)	Height (cm)	Weight (kg)	Destructive load (kN)	Density (kg/m ³)	Compressive strenght (MPa)
Sample 1	15.0	15.0	15.0	8.05	645	2385.2	28.7
Sample 2	15.0	15.0	14.6	7.90	665	2404.9	30.4
Mean	15.0	15.0	14.8	7.98	655	2395.0	29.6

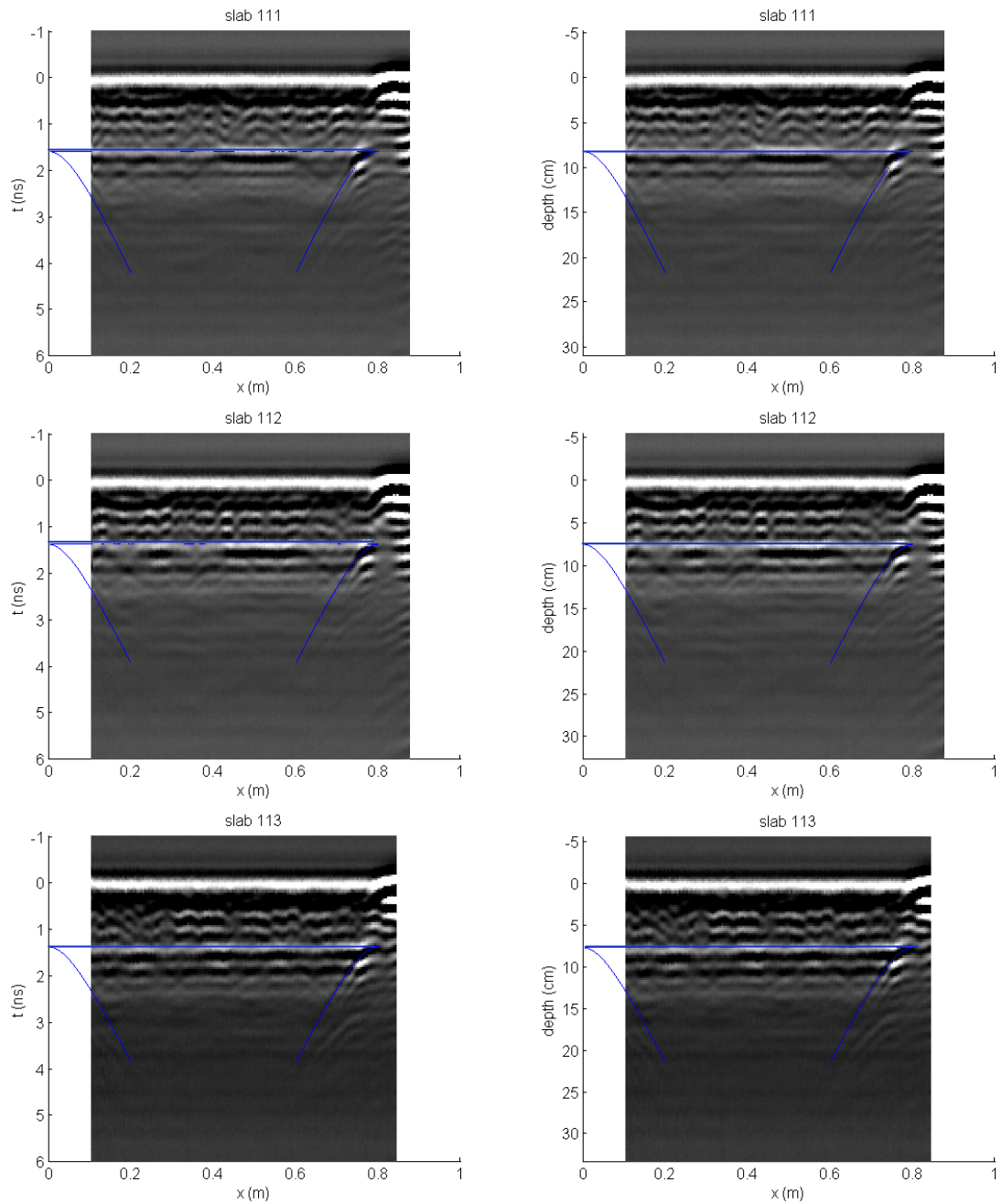
Appendix 2 : Granulometric curve of the sieved sand used for sand patch test

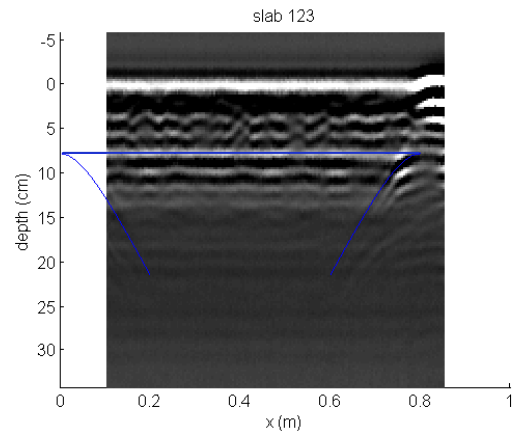
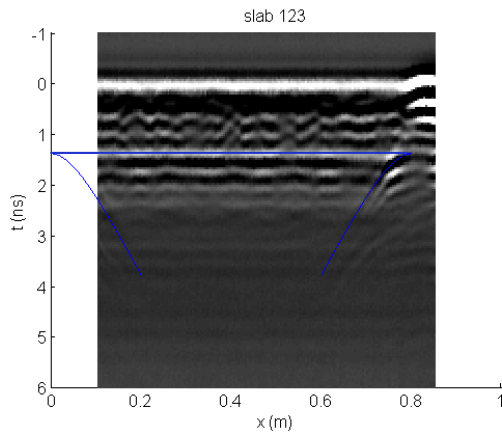
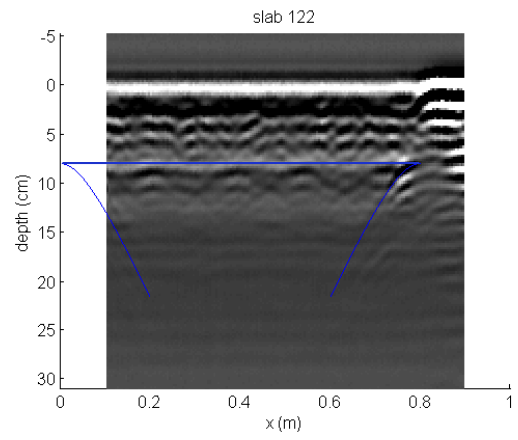
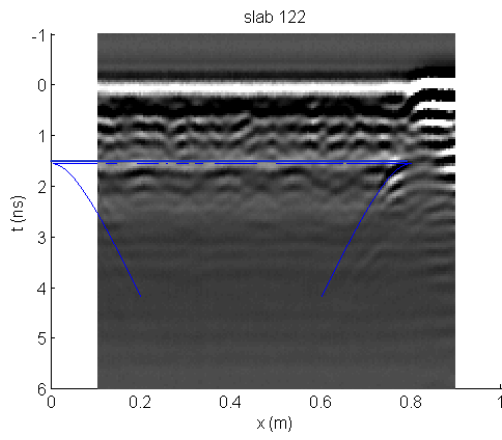
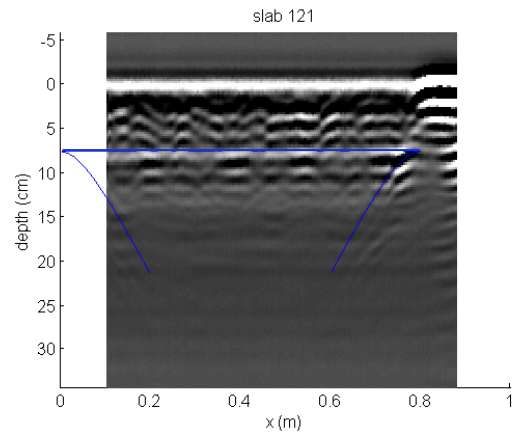
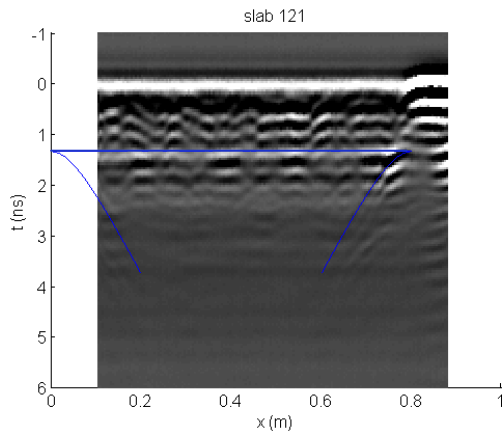
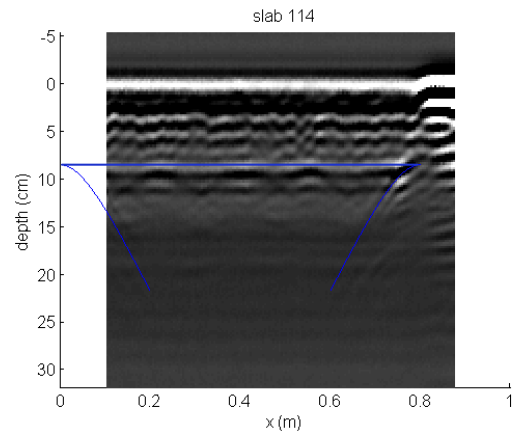
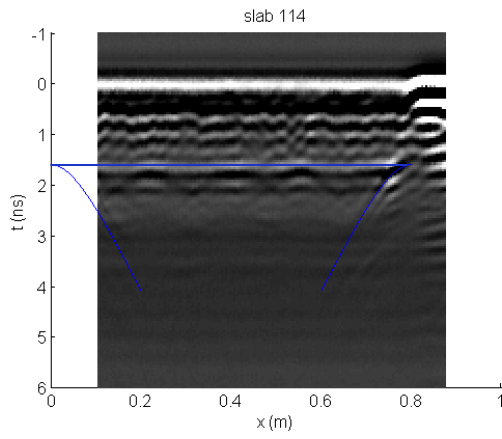


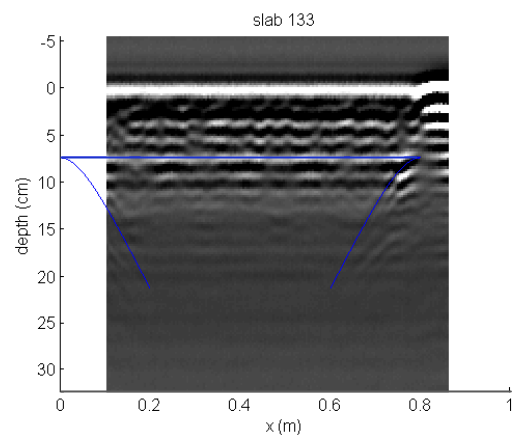
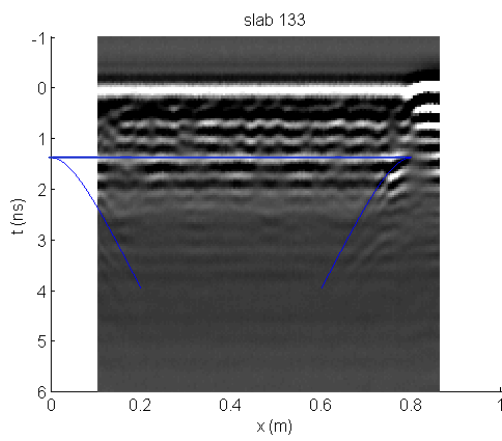
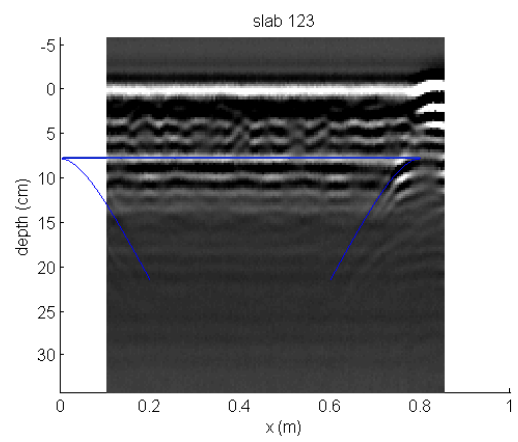
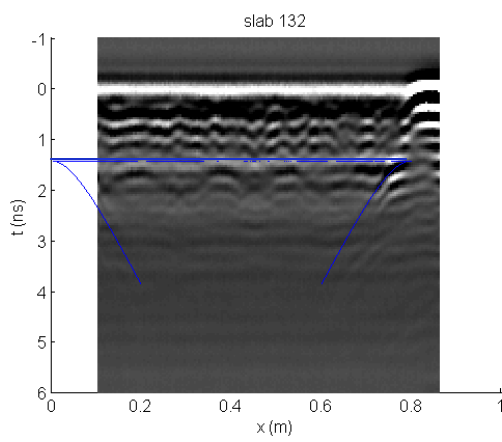
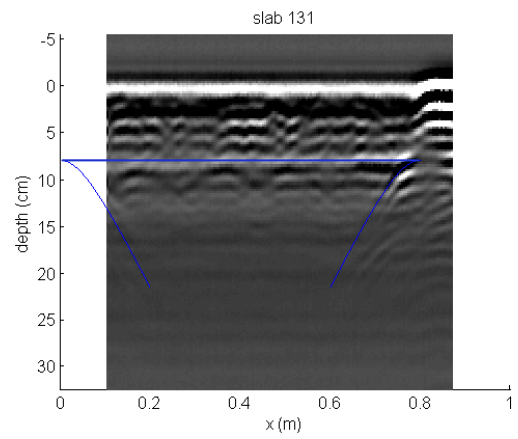
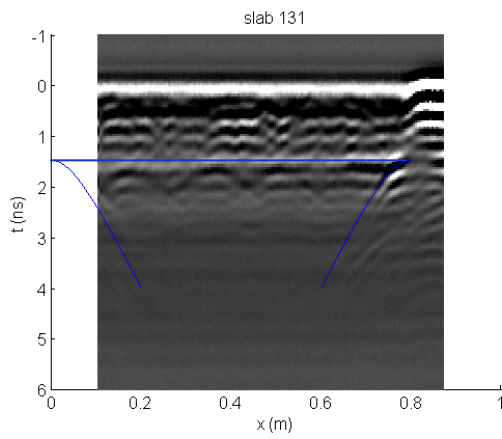
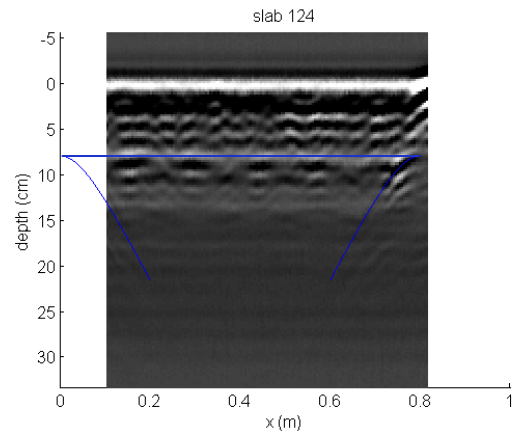
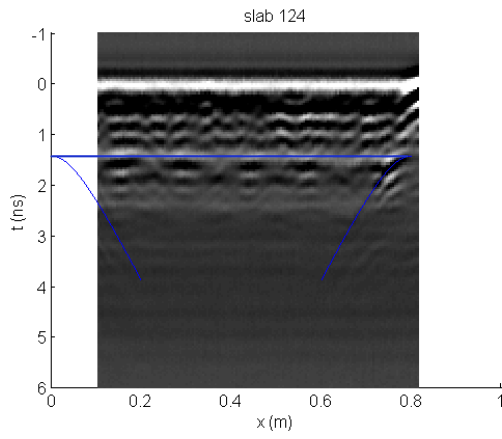
Appendix 3 : Substrate slabs thicknesses and defects

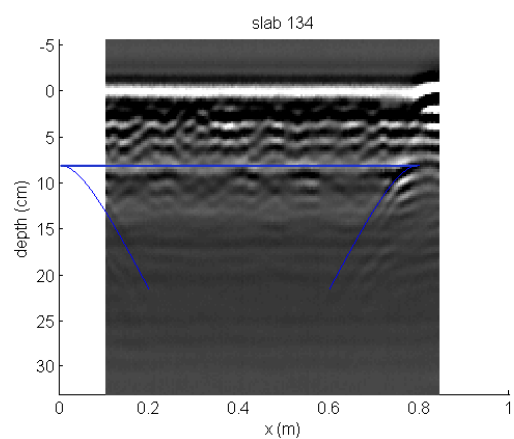
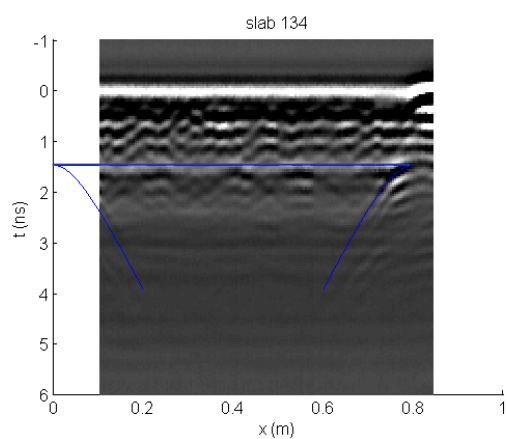
Slab n°	Substrate slab thickness (cm)	Mortar thickness (cm)	Total thickness (cm)	n° defect
1.1.1	8.03	8.05	16.08	2
1.1.2	7.28	7.8	15.08	3
1.1.3	7.45	4.15	11.6	1
1.1.4	8.3	3.95	12.25	6
1.2.1	7.43	4.53	11.95	2
1.2.2	7.8	4.68	12.48	3
1.2.3	7.65	7.2	14.85	1
1.2.4	7.7	6.93	14.63	6
1.3.1	7.73	6.93	14.65	5
1.3.2	7.73	7.35	15.08	4
1.3.3	7.2	4.85	12.05	4
1.3.4	7.88	4.53	12.4	5

Appendix 4 : Substrate slabs profiles









Appendix 5 : Repair mortar product sheet and compressive tests results



CEMART BVBA
Maatheide 76
E-3920 Lommel

T 0032 (0)11/52.51.10
F 0032 (0)11/52.51.09
E info@cemart.be

Cemtop 320

DESCRIPTION DU PRODUIT

CEM TOP 320 est un produit d'arasage auto-égalisant composé de ciment à haute teneur d'alumine, d'agréats, de liants et d'additifs chimiques. C'est une poudre sèche pré-mélangée. L'application se fait en épaisseurs de 4 à 30 mm en une seule opération. Dans des conditions normales, le passage piétonnier sur le sol est possible après 1-2 heures, la pleine charge finale après 1 à 3 jours, en fonction des conditions du site.

APPLICATIONS

CEM TOP 320 est conçu pour être utilisé comme couche d'égailisation fine pur usage industriel et commercial, convenable pour charges légères et mi-lourdes. Ce produit est idéal comme substrat pour des couches de résine. CEM TOP 320 est conçu pour être appliqué à l'aide d'une pompe-mixer automatique. Pour des espaces plus petits, les matériaux peuvent être mélangés aussi dans un seau à mélanges avec un mixeur manuel, après on peut l'appliquer sur le sol.

SUBSTRAT

CEM TOP 320 doit être appliqué sur un substrat correctement préparé. Poussières, laitier de ciment ou autres matériaux mous comme l'asphalte doivent être enlevés. L'épaisseur normale est de 6 à 10 mm, mais une épaisseur de 25 à 30 mm peut être posée dans une seule opération. Des déclivités peuvent être maintenues vers une évacuation d'eau en utilisant une quantité d'eau réduite et en pompant depuis le haut vers le bas. Le matériau en voie de durcissement peut être aisément formé ou coupé, permettant ainsi d'effectuer tous les ajustements nécessaires.

DONNEES TECHNIQUES

Teneur en eau de 18 % 50 % HR et température de 20 °C pendant le processus de durcissement.

Résistance à la flexion	8 N/mm ² après 28 jours.
Résistance à la compression	> 32 N/mm ² après 28 jours.
Adhérence au substrat	> 3N/mm ²
Valeur VOC	Libre d'ammoniaques et de formaldéhyde
Dimension des particules	max. 1 mm.
Retrait admissible	<0,05% mesuré sous H.R. de 55%
Valeur pH	environ 11,5
Fluidité	150 mm-155mm
Stabilité à l'eau	Stable, (Expansion immergé<Retrait autorisé)

DONNEES D'APPLICATION (À 20°C)

Ajout d'eau	18% (4,5 litres/sac de 25 kg)
Test de liquidité, SS 923519	150 - 155 mm
Température minimum d'emploi	+ 6°C

Densité poudre sèche	environ 1,5 g/cm ³
Densité humide	> 1,9 g / cm ³
Durée de malléabilité	10 - 15 min. fonction de la température
Durcissement	1 - 3 heures pour accès piéton 24 heures pour accès de trafic léger 1 semaine pour pleine charge
Conservation	6 mois dans des conditions sèches, max. 20°C et 50%RH

PRÉPARATION DU SOUS-SOL

La surface à traiter doit être dure, saine et libre de toute contamination. Toute poussière sera évacuée à l'aide d'un aspirateur. Le laitier de ciment et les revêtements anciens seront enlevés par un procédé mécanique, par ex. brossage, brûlage de surface, ou grattage. Le béton poissé d'huile ou de graisse peut être traité au brûleur ou dégraissé par un produit approprié. Il faut appliquer du Cemprime sur le substrat.

MÉLANGE

CEM TOP 320 est conçu pour être mélangé par une pompe-mixer automatique. N'utiliser que de l'eau propre et potable à raison de 4,5 litres par sac de 25 kg. Le produit mélangé doit être utilisé endéans les 15 minutes.

NETTOYAGE

Chaque outil et équipement doit être nettoyé immédiatement à l'eau.

APPLICATION

Seuils de porte : les escaliers, évacuations et rigoles doivent être isolés à l'aide de bandes en caoutchouc mousse. Les plus grandes surfaces doivent être réparties en bandes. La largeur normale de chaque bande est de 4 – 12 mètres, suivant la capacité de la pompe.

SANTÉ ET SÉCURITÉ

Produit dangereux - contient du ciment, le ciment humecté est corrosif. Protéger les yeux et éviter le contact prolongé avec la peau. Tenir hors de portée des enfants. Pour plus d'informations consulter la feuille de données Santé et Sécurité.

ETIQUETAGE: SANTÉ ET SÉCURITÉ



Dangereux! Contient du ciment et du quartz.

ETIQUETAGE: TRANSPORT

Produit non répertorié

GÉNÉRALITÉS

Les informations générales contenues dans cette fiche technique, les conseils d'application et les autres recommandations sont fondés sur des examens et sur l'expérience. Cependant le client vérifiera lui-même l'aptitude à l'usage des produits. Les spécifications indiquées concernent des valeurs moyennes obtenues à 20 °C et 50 HR et établies selon l'état actuel de la technique. Les présentes descriptions techniques remplacent toutes les descriptions précédentes.

RE n°: TFE PA

TFE-PA1 Date d'essai: 21/04/09

ESSAI : COMPRESSION BARRETTES

Organisme : UNIVERSITE de LIEGE

Vitesse de mise en charge : 144. kN/min

Laboratoire : Matériaux de Construction

Humidité : 50 %

Opérateur : Jean DELHAMENDE

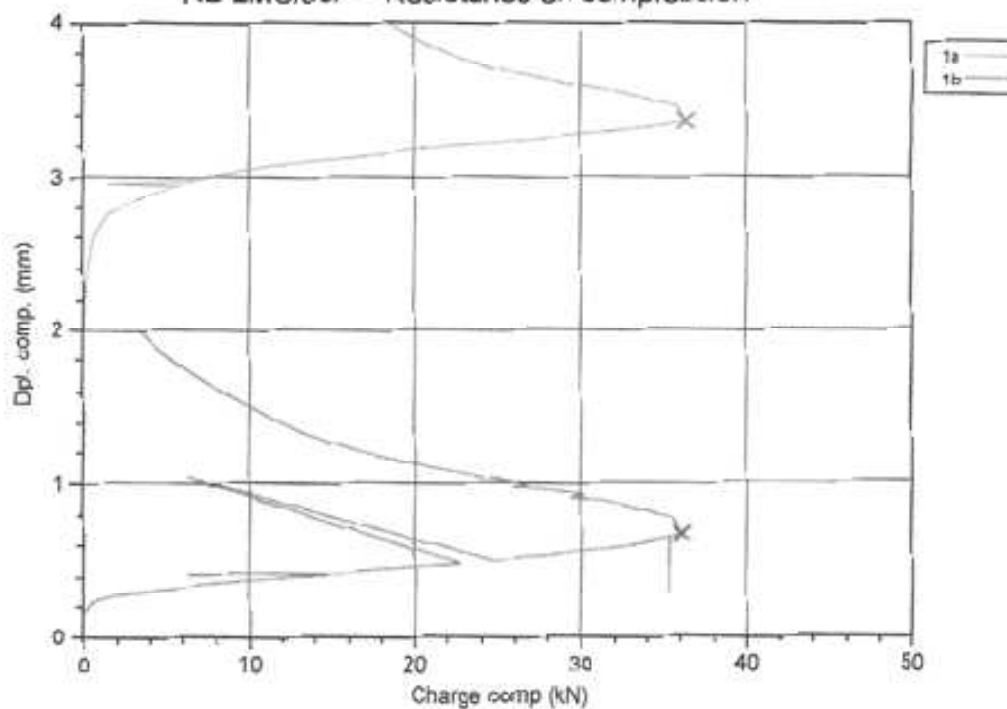
Température : 23°C

Norme : EN 196-1

Entrée utilisNon défini

TYPE :**ETAT :** ETAT DE LIVRAISON

RE LMC/09/ - Résistance en compression



	Contrainte Maximum (N/mm ²)	Charge max. (kN)	Larg. (mm)	Long. (mm)	Haut (mm)
1a	22.7	36.33	40.00	40.00	40.26
1b	22.6	36.11	40.00	40.00	40.26
Moyenne	22.6	36.22	40.00	40.00	40.26

RE n°: TFE PA

Date d'essai: 28/05/09

ESSAI : COMPRESSION BARRETTES

Organisme : UNIVERSITE de LIEGE

Vitesse de mise en charge : 144. kN/min

Laboratoire : Matériaux de Construction

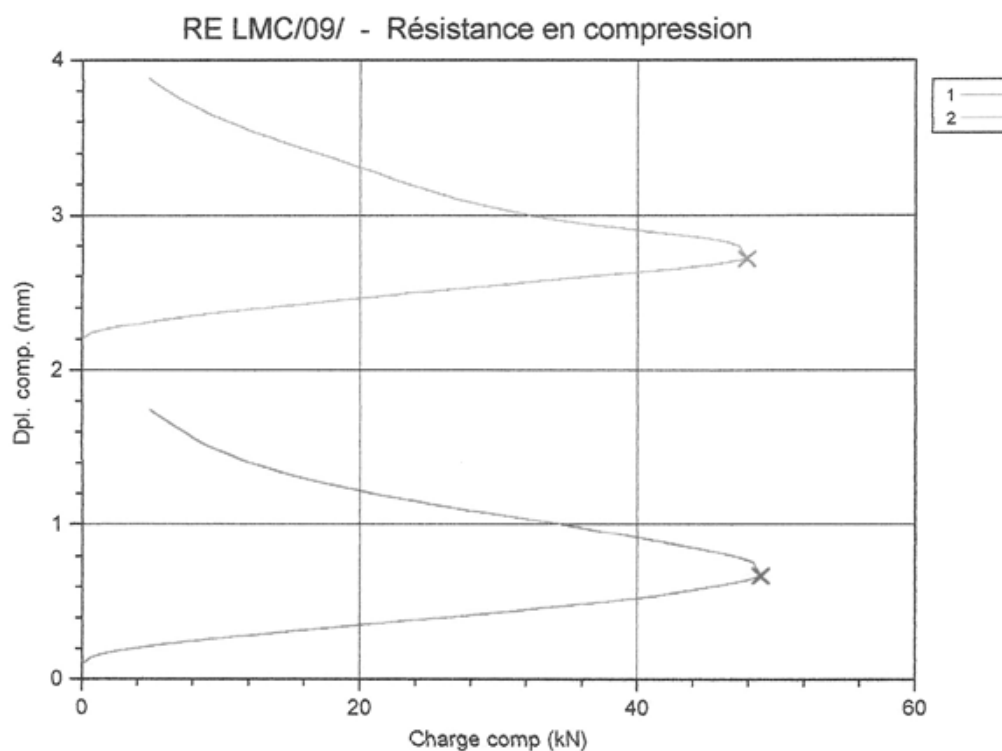
Humidité : 50 %

Opérateur : Jean DELHAMENDE

Température : 23°C

Norme : EN 196-1

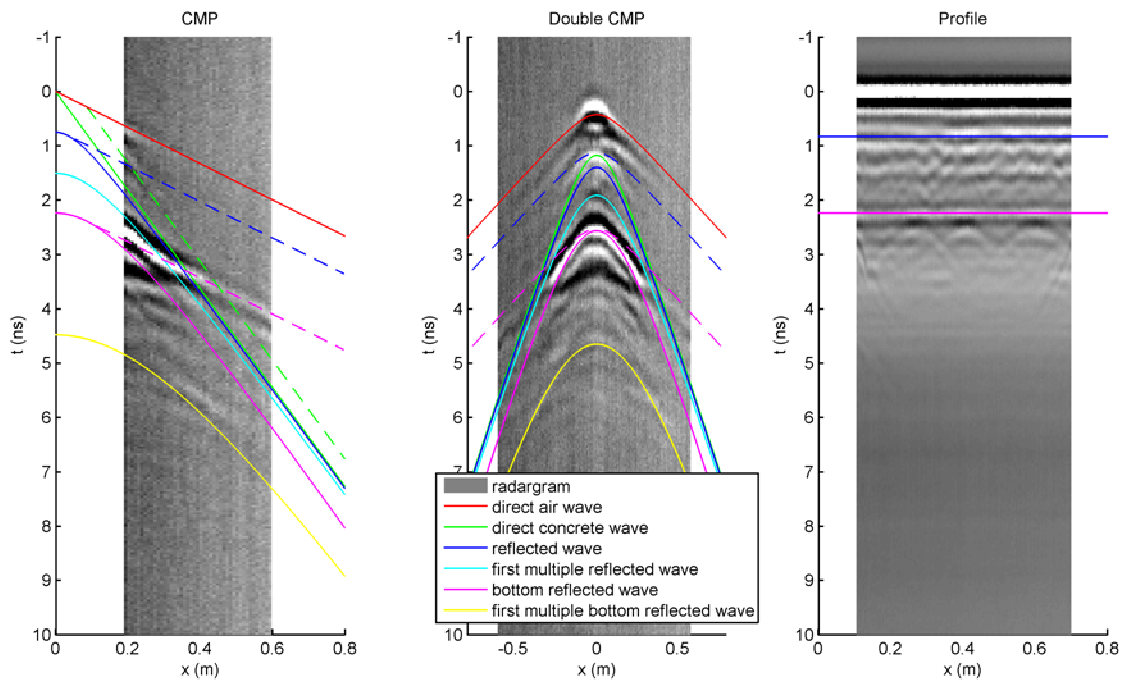
Entrée utiliNon défini

TYPE :**ETAT : ETAT DE LIVRAISON**

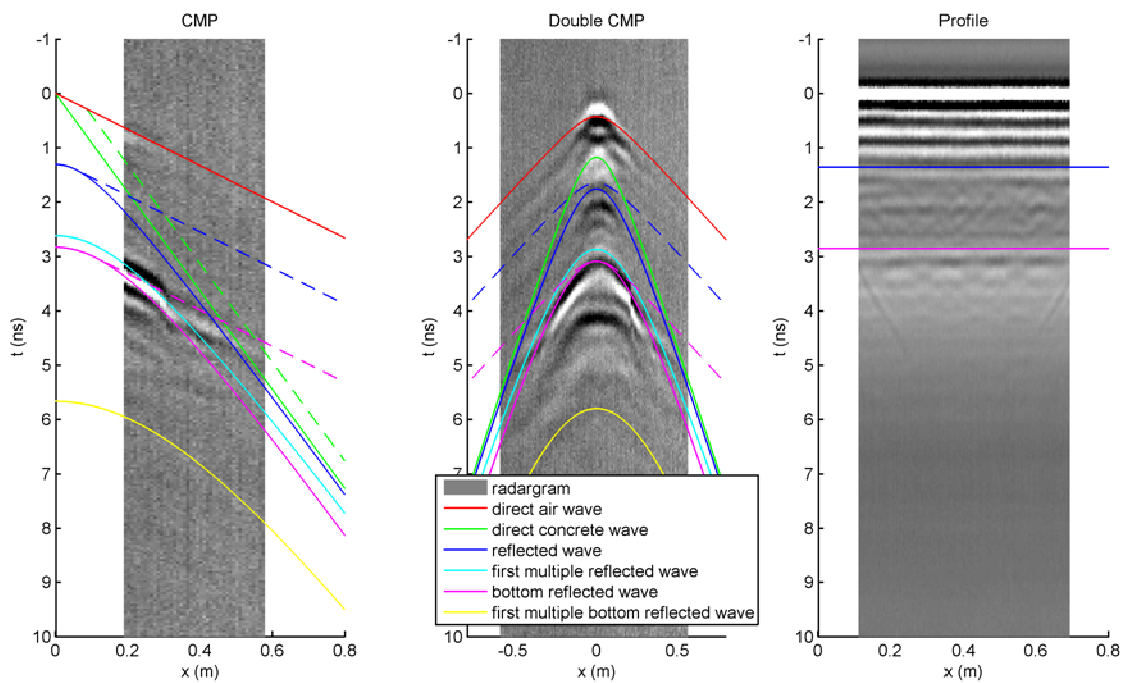
	Contrainte Maximum (N/mm ²)	Charge max. (kN)	Larg. (mm)	Long. (mm)	Haut (mm)
1	29.6	47.84	40.47	40.00	40.07
2	30.2	48.87	40.47	40.00	40.11
Moyenne	29.9	48.35	40.47	40.00	40.09

Appendix 6 : CMP results

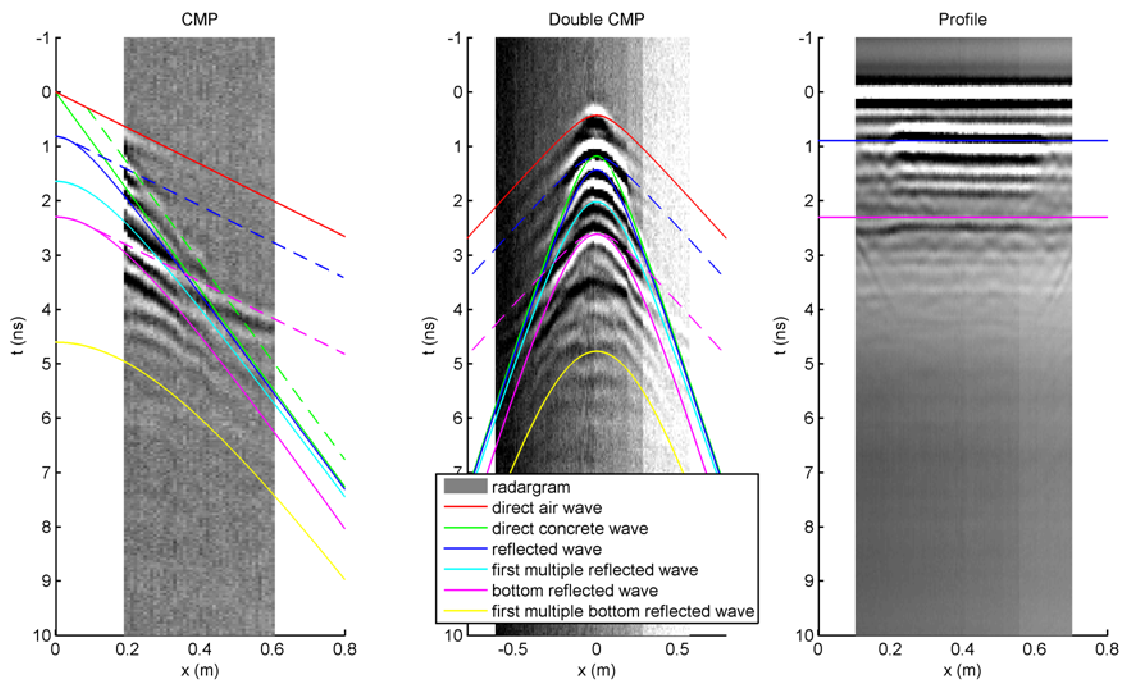
Slab 1.1.3: Defect 1 / 5 cm



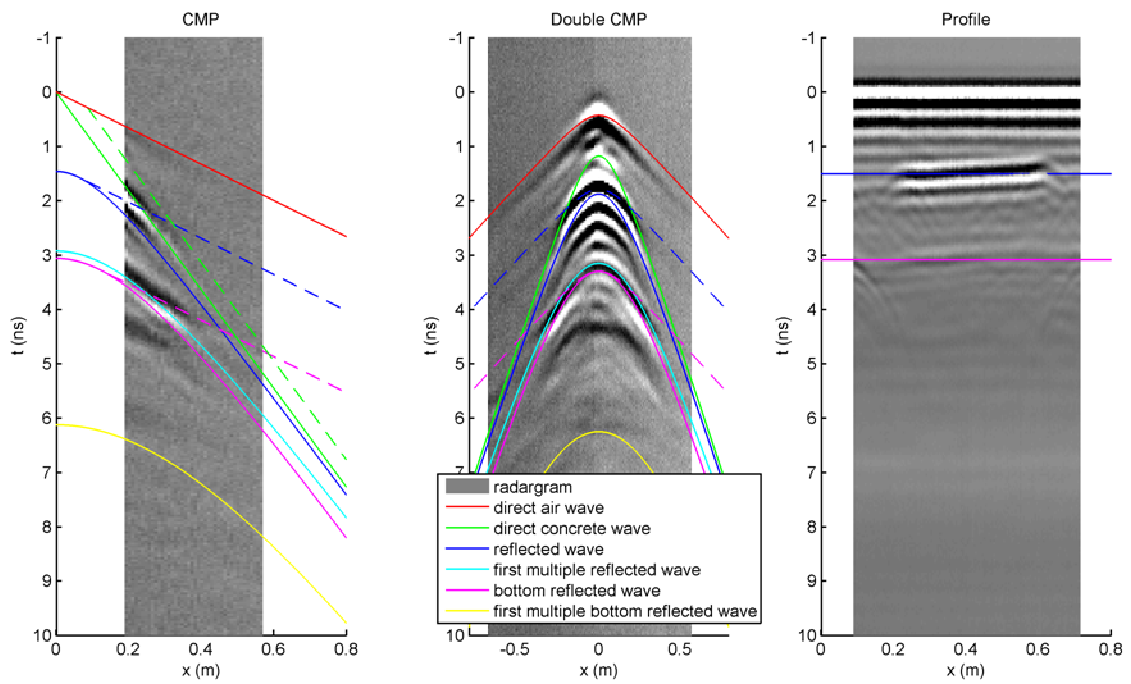
Slab 1.2.4: Defect 1 / 8 cm



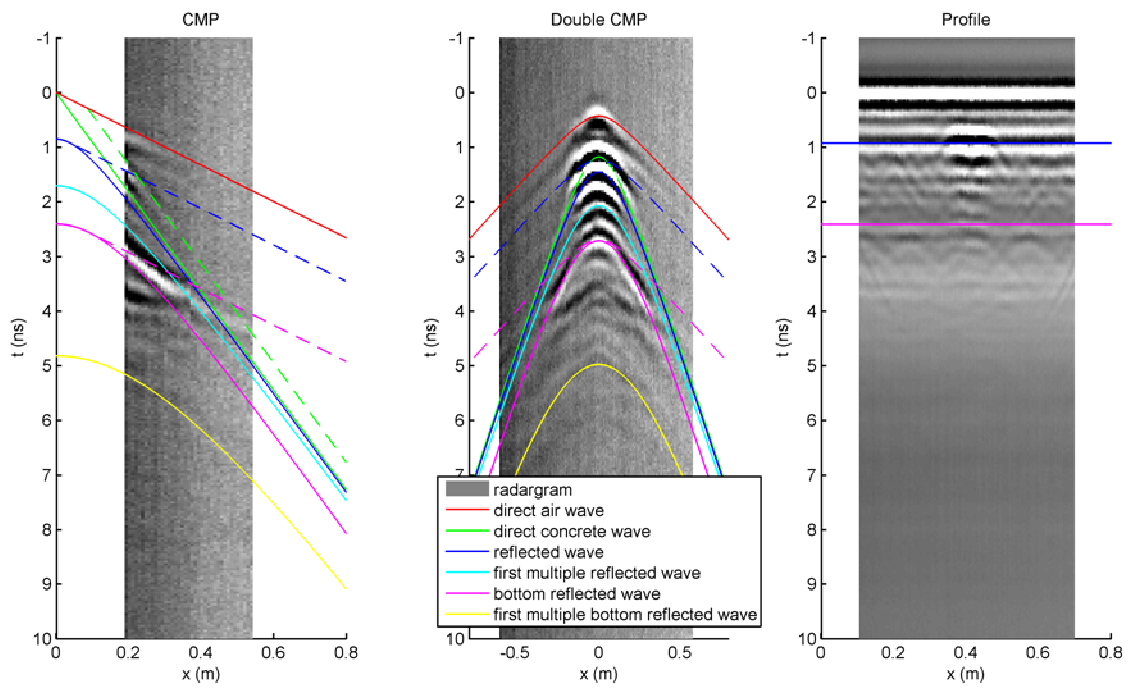
Slab 1.2.1: Defect 2 / 5 cm



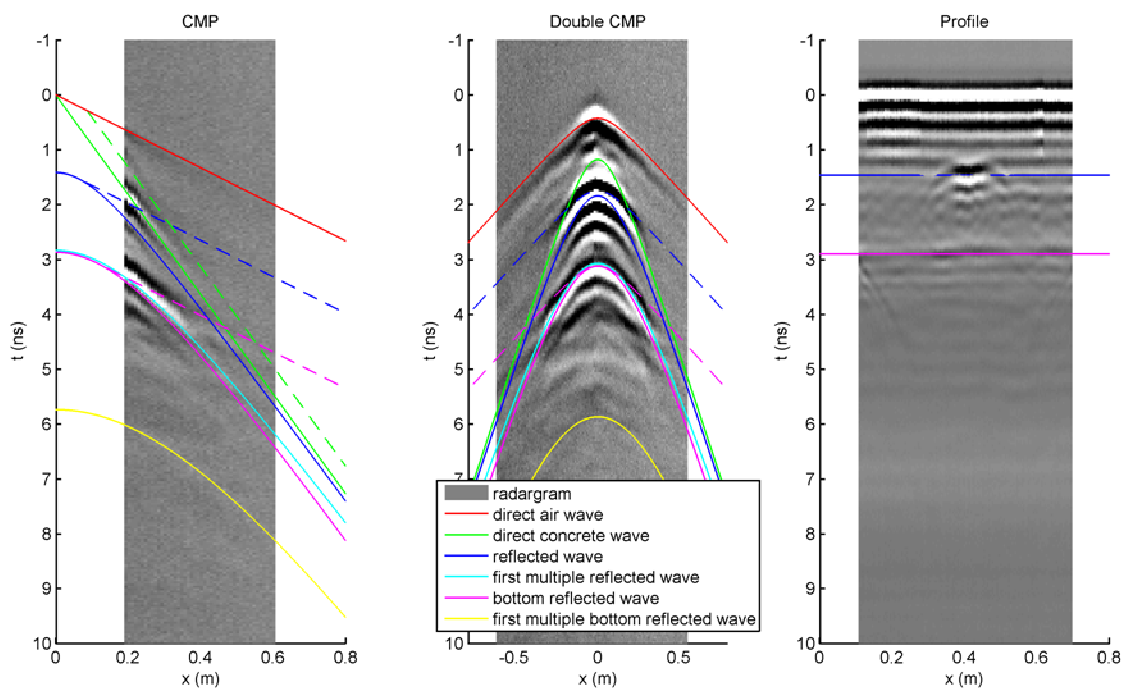
Slab 1.1.1: Defect 2 / 8 cm



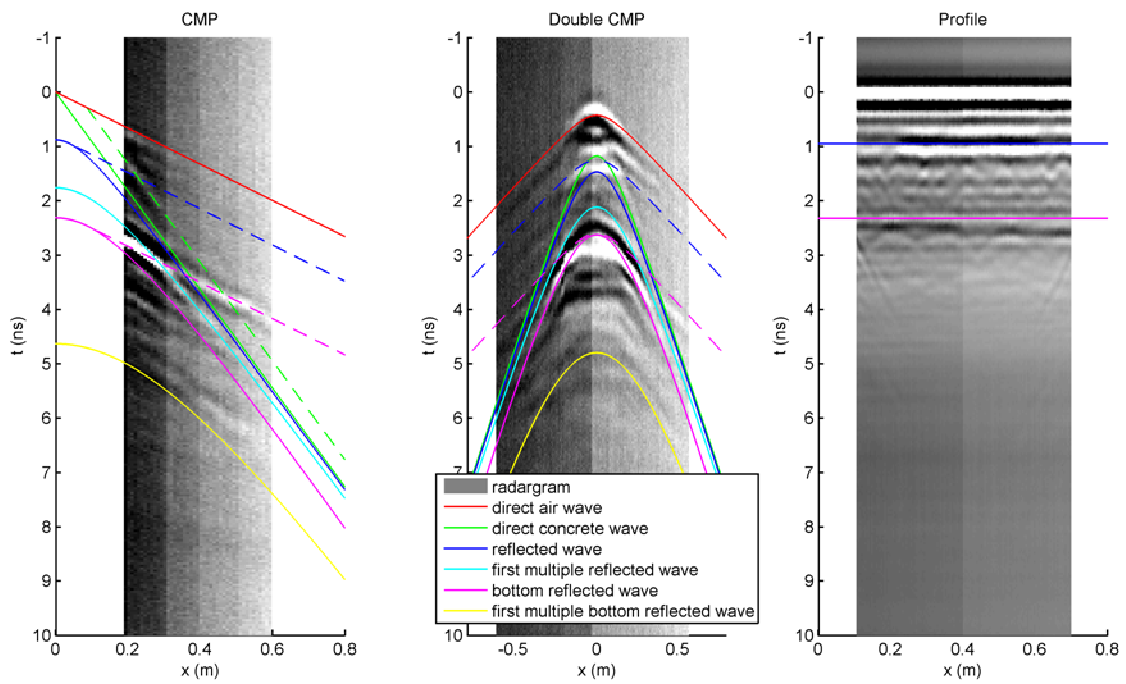
Slab 1.2.2: Defect 3 / 5 cm



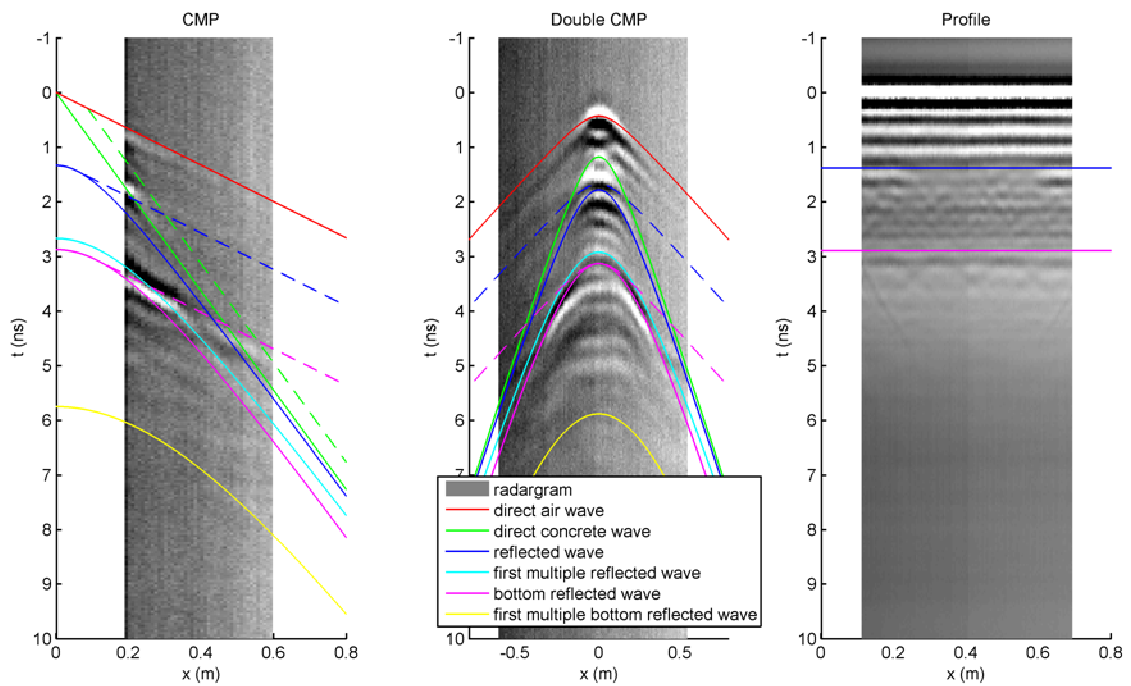
Slab 1.1.2: Defect 3 / 8 cm



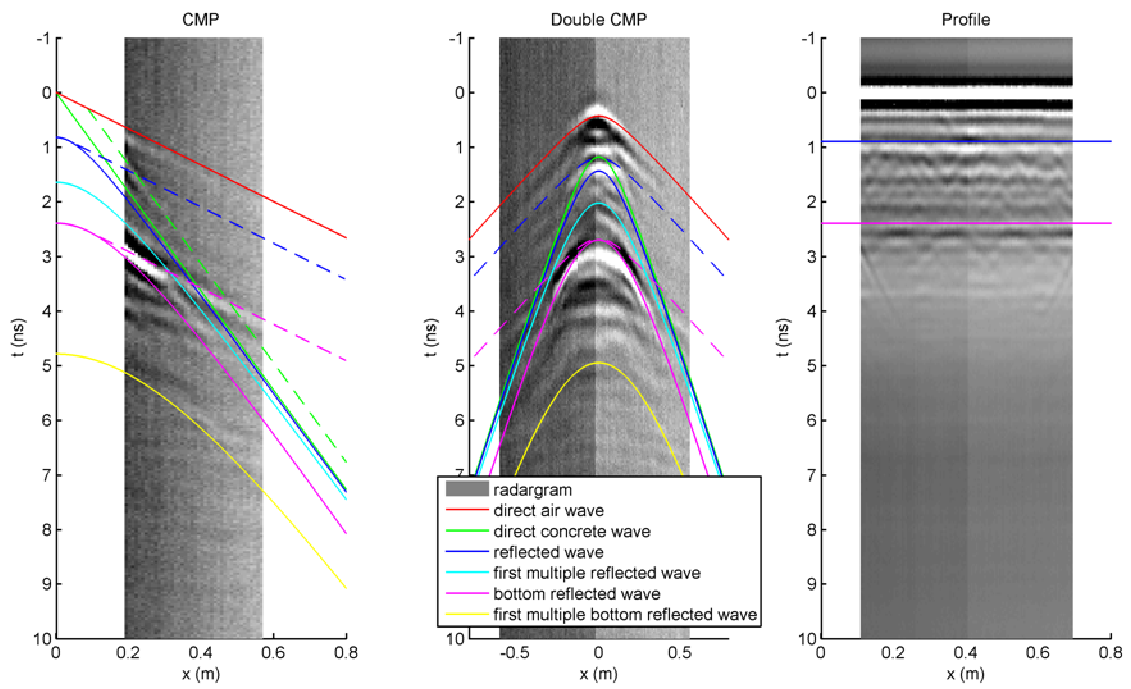
Slab 1.3.3: Defect 4 / 5 cm



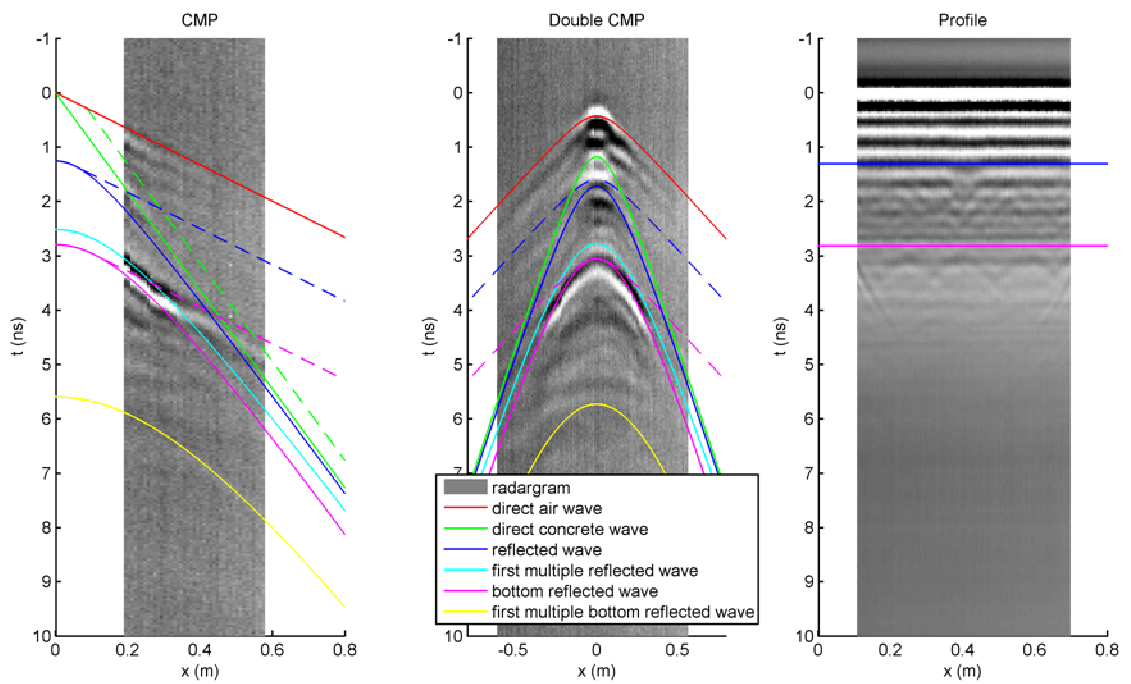
Slab 1.3.2: Defect 4 / 8 cm



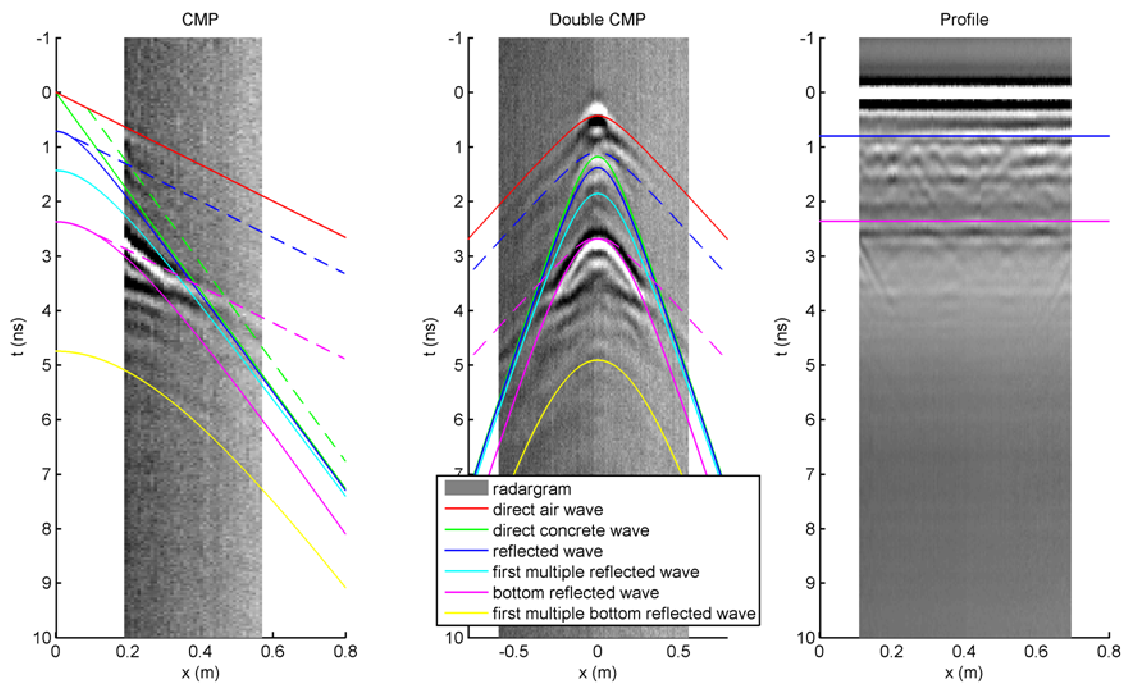
Slab 1.3.4: Defect 5 / 5 cm



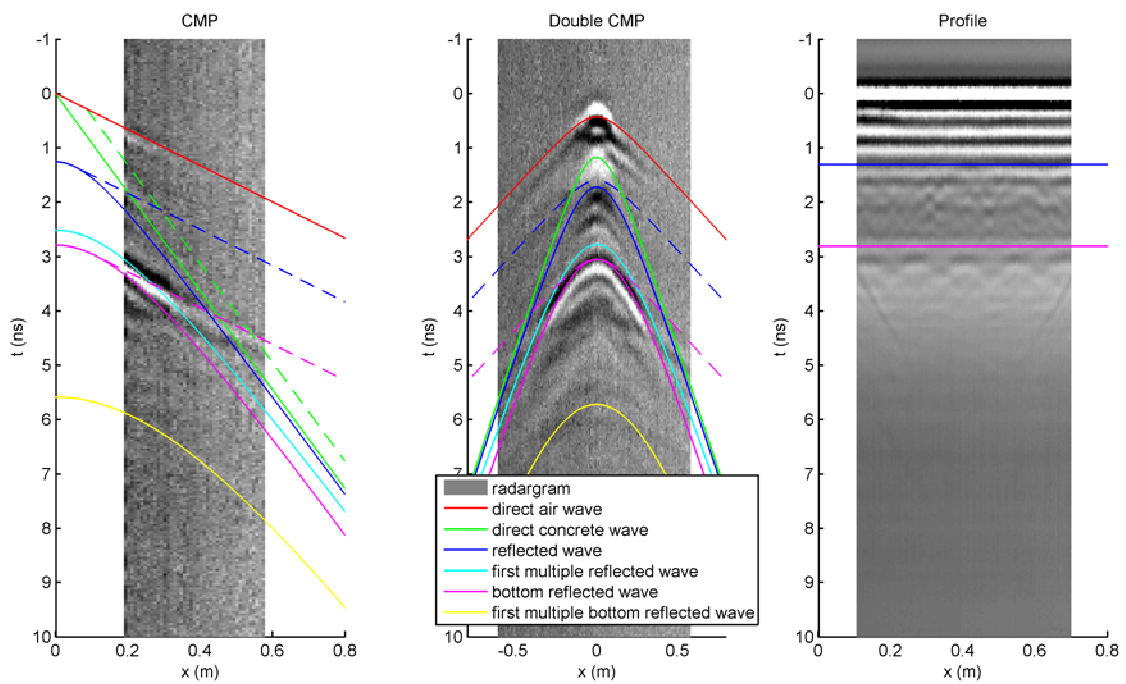
Slab 1.3.1: Defect 5 / 8 cm



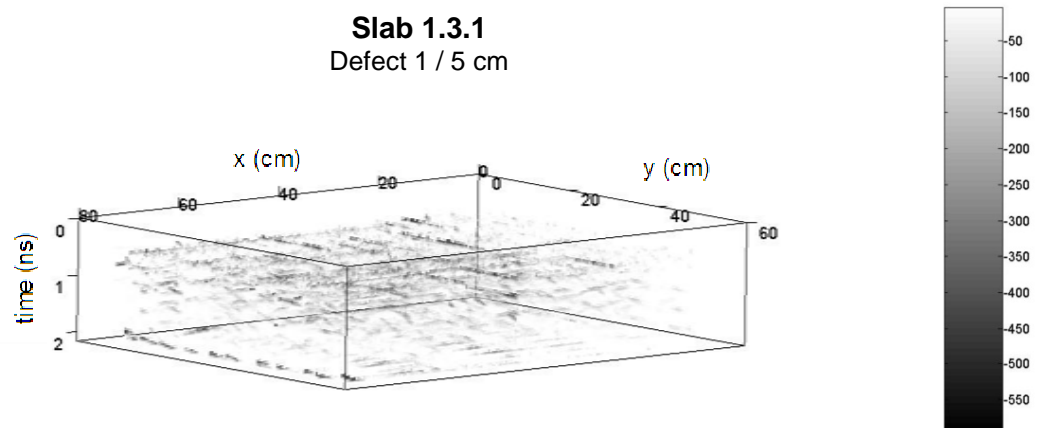
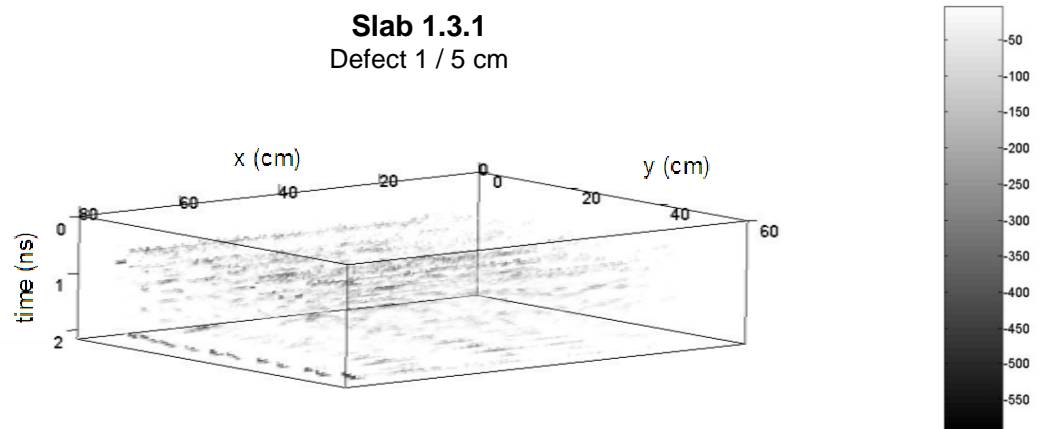
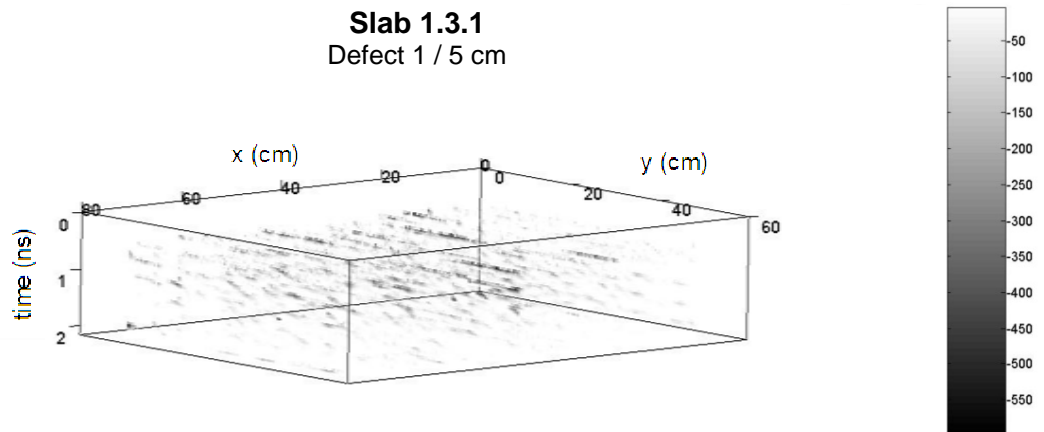
Slab 1.1.4: Defect 6 / 5 cm



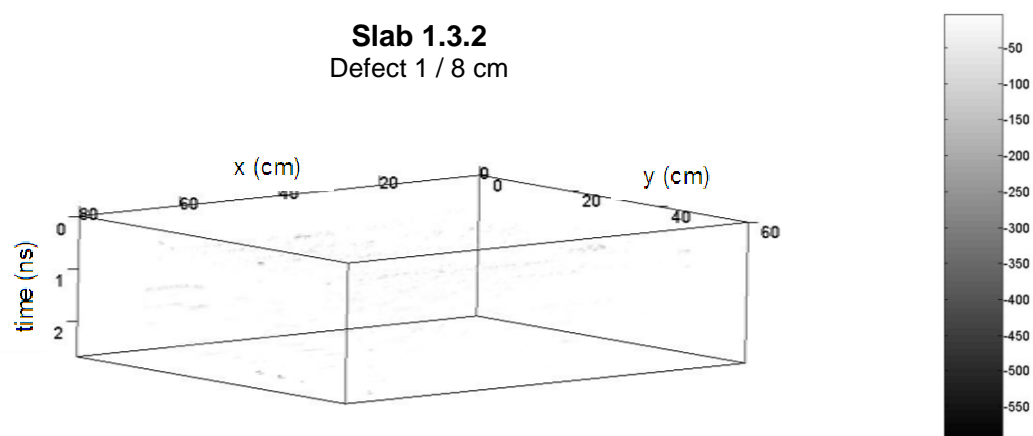
Slab 1.2.4: Defect 6 / 8 cm



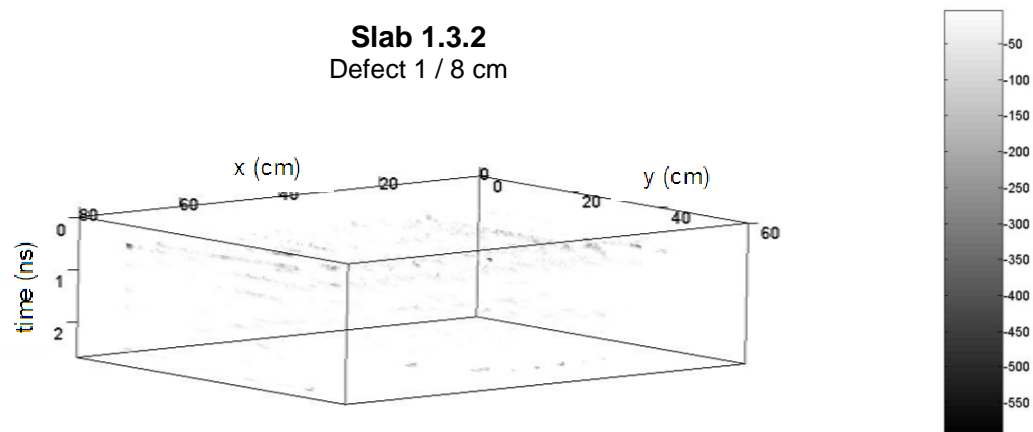
Appendix 7 : 3D visualization of the defects



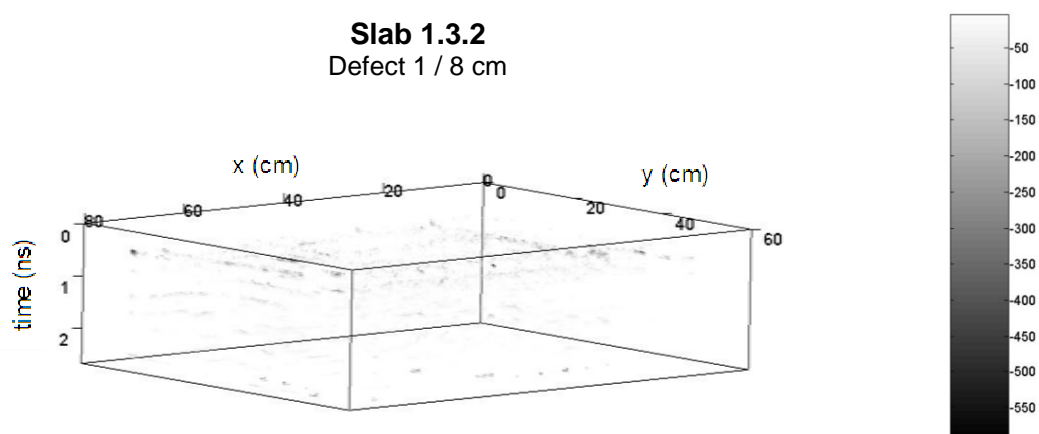
Slab 1.3.2
Defect 1 / 8 cm



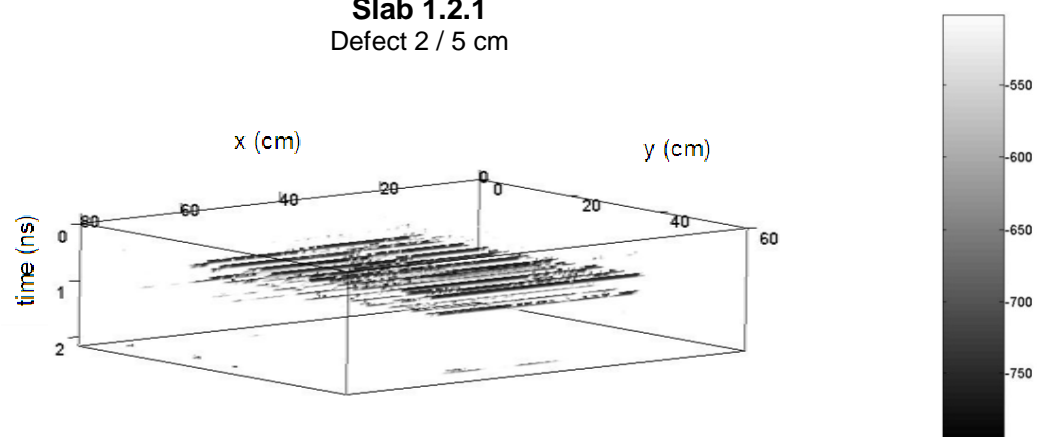
Slab 1.3.2
Defect 1 / 8 cm



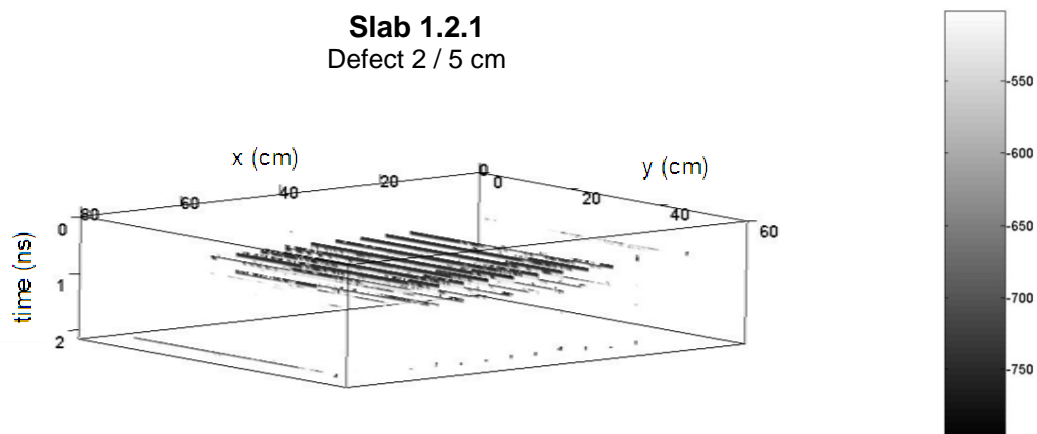
Slab 1.3.2
Defect 1 / 8 cm



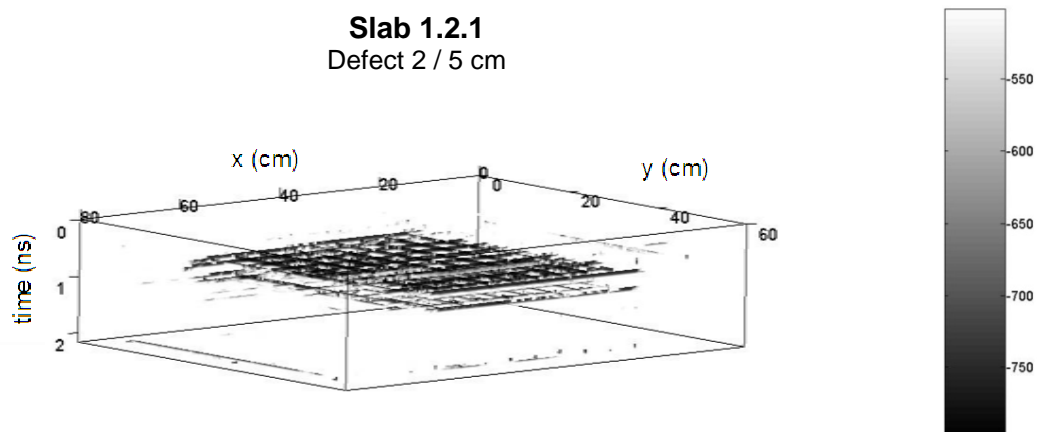
Slab 1.2.1
Defect 2 / 5 cm

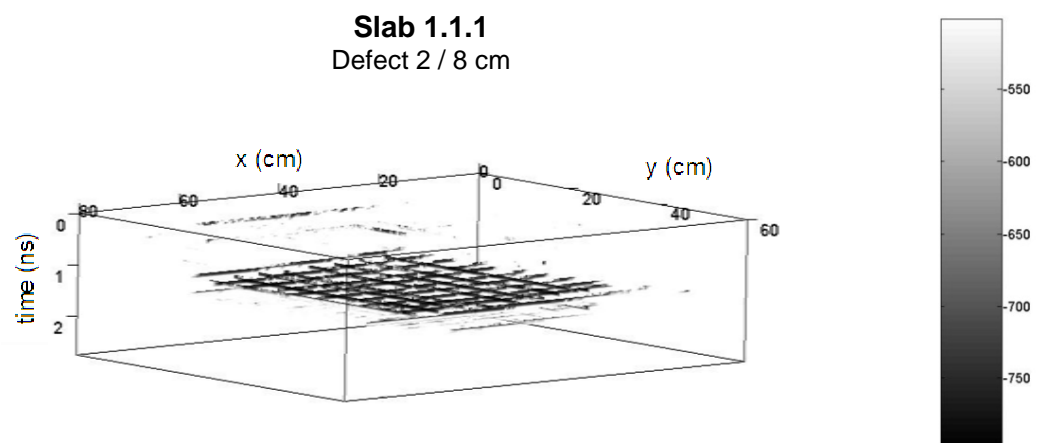
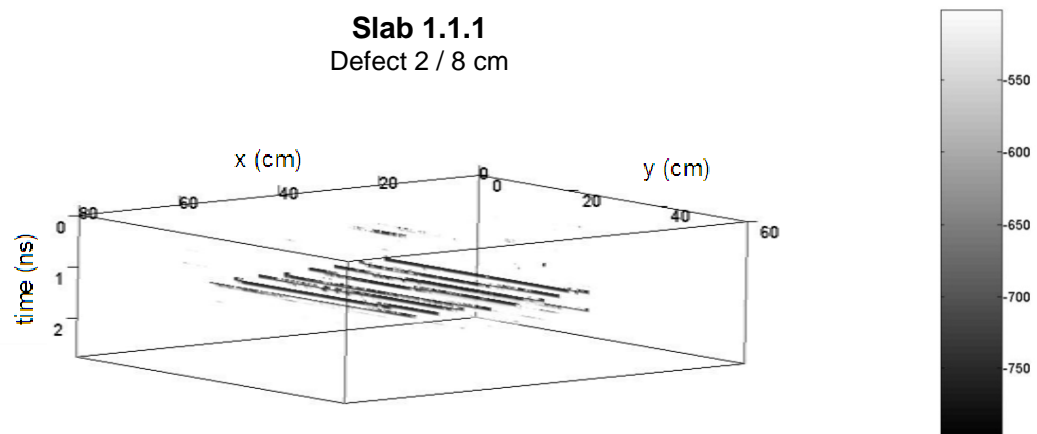
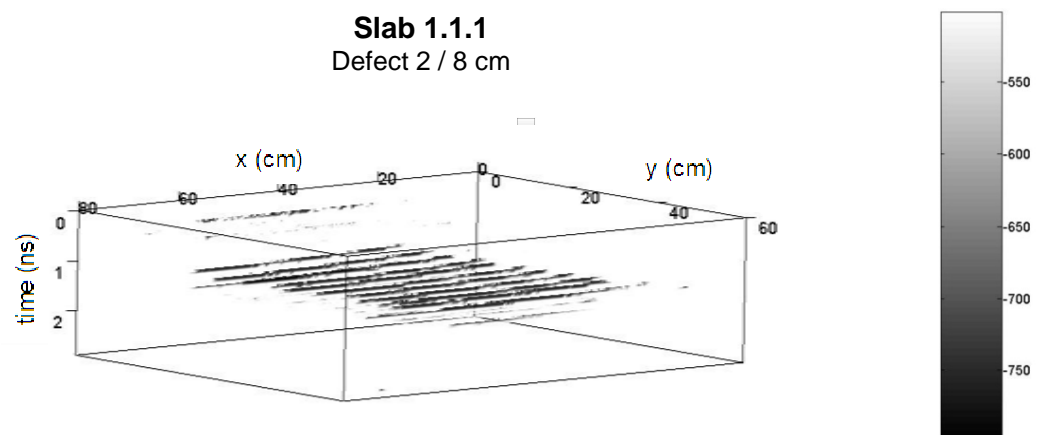


Slab 1.2.1
Defect 2 / 5 cm

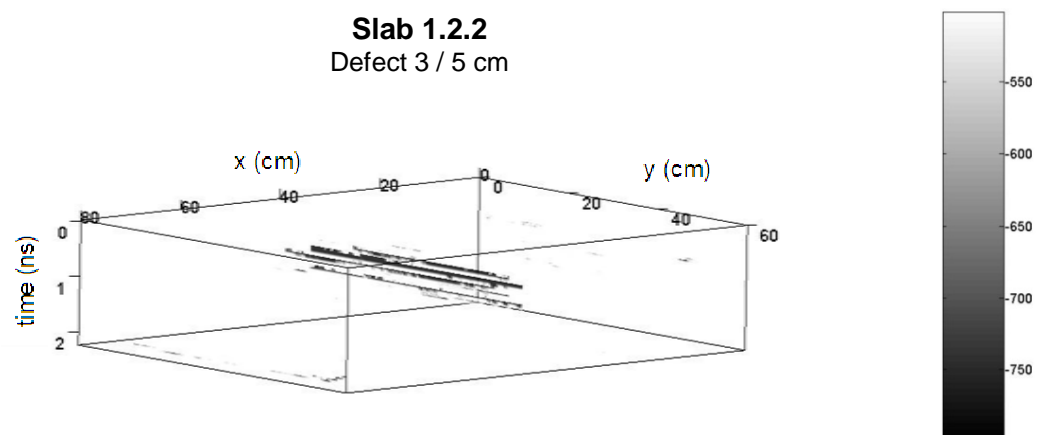


Slab 1.2.1
Defect 2 / 5 cm

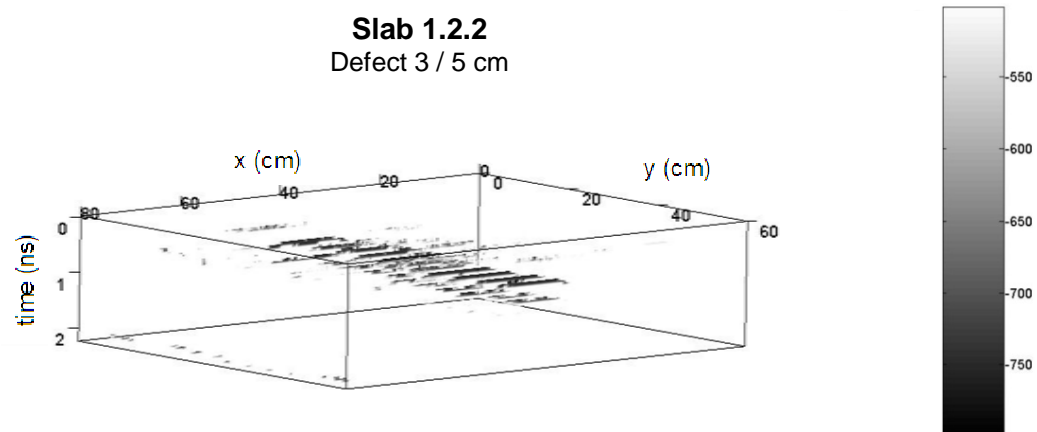




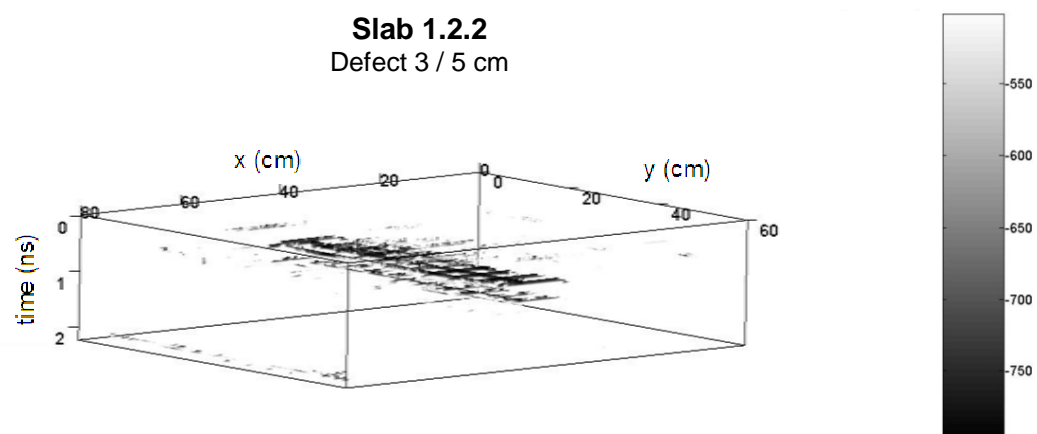
Slab 1.2.2
Defect 3 / 5 cm



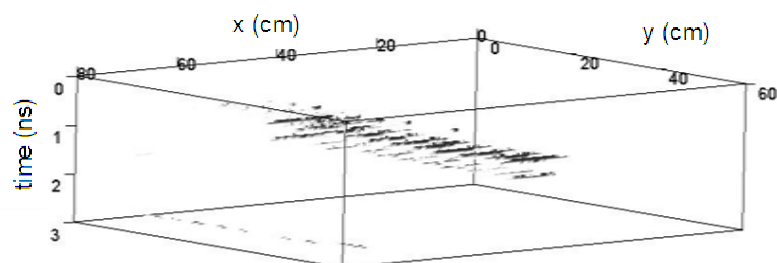
Slab 1.2.2
Defect 3 / 5 cm



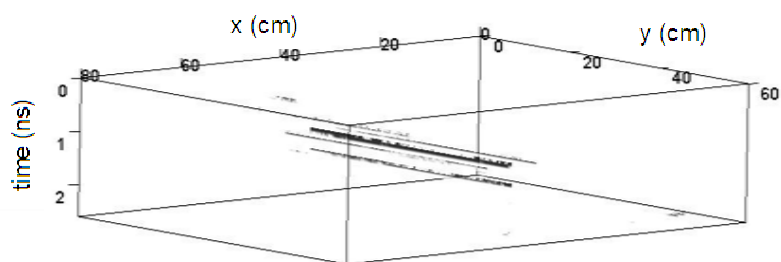
Slab 1.2.2
Defect 3 / 5 cm



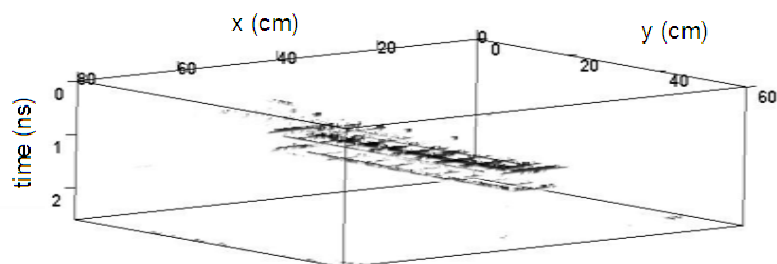
Slab 1.1.2
Defect 3 / 8 cm



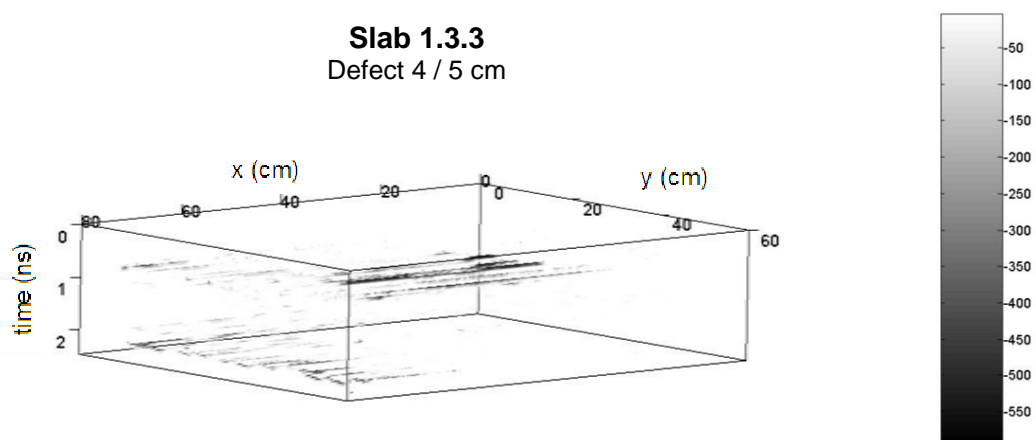
Slab 1.1.2
Defect 3 / 8 cm



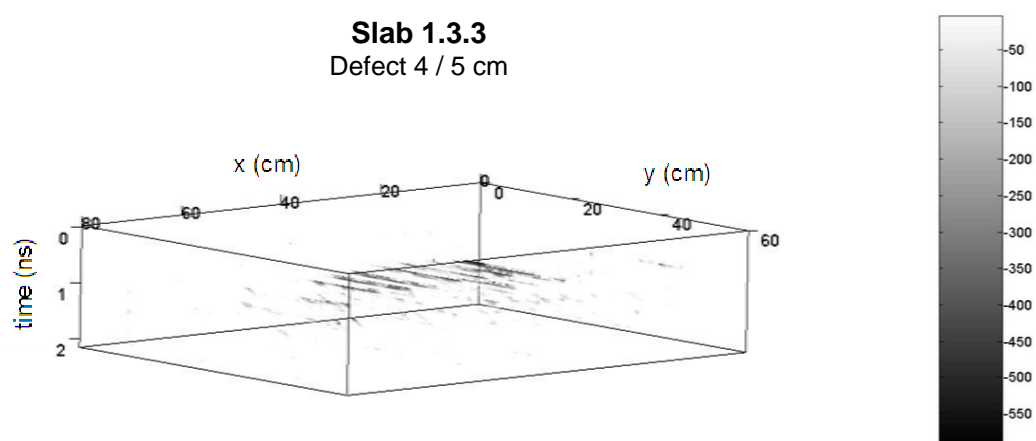
Slab 1.1.2
Defect 3 / 8 cm



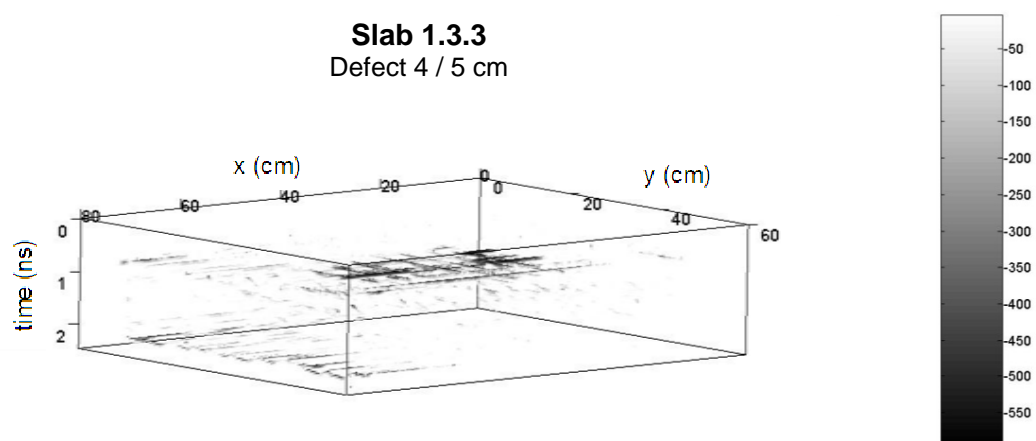
Slab 1.3.3
Defect 4 / 5 cm



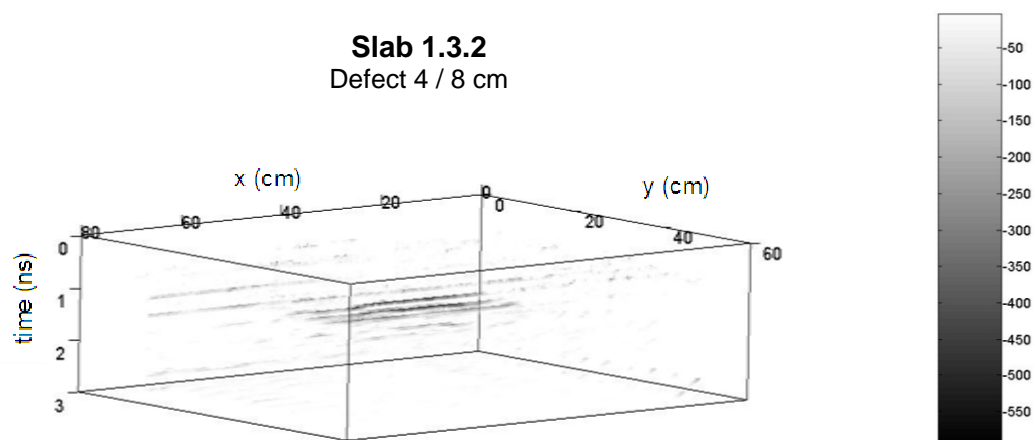
Slab 1.3.3
Defect 4 / 5 cm



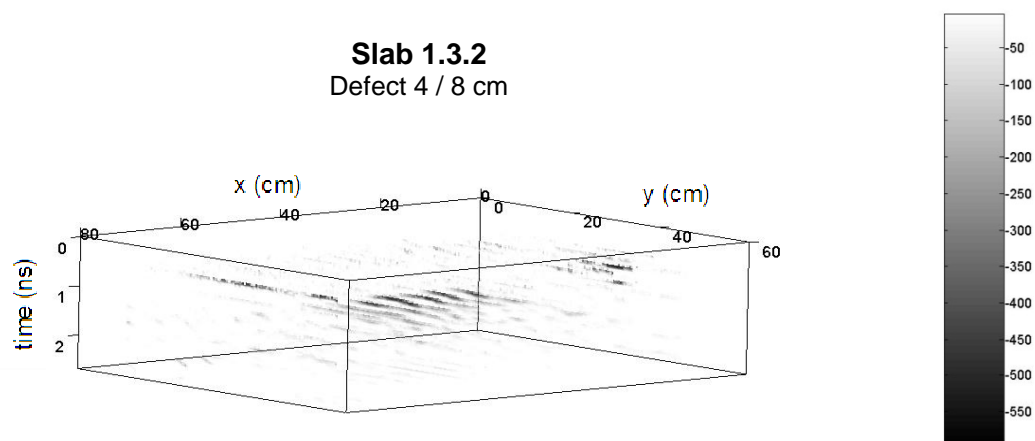
Slab 1.3.3
Defect 4 / 5 cm



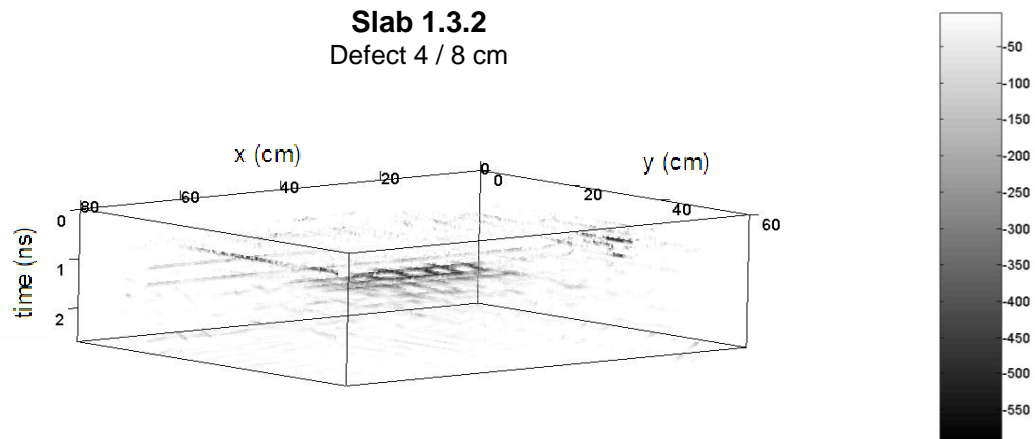
Slab 1.3.2
Defect 4 / 8 cm



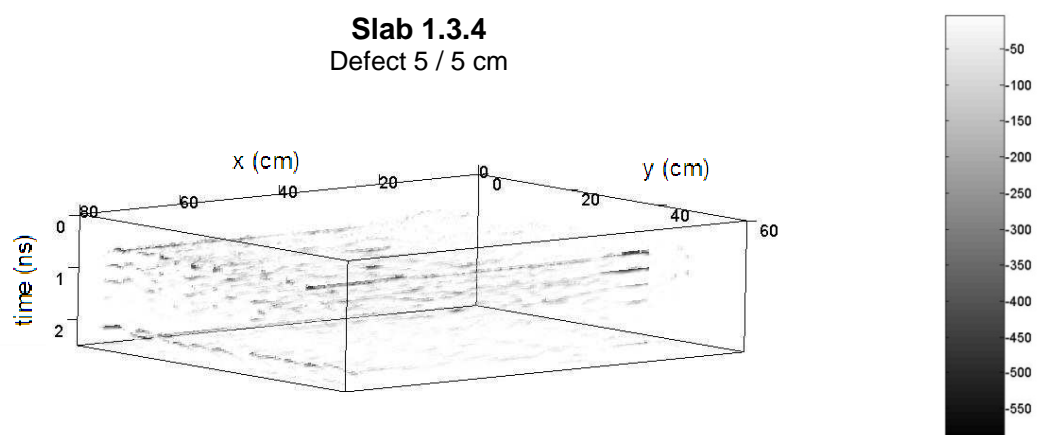
Slab 1.3.2
Defect 4 / 8 cm



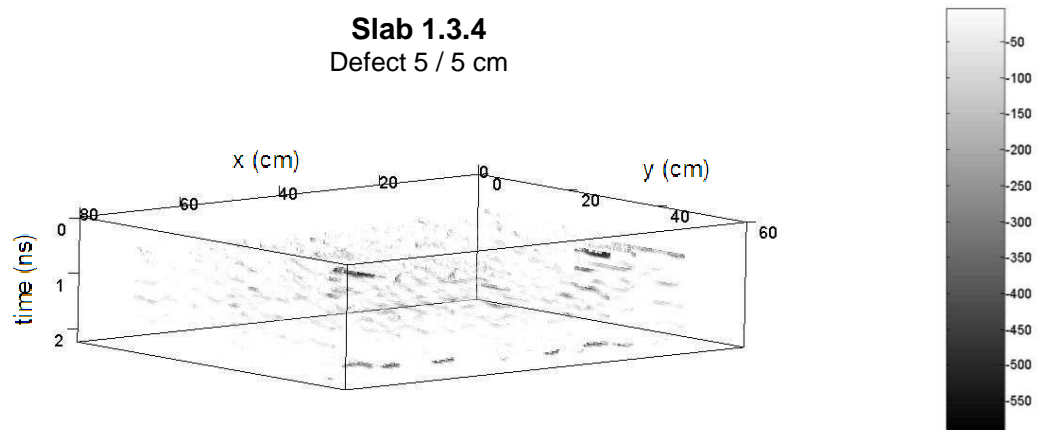
Slab 1.3.2
Defect 4 / 8 cm



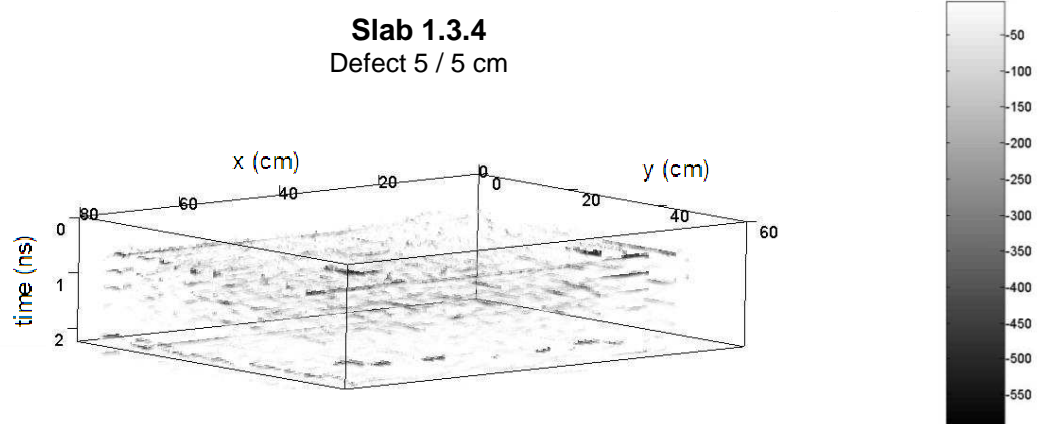
Slab 1.3.4
Defect 5 / 5 cm



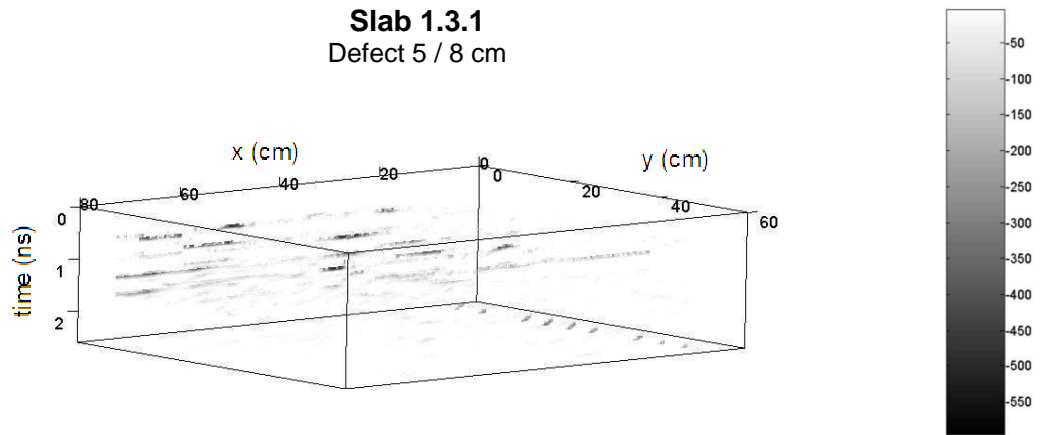
Slab 1.3.4
Defect 5 / 5 cm



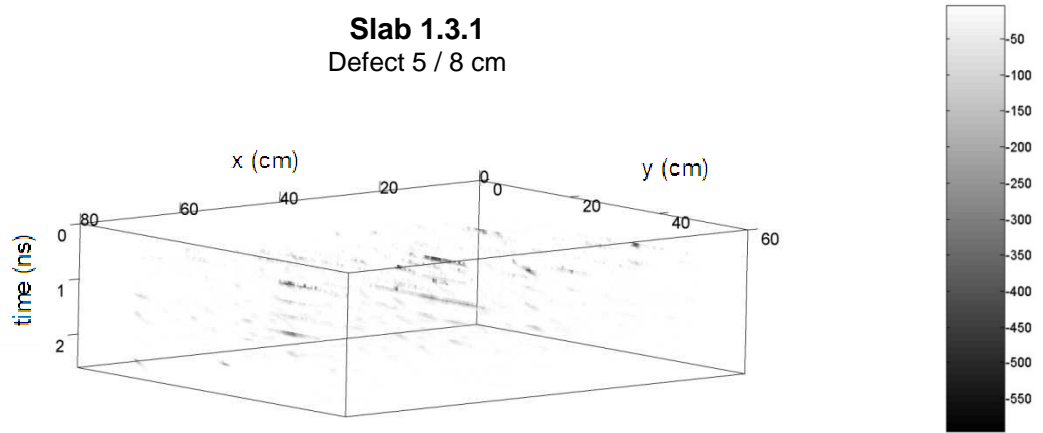
Slab 1.3.4
Defect 5 / 5 cm



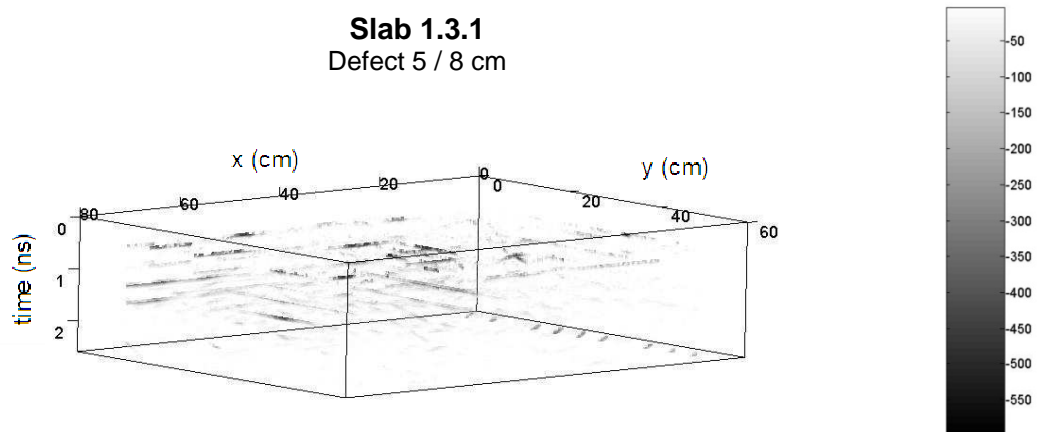
Slab 1.3.1
Defect 5 / 8 cm



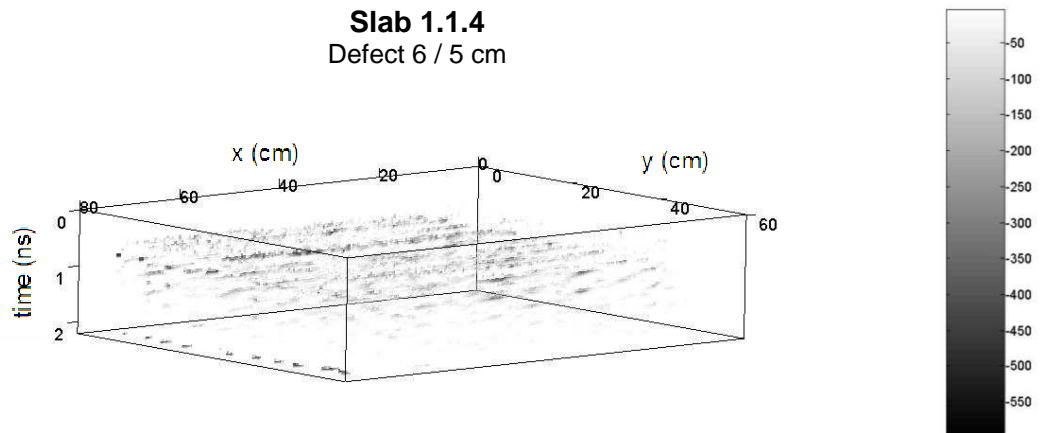
Slab 1.3.1
Defect 5 / 8 cm



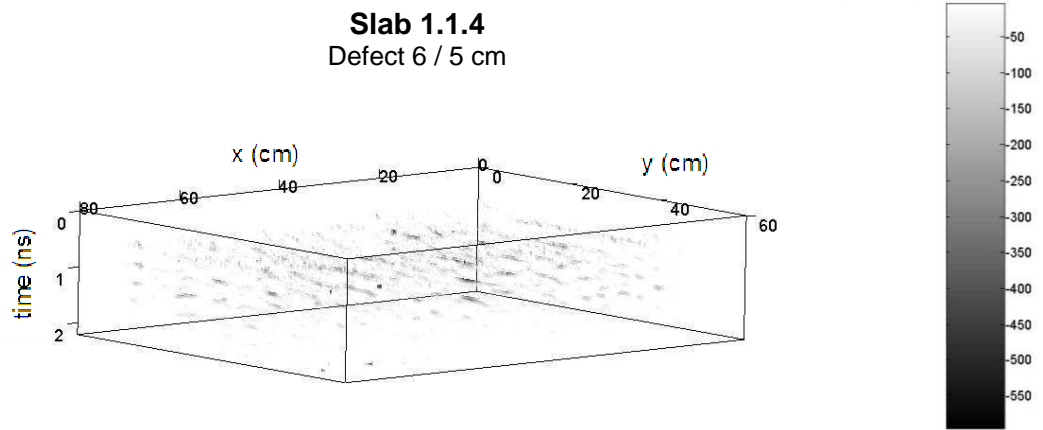
Slab 1.3.1
Defect 5 / 8 cm



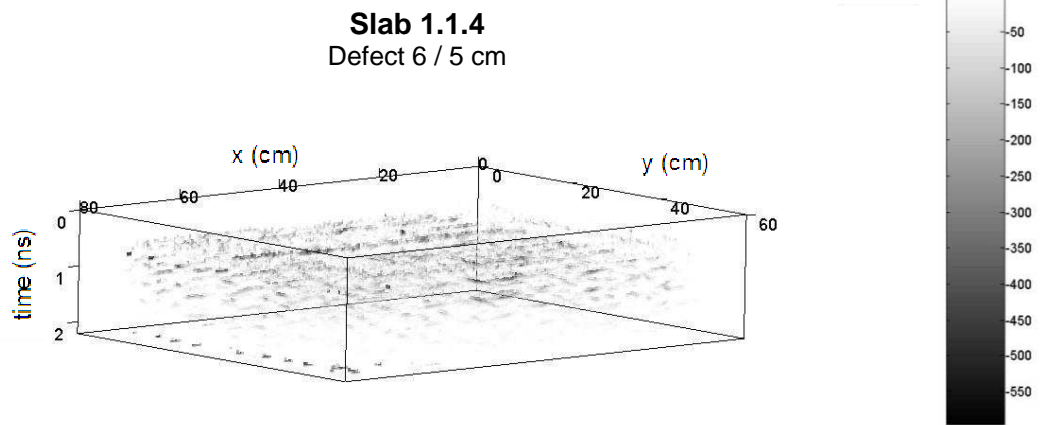
Slab 1.1.4
Defect 6 / 5 cm



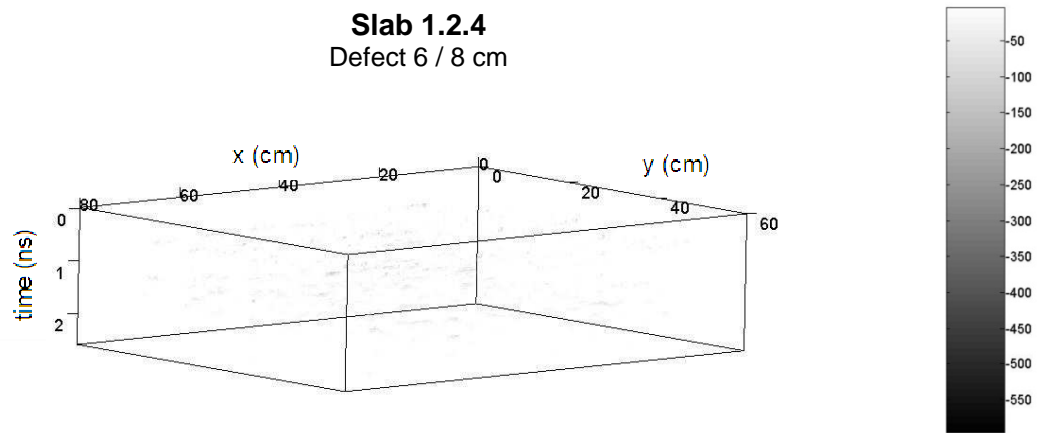
Slab 1.1.4
Defect 6 / 5 cm



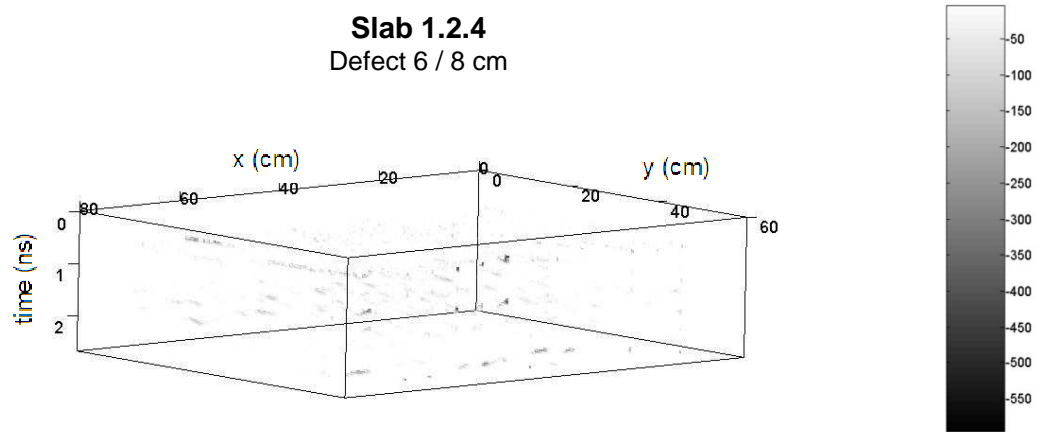
Slab 1.1.4
Defect 6 / 5 cm



Slab 1.2.4
Defect 6 / 8 cm



Slab 1.2.4
Defect 6 / 8 cm



Slab 1.2.4
Defect 6 / 8 cm

